REPORT DOCUMENTATION PAGE		READ INSTRUCTIONS BEFORE COMPLETING FORM
1. REPORT NUMBER	2. GOVT ACCESSION NO. AD-A107523	3. RECIPIENT'S CATALOG NUMBER
4. TITLE (and Subtitle) "Atmospheric Fluctuations Which Lead To Trackable Radar Signals In The Marine Boundary Layer"		5. TYPE OF REPORT & PERIOD COVERED Final 1 Aug 1980 - 31 Jul 1981
		6. PERFORMING ORG. REPORT NUMBER ARAP -450
7. AUTHOR(s) W.S. Lewellen, H. Segur, R.I. Sykes and C.P. Cerasoli		8. CONTRACT OR GRANT NUMBER(s) N00014-80-C-0873
9. PERFORMING ORGANIZATION NAME AND ADDRESS Aeronautical Research Associates of Princeton, Inc. P.O. Box 2229, 50 Washington Rd., Princeton, NJ 08540		10. PROGRAM ELEMENT, PROJECT, TASK AREA & WORK UNIT NUMBERS
11. CONTROLLING OFFICE NAME AND ADDRESS Office of Naval Research 800 Quincy Street Arlington, VA 22217		12. REPORT DATE Jul 1981
		13. NUMBER OF PAGES 130
14. MONITORING AGENCY NAME & ADDRESS(if different from Controlling Office)		15. SECURITY CLASS. (of this report) Unclassified
		15a. DECLASSIFICATION DOWNGRADING SCHEDULE

16. DISTRIBUTION STATEMENT (of this Report)

Unclassified, Distribution Unlimited

17. DISTRIBUTION STATEMENT (of the abstract entered in Block 20, if different from Report)

18. SUPPLEMENTARY NOTES

19. KEY WORDS (Continue on reverse side if necessary and identify by block number)

clear air radar targets   Kelvin-Helmholtz Waves
refractive index fluctuations
internal wave breaking
atmospheric boundary layer

20. ABSTRACT (Continue on reverse side if necessary and identify by block number)

    A description and rough cataloguing of the dominant types of fluid dynamic features which may be expected to yield trackable radar targets in the atmospheric boundary layer is provided. Conditions favorable for target motion relative to the ambient wind velocity are discussed. One particularly interesting type of wave generated target is that involving Kelvin-Helmholtz wave breaking which occurs when a wave of sufficient amplitude passes through a slightly stable fluid shear layer. This type of wave breaking is examined

numerically using A.R.A.P.'s second-order closure turbulence model. This normalized computation allows the evolution of the radar pattern for this particular type of event to be interpreted in terms of the temperature, humidity, and velocity across a particular shear zone, and the wave speed of the triggering internal wave.

TABLE OF CONTENTS

LIST OF FIGURES

LIST OF TABLES

I. Introduction

Modern, high-powered radars can receive signals from targets that are nothing more than humidity and/or temperature fluctuations in clear air. The fluctuations in refractivity induced by the fluctuations in humidity or temperature scatter the radar signal sufficiently that the back scatter can be observed by a sensitive receiver. Such clear air radar targets have been observed for some time (c.f., Ottersten, Little, and Hardy, 1973). They represent both an opportunity for probing atmospheric motions and possible interference with sensitive radar operations. An operational, sensitive receiver must be able to discriminate between these atmospheric targets and other targets of potential interest. In some cases, unusually clear signals have been associated with specific physical mechanisms, such as convective plumes (Konrad, 1970) and shear-induced wave breaking (Richter, 1979). More frequently the precise nature of the fluctuations is insufficiently known to predict the motion or evolution of the target. This report presents the results of the initial phase of a theoretical investigation of different possible fluid dynamical mechanisms which can lead to relatively strong radar signals. The goal of this study is to provide a better understanding of the phenomena and an improved capability to predict the motion and evolution of these targets.

This report is divided into five chapters. Chapter II provides a brief description of the relationships between turbulent fluctuations in humidity and temperature and the potential strength of radar signals. This permits a delineation of what types of atmospheric motions are detectable by radar. Chapter III provides a description and rough cataloguing of a number of different physical phenomena which may produce these atmospheric motions. Chapter IV presents an analysis of part of the data obtained by NRL during recent investigations which coordinated radar probing with _in situ_ aircraft

measurements. Appendix A provides a detailed examination of one particular type phenomena, Kelvin-Helmholtz wave breaking, using A.R.A.P.'s second-order closure turbulence model. This normalized computation allows the evolution of the radar pattern for this particular type of event to be interpreted in terms of atmospheric variables such as the increments in temperature, humidity, and velocity across a particular shear zone, and the wave speed of a triggering internal wave.

The concluding remarks provide specific recommendations for further work which is needed to extend our knowledge of the relationships between particular features of the radar return and the nature of the atmospheric motion which generated it.

II. The Dependence of Radar Reflectivity
on Humidity Fluctuations

Radar echoes may be generated by the backscatter caused by fluctuations in the refractive index. The refractive index for cm wavelength radio waves is related to temperature and humidity by the equation (Battan, 1970)

$$n = 1 + 10^{-6} \left(\frac{77.6}{T} p + 4810 \frac{e}{T} \right) \qquad (2.1)$$

with T equal to temperature in °K, p equal to pressure in mb and e equal to water vapor partial pressure in mb. Echoes generated by backscatter are distributed rather than point targets. The radar equation for distributed targets as given by Richter (1980) may be written as

$$P_R = 0.0177 \, P_T \, A_e \, h \, n \, R^{-2} \qquad (2.2)$$

where P_R is the average received power; P_T, transmitted power; A_e, effective antenna area; h, range resolution; n, backscatter cross section per unit volume (reflectivity); and R is the range of the echo region.

The radar reflectivity is related directly to the spatial correlation of the fluctuations in refractive index,

$$n = 0.38 \, \lambda^{-1/3} \, C_n^2 \quad , \qquad (2.3)$$

where λ is the radar wavelength, C_n^2 is the refractive index structure function

which measures the spatial correlation of the fluctuations in refractivity,

$$C_n^2 = \frac{\overline{[n(x) - n(x+r)]^2}}{r^{2/3}} , \qquad (2.4)$$

and r is the separation distance for the two point correlation. Turbulent fluctuations on the centimeter scale length generally fall into a part of the inertial subrange of the turbulent kinetic energy spectrum. In this range C_n^2 is independent of separation distance. It is determined by the total variance in refractivity and the dissipation length scale, ℓ_d.

$$C_n^2 \propto \overline{n'n'} \, \ell_d^{-2/3} \qquad (2.5)$$

When fluctuations in pressure are neglected in comparison to fluctuations in temperature and water vapor mixing ratio, the following expression for C_n^2 may be derived (Lewellen and Teske, 1975)

$$
\begin{aligned}
C_{n(radar)}^2 = \ & 7.3 \times 10^{-3} \, \Lambda^{-2/3} \, \frac{p^2}{T^4} \left\{ \left(1 + \frac{2B\overline{H}}{T}\right) \overline{\theta_V' \theta_V'} \right. \\
& - 2 \left(1 + \frac{2B\overline{H}}{T}\right)(0.61T_\infty + B) \, \overline{\theta_V' H'} \\
& \left. + B^2 + \left(1 + \frac{2B\overline{H}}{T}\right)\left[(0.61T_\infty)^2 + 2(0.61T_\infty)B\right] \, \overline{H'H'} \right\} \qquad (2.6)
\end{aligned}
$$

where B = 7,730, p is in atmospheres, T is temperature in °K, H is water vapor mixing ratio fluctuation, θ_V' is the virtual potential temperature fluctuation, and Λ is the turbulent macroscale length used in A.R.A.P., Inc.'s turbulent

12

transport model.

In the marine atmospheric boundary the leading term in C_n^2 will be

$$C_n^2 \approx 6 \times 10^{-5} \Lambda^{-2/3} \overline{H'H'} \tag{2.7}$$

Thus, qualitatively, C_n^2 can be expected to be proportional to the square of the total incremental change in water vapor mixing ratio induced by the particular fluid motion and inversely proportional to the two-thirds power of the thickness of the turbulent zone across which this change occurs ($\Lambda \sim 0.2 \times$ thickness of the turbulent zone).

Detectable values of C_n^2 depend on radar characteristics and range as given in Eqs. (2.2 and 2.3) but values as low as 10^{-15} may be significant. This may be induced by humidity increments of the order of a fraction of a gm per kg across a turbulent layer of the order of a few meters thick.

The task of understanding clear air radar returns involves understanding particular fluid dynamic features which may be associated with relatively strong changes in water vapor content across relatively thin layers of turbulence. A catalogue of such features is discussed in Section III. For those features which may be approximated as two-dimensional in some sense, the turbulent transport code developed at A.R.A.P., Inc., can be used to quantitatively follow the evolution of the fluid dynamic regions of significant C_n^2.

13

III. A Catalogue of Physical Phenomena Leading to the
Necessary Humidity Fluctuations Required for Radar Returns

Fluid motions associated with a number of physical phenomena can produce clear air radar returns, and one can catalogue these phenomena using various criteria. We initially choose two broad categories for cataloguing, depending on whether the motion is associated with convective cells or with internal gravity wave phenomena.

3.1 Convective Motions

Convective motion can occur in situations where unstable density gradients exist. This can occur either over large horizontal extents, such as in the atmospheric boundary layer over land on a sunny day, or in localized regions of unstable gradients that may exist within a stable background. An example of this latter situation is a heated plume (e.g., from a power plant) in the evening or early morning atmospheric boundary layer, which is statically stable. Theoretical study of such motions dates back to the work of Morton, Taylor, and Turner (1956), who studied the motion of buoyant parcels using mixing length theory to model the turbulent entrainment of ambient fluid into the parcel. Although their model is very simple, the basic concepts used by Morton, et al., are correct and we now outline their results.

A buoyant parcel generated in an unstratified environment rises due to gravitational forces. Ambient fluid is entrained into the parcel, causing a dilution of the density difference between parcel and environment, $[\rho_p(z) - \rho_{amb}(z)]$, where ρ_p is the parcel density and ρ_{amb} is the ambient density. The dilution of the density difference decreases the acceleration of the parcel. Morton, et al., showed that in an unstratified environment, the vertical velocity, w, parcel size, r, and density difference behave as

15

$$w \sim t^{-1/2}$$

$$r \sim t^{1/2}$$

$$(\rho_p - \rho_{amb}) \sim t^{-3/2} \; ,$$

where t is a measure of elapsed time from the onset of the parcel motion. The parcel continues upward indefinitely, although at some point it will effectively merge with the environment.

In the case of a stably stratified environment, the parcel motion is affected by the ambient density gradients. A case of interest in this report is a "two-layer" fluid which is modeled by density ρ_u overlaying density ρ_ℓ, where the ambient condition is stable, $\rho_\ell > \rho_u$, and we define a density jump, $\Delta\rho = \rho_\ell - \rho_u$. A parcel released in the lower region rises in a manner similar to that described previously until it approaches the height of the density jump. For the case, $|\rho_u - \rho_\ell|/\Delta\rho \gg 1$, the parcel is relatively unaffected by the density jump and continues upward. The more relevant situation to the atmospheric boundary layer is $|\rho_u - \rho_\ell|/\Delta\rho < 1$. In this case, the density jump provides a strong deceleration of the parcel. Typically, the parcel slightly overshoots the density jump height and then falls back and eventually collapses. The above situations were studied in the laboratory by Scorer (1957) and the theory of Morton, et al., agrees reasonably well with observations. It is more difficult to apply the simple theories to the atmospheric case, where the ambient turbulence levels can modify the parcel motion. In particular, the entrainment process can be greatly enhanced when the environment is turbulent, so that the parcel decelerates much more rapidly. Recent laboratory observations attempting to simulate unstable atmospheric conditions can be found in Deardorff, et al. (1980).

16

Thermals in the atmosphere have been extensively studied using techniques such as glider planes (Woodward, 1956), instrumented aircraft (Lenschow and Stephens, 1980) and radar observations (Hardy and Ottersten, 1969; Konrad, 1970). The following picture is obtained from these studies. An individual thermal (referred to as a "Type I" cell by Hardy and Ottersten) ranges in horizontal dimensions from about 50 to 100 meters at onset to about 1000 to 2000 meters near the top of the mixed layer, Z_I. The parcels are warmer than the environment up to a level near Z_I, after which they are cooler than the surroundings and are negatively buoyant. The parcels continue past their neutrally buoyant level due to their upward momentum. They are likely to possess a humidity excess throughout their ascent. Turbulent mixing and the resulting refractivity fluctuations, C_n^2, are most pronounced at the outer edges, or "skin", of the parcel. This results in clear air radar returns which appear as doughnut-shaped echoes on a "plan position indicator" (PPI) scan (see Figure 3.1). These patterns become larger as the height of the scanning plane is increased. The intensity of the radar returns depends on the magnitude of C_n^2, which is proportional to the temperature and humidity differences between the thermal and the surroundings, as discussed in Chapter II. A "range height indicator" (RHI) scan typically shows thermals as perturbations at the top of the mixed layer. The mean humidity and temperature gradients at the top of the mixed layer give rise to corresponding fluctuations at this level. These fluctuations generally provide a radar return which appears as a continuous band centered near Z_I on a RHI scan (Figure 3.2). Examples of the radar returns from individual thermals can be found in Konrad (1970), who used X-band, S-band and UHF band radars for his studies. These radars had respective frequencies of 9.3 Ghz, 2.8 Ghz and 430 Mhz, and Konrad comments that the returns were best for the S-band radar. The thermals behave as independent entities, and as such, drift with the local mean wind as long as there is no strong vertical shear in the wind. Their lifetimes are of order 20 to 40 minutes, which is the time between onset near the statically unstable surface and the time when the thermal reaches the top of the mixed layer. For a more detailed discussion of clear air convective cells in the unstable boundary layer, see Richter, Jensen and Noonkester (1974).

17
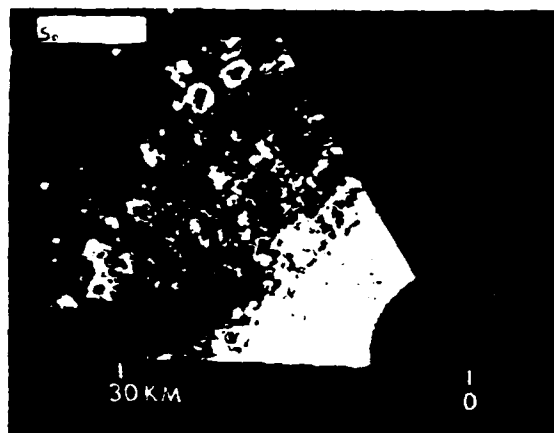
Figure 3.1 - PPI photograph taken with 10.7 cm radar at 3° elevation angle. Individual thermals are clearly seen as "doughnut" shaped entities (from Hardy and Ottersten, 1969).
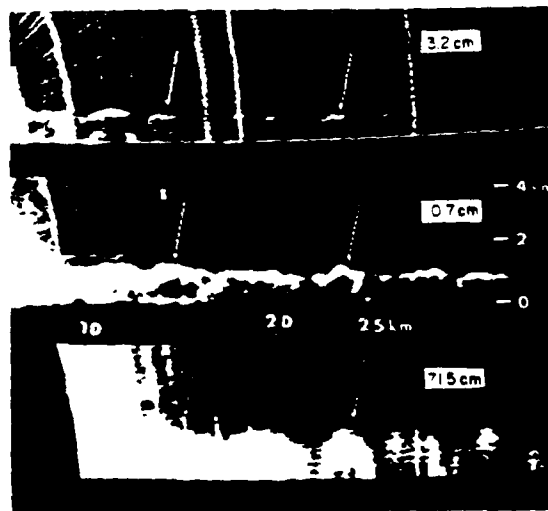
Figure 3.2 - RHI photographs at radar wavelengths of 3.2, 10.7, and 71.5 cm, taken while the sky was clear. Individual thermals appear as perturbations near the top of the mixed layer at approximately 1 km (from Hardy and Ottersten, 1969).

18

Individual cells frequently become organized on a larger scale in the atmospheric boundary layer. There are two ways in which this collective motion can happen. The first takes the form of Bénard cell motion when observed in PPI scans (Hardy and Ottersten refer to such motions as "Type II" cells). These cells are typically 5 to 10 km wide (as shown in Figure 3.3). and the overall structure can last several hours. The outer boundary of the Bénard-like cells is composed of thermals with individual lifetimes of order 30 minutes, and a mean updraft exists in this region. The central area of the Bénard cells is characterized by a mean downflow and no clear air radar returns.

The second type of collective motion is commonly known as "thermal streets". In this case, individual cells align parallel to the mean wind and appear as bands on PPI scans. Thermal streets tend to appear when the mean velocity, $U(z)$, is of sufficient magnitude and the wind direction is sufficiently constant to allow the individual convective cells to become aligned. The spacing between the bands ranges from approximately 1 to 4 times the mixed layer height, and the bands can extend up to 500 km in length. An observational example of thermal streets is shown in Figure 3.4a, and results from a two-dimensional computation are presented in Figure 3.4b. It should be noted that the source of the clear air radar returns for the thermals need not be humidity and temperature fluctuations. Hardy and Ottersten discuss the likelihood of insects acting as scatterers. In such cases, the insects are caught in the updrafts and are responsible for radar returns.

3.2 Wave Phenomena in the Atmosphere: Unstable and Stable Disturbances

We now discuss wave phenomena which can give rise to clear air radar returns. A distinction will be made between (1) waves which are locally generated and travel with the local wind speed, and (2) waves which travel at velocities different from the local wind velocities, and propagate into the region of interest from afar. Both types of waves can be understood using the linearized Euler equations, and a brief theoretical discussion of these waves will be presented.

19
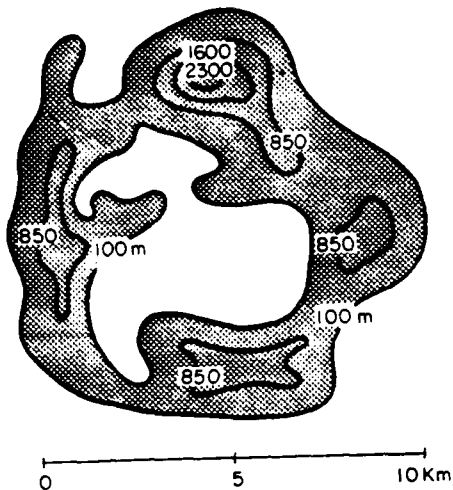
Figure 3.3 - Height contours of
reflectivity of a typical
Bénard-like cell. The shaded
region consists of individual
thermals and upward flow, while
the central region is charac-
terized by a slow downward
motion (from Hardy and Ottersten,
1969).
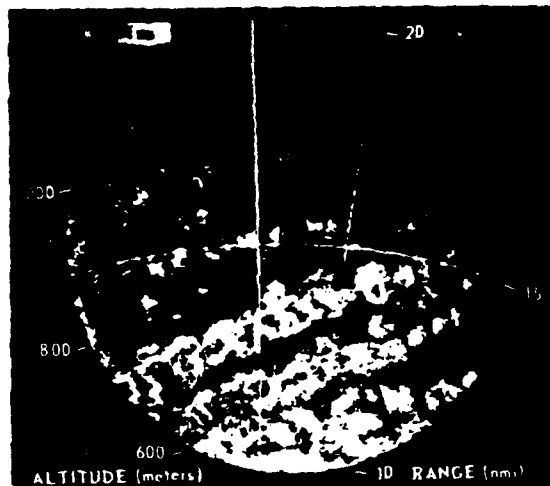
Figure 3.4(a) - An example of individual thermals aligned in "thermal streets". PPI photograph was taken using S-band radar at an elevation angle of 1.75° (from Konrad, 1970).
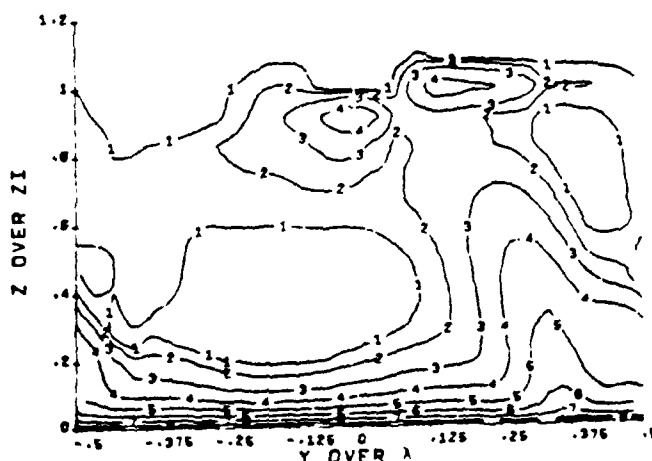
Figure 3.4(b) - Contours of radar reflectivity, C_n^2, for a two-dimensional computation by Lewellen, Teske and Sheng (1980). The plot is analogous to a RHI radar scan and shows regions of high C_n^2 near the top of the mixed layer, Z_I. The contours are labelled such that there is a factor of two difference between each contour, and the regions of high C_n^2 would appear as bands on a PPI scan.

21

The simplest configuration for studying atmospheric waves is one in which the atmosphere has no regions of static instability, beginning at the sea surface and extending clear up to the tropopause. In this configuration all small atmospheric disturbances will be waves of some type. To simplify the presentation, let us assume temporarily that the atmosphere is dry and incompressible. Also, we will assume that the scale of the motion is small enough that we may neglect the sphericity and rotation of the earth. The motion of small amplitude disturbances in this configuration was analyzed in the important work by Miles (1961) and Howard (1961) on the stability of a sheared flow of a heterogeneous fluid in the presence of a constant gravitational field. Here we will simply summarize their main results.

Let $\rho_0(z)$ and $U(z)$ represent the undisturbed background distributions of density and horizontal velocity. Infinitesimal disturbances of the form $F(z) \exp\{ik[x-a(k)t]\}$ are governed by the linear differential equation

$$\frac{d}{dz}\left[\rho_0(U-a)^2 \frac{dF}{dz}\right] + \rho_0 \left[g\beta - k^2(U-a)^2\right]F = 0 , \qquad (3.1)$$

where g represents the gravitational force and

$$\beta(z) = -\frac{1}{\rho_0}\frac{d\rho_0}{dz} , \qquad N^2 \equiv g\beta . \qquad (3.2)$$

N is Brunt-Väisälä, or buoyancy frequency, and is the frequency (in rad/sec) at which a vertically displaced parcel oscillates. Equation (3.1) is sometimes called the Taylor-Goldstein equation (Taylor, 1931; Goldstein, 1931). When coupled with appropriate boundary conditions at the sea (or land) surface and at the tropopause [e.g., one choice is $F(0) = F(H) = 0$, since the vertical velocity is proportional to F] it may be considered a linear eigenvalue problem for $a(k)$, the eigenvalue. Miles and Howard proved that:

(i) the flow is not unstable if

$$g\beta - \frac{1}{4}\left(\frac{dU}{dz}\right)^2 > 0 \; ; \tag{3.3}$$

i.e., the local Richardson number must be less than 0.25 somewhere in the flowfield for instability.

(ii) If there are any unstable modes, with complex phase speed

$$a = a_r + i \, a_i \, , \qquad a_i > 0 \tag{3.4}$$

then

$$\alpha = \min_z [U(z)] < a_r < \max_z [U(z)] = \beta \, , \tag{3.5}$$

and

$$\left[a_r - \frac{1}{2}\,(\alpha + \beta)\right]^2 + a_i^2 < \left[\frac{1}{2}\,(\alpha - \beta)\right]^2 \, . \tag{3.6}$$

The last result is known as the semi-circle theorem.

3.2.1   Unstable atmospheric disturbances. It follows from Eq. (3.5) that associated with each unstable wave mode is at least one so-called critical layer, where $U(z^*) = a_r$; i.e., where the wave travels with the wind. The unstable modes are collectively referred to as stratified shear-flow instabilities when the density gradient provides a stable stratification, i.e., $\beta > 0$. The most extensively studied mode of instability is that associated with an inflection point in the velocity profile. This type is probably also the most prevalent stratified shear-flow instability in the atmosphere, and is frequently referred to as Kelvin-Helmholtz instability, although the latter is strictly confined to discontinuous velocity and

23

temperature profiles. In this report, we shall use the phrase Kelvin-Helmholtz (K-H) instability to denote the shear-induced instability associated with a confined layer of velocity and temperature gradient. A detailed study of the K-H instability is given in Appendix A. Equation (3.3) states that for unstable waves to exist, $Ri \equiv g\beta/(dU/dz)^2 < 0.25$ is a necessary, but not sufficient, condition. This condition, $Ri < 0.25$, has the physical meaning that the destabilizing effect of the mean shear must be greater than the stabilizing effect of the density stratification. In general, shear-induced waves are found in atmospheric regions where $Ri < 0.25$. Kelvin-Helmholtz instabilities commonly occur at high altitudes in the atmosphere (5 to 7 km) near the jet stream where velocity shears are large, and in the boundary layer (~ 200 to 1000 meters) where, again, one finds large shears. As this report is primarily concerned with clear air radar returns originating in the atmospheric boundary layer, only a brief discussion of K-H waves in the upper atmosphere will be given.

Reed and Hardy (1972) and Hooke and Hardy (1975) combined measurements from a sensitive 3 Ghz radar with surface microbarographs and conventional synoptic data to document a stratified shear-flow instability which occurred over the eastern seaboard. The waves possessed a wavelength and frequency of approximately 15 km and 300 seconds, respectively, and a horizontal phase velocity of about 45 m/sec. The instability was associated with the high shear region near the lower portion of the jet stream ($z \sim 8$ km), and a critical layer was found at $z \approx 9$ km. Radar returns on a RHI scan revealed a number of echo strata throughout heights of 8 to 10 km. The returns appeared as undulating strata and returns near the critical level showed the "cat's eye" pattern typical of K-H waves, as shown in Figure 3.5. The waves are vertically trapped with amplitudes decaying away from the critical level; typically velocity fluctuations are negligible 1 km above or below the critical layer. Two more recent studies of unstable waves in the upper atmosphere were carried out by VanZandt, Green, Clark, and Grant (1979), and Klostermeyer and Ruster (1980), using doppler radar. The dynamics of the waves observed by them were similar to that just described, but both noted the feature of "power bursts". These bursts were due to enhanced radar returns
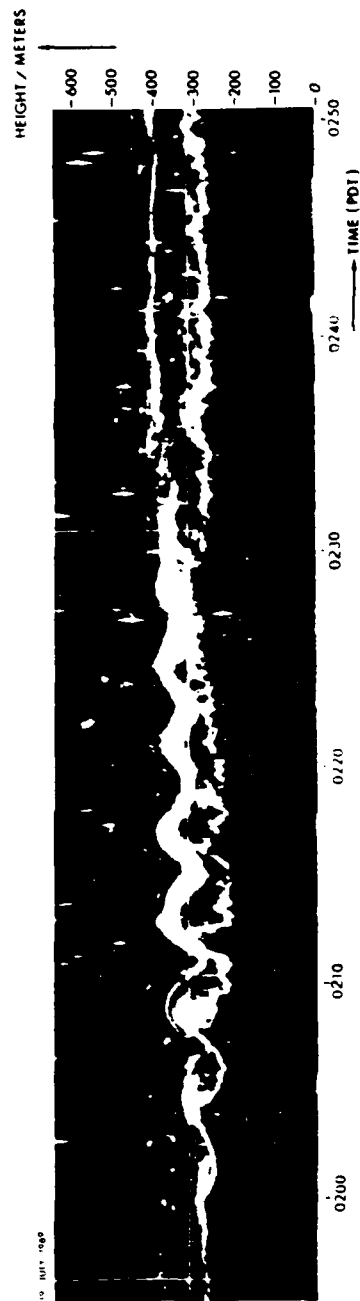
Figure 3.5(a) - Radar observation of a breaking Kelvin-Helmholtz instability (from Gossard, et al., 1971).

25
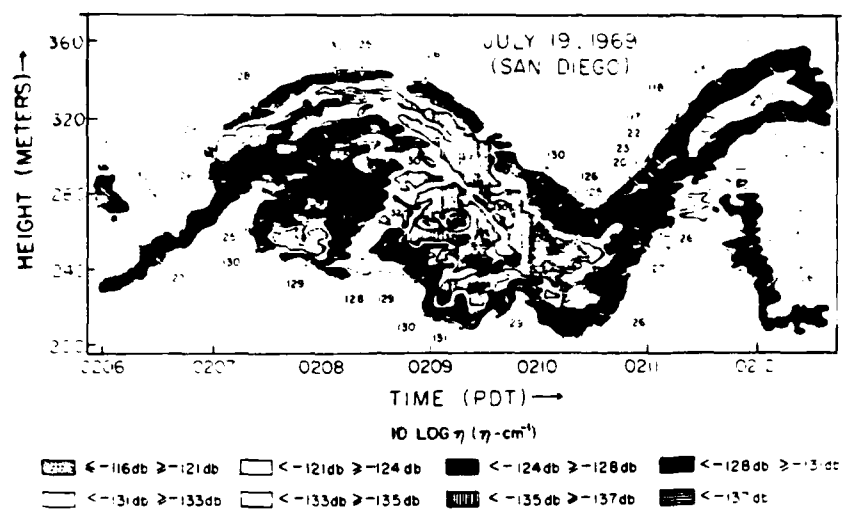
Figure 3.5(b) - Reflectivity contour of the preceeding
radar observation.

from localized regions of wave overturning. That is, the instability grew to the point where heavy fluid was advected over light fluid; this statically unstable situation then generated high levels of turbulence and C_n^2 locally. This development will be demonstrated in the model calculations of Appendix A.

Next we discuss wave phenomena in the atmospheric boundary layer which can give rise to clear air radar returns. Pioneering work in probing the lower atmosphere with high resolution radar was done by Richter and co-workers, who developed a high-sensitivity, high resolution radar system at the Naval Electronics Laboratory Center in San Diego. The radar operated at 2.9 Ghz and radar measurements were made along the San Diego coast. The atmospheric boundary layer in this region is characterized by a stable inversion, typically above 200 to 300 meters, and wind speeds of order 1 m/sec. The principal results of Richter and co-workers studies are given in three papers: Gossard, Richter and Atlas (1970); Atlas, Metcalı, Richter and Gossard (1970); and Gossard, Jensen and Richter (1971). These papers treat various phenomena responsible for clear air radar returns, and we will first discuss shear instabilities. These instabilities typically occurred near the base of the inversion (i.e., near the top of the mixed layer), $Z_I \sim 200$ to 400 meters, and temperature-velocity soundings showed this region to be one with critical, or near critical, Richardson numbers. The waves appeared on a RHI scan as well-defined rolls with peak to peak amplitudes of up to 100 meters. Typical wavelengths and periods were 200 meters and 250 seconds, respectively, and phase velocities were of order 1 m/sec. Again, critical layers were present where the phase velocity equaled the mean velocity ($z \sim 200$ to 400 meters). Superimposed on the rolls were small scale perturbations due to overturning (localized regions of static instability). These perturbations represent the same phenomena which gave rise to the "power bursts" in the study of upper atmospheric K-H waves. Evidence of long period internal gravity waves was found in all of the above studies, and it was proposed that these waves were instrumental in triggering the shear instabilities; the mechanism is as follows. The base of an inversion (or top of a mixed layer) typically has a mean velocity shear. Situations can exist where the Richardson number is marginally stable (Ri slightly above 0.25), and the shear

of a propagating internal wave can add to the background shear, driving the Richardson number below 0.25. We return to this scenario in Section 3.2.2.

A number of other observations of waves in stratified shear flows can be found in the literature. Noonkester (1973) compiled data on a total of 44 wave events which occurred over the Southern California coastal region. Hooke, Hall and Gossard (1973) observed waves over Colorado using acoustic sounders and an instrumented tower. Generally in boundary layer studies, wavelengths are on the order of several hundred meters, which is about 6 to 10 times the thickness of a typical shear layer, and phase velocities are a few meters per second, corresponding to a typical mean wind velocity. A fairly complete list of observations of shear instabilities can be found in a review article by Ottersten, Hardy and Little (1973).

We also note that an interaction between the convective cells considered in Section 3.1 and the stable layer capping the boundary layer can also give rise to K-H instabilities. When there is significant wind shear in this stable layer as is often the case, the individual convective cell protruding up into this layer forms a hummock with increased shear across the top of it. K-H wave-breaking has also been observed at the top of these hummocks (Browning, et al. 1973). Due to the vertical wind shear the resulting regions of enhanced C_n^2 will move at a velocity different from the wind velocity in the mixed layer.

3.2.2   <u>Stable wave modes.</u> Equation (3.5) states that in the absence of external forcing, <u>any</u> <u>wave</u> <u>whose</u> <u>speed</u> differs <u>from</u> <u>the</u> <u>wind</u> <u>everywhere</u> (<u>i.e.,</u> <u>for</u> <u>all</u> <u>z)</u> <u>cannot</u> <u>be</u> <u>unstable</u>. This allows atmospheric disturbances to be divided into: (i) plumes of various sorts, all of which are carried (horizontally) by the wind; (ii) unstable traveling waves, each of which travels with the wind at its own critical level; and (iii) neutrally stable traveling waves, which do not travel with the wind at any level. Categories (i) and (ii) have been discussed in our treatment of thermals and shear-induced waves, respectively. The stable atmospheric disturbances of category (iii) will now be considered.

28

The derivation of Eq. (3.1) was based on the assumptions that the atmosphere is incompressible and dry. We may relax these assumptions if we require that:

(i) the motion is isentropic;

(ii) the specific humidity, q, of each fluid particle is conserved during the motion (i.e., no condensation or evaporation occurs);

(iii) the moist air is a perfect gas, with gas constant

$$R = R_a [1 + 0.61 q_0(z)] \tag{3.7}$$

where R_a is the gas constant for dry air, and $q_0(z)$ is the background distribution of specific humidity (e.g., see Holmboe, Forsythe, and Gustin, 1943).

It is convenient to define the virtual temperature

$$T_0^*(z) = [1 + 0.61 q_0(z)] T_0(z) , \tag{3.8}$$

where $T_0(z)$ is the background temperature. Then an analysis similar to those of Miles and Howard leads again to Eq. (3.1), provided we replace $\beta(z)$ in Eq. (3.2) with

$$\beta(z) = \frac{1}{T_0^*} \left[\frac{dT_0^*}{dz} + \frac{g}{c_{pa}} \left(\frac{1 + 0.61 q_0}{1 + 0.90 q_0} \right) \right] , \tag{3.9}$$

where c_{pa} is the specific heat of dry air at constant pressure. As before, static stability requires $\beta > 0$, while dynamic stability is assured if Eq. (3.3) holds. Moreover, it follows again from Eq. (3.5) that only neutrally stable waves can travel at speeds different from the wind.

For convenience, we have represented the tropopause (at z = H) by a rigid lid [i.e., F(H) = 0]. However, no qualitative changes occur if the tropopause is represented by a free surface. In particular, it remains true that in the absence of external forcing, only neutrally stable gravity waves can travel at speeds different from the wind at all levels. This is a fundamental feature of propagating gravity waves.

As examples, let us consider two special cases of $\beta(z)$ and $U(z)$ which have application to the atmosphere. The first is the case of constant $\beta(z)$, and we take U = 0 for simplicity. The solutions to Eq. (3.1) are

$$F_{\pm} = F_0 \exp(\pm imz) , \tag{3.10}$$

which represent freely propagating disturbances. In the case of rigid boundaries at z = 0 and z = H, a linear combination of the two solutions satisfies the boundary conditions. The dispersion relation for these disturbances is

$$\omega^2 \equiv k^2 a^2 = \frac{g\beta k^2}{k^2 + m^2} = \frac{N^2 k^2}{k^2 + m^2} , \tag{3.11}$$

from which it follows that $|\omega| \leqslant N$ and that $|\omega| \to N$ as $m/k \to 0$, $|\omega| \to 0$ as $k/m \to 0$ display this. One may show that horizontally propagating waves are long waves (k $\ll$ m); see Mowbray and Rarity (1967).

A second form of β applicable to the atmosphere is one which models an atmosphere often observed over the ocean, and similar to the environment studied by Richter and co-workers at San Diego. The region from approximately 200 to 1000 meters is very stably stratified, while the region above 1000 meters is less so. We take the following form for $N(z) = [g\beta(z)]^{1/2}$,

30

$$N(z) = N_L \qquad 200\,m < z < 1000\,m \,,$$

$$N(z) = N_u \qquad 1000\,m < z \,,$$

where $N_L > N_u$ and the subscripts denote lower and upper, respectively. As above, we assume $U(z) = 0$. A set of eigenfunctions exist with $N_u < \omega < N_L$. These solutions oscillate in the region $200m < z < 1000m$, and decay exponentially for $z > 1000m$. Such waves are "ducted" modes. A set of eigenfunctions also exists with $\omega < N_u$, and these disturbances can freely propagate throughout the atmosphere. Both types of waves, freely propagating and ducted, are commonly found in the atmosphere. The former are low frequency disturbances [$\omega < N(z)$ through the atmosphere], while the latter are high frequency modes which cannot propagate into regions where $\omega > N(z)$.

The preceeding discussion excluded any mean velocity. However, in the case of constant $U(z)$, it follows from Eq. (3.1), that the effect of the mean flow is merely to "doppler-shift" the frequency of the wave relative to a stationary observer. The problem becomes more difficult to solve when shear exists ($\partial U/\partial z \neq 0$), but for cases where $a \gg U$, the effects of $U(z)$ will not be dramatic. On the other hand, if $U(z) = a$ somewhere in the flow, we may anticipate the unstable waves previously discussed.

The existence of propagating internal gravity waves in the atmospheric boundary layer has been documented by Gossard, Jensen and Richter (1971). In certain cases, multi-layered structures appeared on RHI scans which could be interpreted as marking the crests of a propagating wave. As the clear air returns marked regions of enhanced C_n^2, Gossard, et al. (1971), investigated mechanisms which might provide increased turbulence for a propagating internal wave. The first mechanism investigated was that of wave overturning, where the amplitude of the wave is large enough to advect heavy fluid over light, thereby creating localized regions of static instability. Data did not support this mechanism as balloon soundings showed no evidence for thermal

(convective) instability at the heights of radar returns. Gossard, et al., did find that a high resolution (of order of meters) inspection of the echo bands revealed a sub-structure remarkably similar to that seen in large scale shear-induced instabilities. Gossard, et al., proposed that internal waves propagate into a region possessing sub-critical ambient shear, and that the sum of wave shear plus ambient shear creates a dynamically unstable situation (Ri < 0.25). They argued that the conditions for this dynamic instability will occur before the onset of a convective instability and the dynamic instability are responsible for the layered radar returns. These arguments were refined and extended in a later work by Gossard, Richter and Jensen (1973). We believe that this mechanism is a prime candidate for clear air radar returns which propagate at velocities significantly different from the local wind velocity. Internal waves typically can have phase velocities much greater than the local wind speed and arbitrary directions with respect to the local wind. They can create regions of critical Ri which propagate at their phase speed, giving rise to propagating regions of dynamic instability and enhanced C_n^2. As long as the characteristic time for the evolution of the wave breaking generated in this unstable region is smaller than the time required for the wave to travel through the region, the region of enhanced C_n^2 will appear to propagate with the speed of the wave. This evolution of the breaking wave is studied in detail in Appendix A. Given the demonstrated ability of internal gravity waves to produce clear air returns, and the proposed way in which internal waves can give rise to rapidly moving radar returns, we proceed to discuss the observations and production mechanisms for internal gravity waves in the atmosphere.

Freely propagating gravity waves have been observed by a number of workers, and Jordan (1972) studied waves generated by winds and storms in the Colorado area using a ground based array of microbarographs and anemometers. Certain wave phenomena were related to topography, such as mountain lee waves, while other pressure oscillations were due to shear instabilities associated with either the jet stream or the shear due to frontal systems. In addition, Jordan observed internal gravity waves generated from summer thunderstorms with periods of order 20 to 30 minutes, wavelengths of order 30 km, and

32

horizontal phase speeds of order 30 m/sec. Jordan also observed pressure pulses on the microbarographs which were followed by high frequency (periods of a few minutes) oscillations. Two mechanisms for wave generation were offered by Jordan. The first proposed was that the downdraft cells of a thunderstorm impinge on the boundary layer inversion which perturbs the region and excites internal waves. The second mechanism involves the updraft region of the thunderstorm, where fluid can be carried above its equilibrium position. Fluid parcels will "overshoot" equilibrium levels and perturb the surroundings, which will excite internal waves. A visual display of internal gravity waves due to a severe thunderstorm can be found in the satellite pictures of Erickson and Whitney (1973). Bands of internal waves propagate out from a storm located in the Southern Great Plains. The wavelength is approximately 5 to 10 km, and the clouds are estimated to be at mid-tropospheric levels ($\sim$ 4 to 5 km), so that one has a picture of internal gravity waves extending throughout the troposphere and propagating away from the storm. Uccelini (1975) used synoptic data to infer the existence of very long wavelength, low frequency waves associated with a severe midwest storm. Wavelengths and periods were approximately 400 km and 2 hours, respectively, which corresponds to a phase velocity of approximately 40 m/sec. Gossard, Richter and Atlas (1970) observed internal gravity waves on the San Diego coast using radar and ground based microbarographs and anemometers. Wave periods ranged from 7 to 20 minutes, and very large amplitudes were observed. An echo layer at approximately 200 meters showed peak to peak amplitudes of up to 100 meters. The wave form was highly distorted due to non-linear effects with steepened crests and flattened troughs. No evidence of wave breaking was found even with this high degree of non-linearity. Wavelengths and phase velocities ranged from 3 to 7 km and 2 to 7 m/sec, respectively. These phase speeds always exceeded the mean winds, so that no evidence was found for critical layers. Gossard, et al., also speculated on the wave source and noted that thunderstorms were present some 500 km from their instruments. More recent studies have added to the evidence for storm generated internal waves. Oliver (1981) discusses satellite data taken over the eastern Pacific which clearly shows waves originating in the vicinity of strong fronts and propagating toward the equator. Gedzelman (1981) analyzed wave events at

33

Palisades, New York, covering a one-year period. Approximately one-half of these events could be traced to shear instabilities. Most of the others were found to propagate at velocities significantly different from the mean wind aloft and, in some cases, could be traced to thunderstorm activity.

To summarize, thunderstorms are a common source of freely propagating gravity waves in the atmosphere. They are by no means the only source of these waves. In the lee of large mountain ranges, such as the Rockies and the Sierras, large amplitude lee waves are common and are well documented (e.g., Lilly and Toutenhoofd, 1969; Lilly, 1971). On a smaller scale, lee waves also may be generated in the lee of heat sources, such as a city over land (e.g., Wurtele, 1955) or an island in the ocean. One mechanism for generation that is relatively rare was identified by VanDorn (1964). He noted that the deformation of the earth's surface by the Alaska earthquake of 1964 created an "atmospheric tsunami" that was observed as far away as northern California.

The existence of ducted, or trapped, internal waves has been well documented by Metcalf (1975), who used an instrumented aircraft in conjunction with radar and balloon soundings to study waves near the San Diego coast. Radar returns showed that the low level inversion oscillated almost continuously, while analysis of aircraft temperature and velocity records revealed the presence of internal waves with wavelengths and periods ranging from 40 to 700 meters and 0.50 to 1.50 minutes, respectively. Nearly all of the observed waves were trapped within the high buoyancy frequency region of the inversion, and wave propagation occurred in nearly all horizontal directions. Phase speeds ranged from less than 1 m/sec to over 20 m/sec, and, as in previous studies, no evidence for critical layers was found. Stilke (1973) observed ducted internal gravity waves over Hamburg, Germany, using an instrumented tower. Wave periods ranged from approximately 4 to 20 minutes with peak to peak amplitudes of up to 100 meters. Sethuraman (1977, 1980) observed internal waves using an instrumented tower at Long Island, New York. A strong inversion was present due to the advection of warm air from land over the cold water. These waves had periods of order 5 to 10 minutes, and Sethuraman estimated wavelengths and phase speeds to be in the 4 km and

4 m/sec range. The phase speeds were far greater than the mean wind, and this excluded the existence of critical layers. Sethuraman observed periods of persistent high levels of turbulence, lasting well over an hour, and this is in contrast to the frequently observed short-lived turbulent bursts. The measurements were not detailed enough to yield information of the generation mechanism or the physics of the persistent turbulence, and Sethuraman did not speculate on either of these.

3.3 Characteristic Features of Long Internal Gravity Waves

These observations demonstrate that gravity waves are common in a stably stratified atmosphere. Moreover, many of the waves that were observed were significantly longer than height of the tropopause for freely propagating waves, or than the duct height for ducted waves. In this section we discuss some of the characteristic features of long internal gravity waves, so that they may be identified easily. In particular, we consider the following questions:

(i) Do these waves have any distinguishing features (e.g., shape) that would help to identify them?

(ii) How long do they persist?

The question of their generation has already been discussed. The relation between the amplitude of an internal gravity wave and the intensity of the resulting radar signal may be obtained from Appendix A.

The equation governing the horizontal propagation of long wavelength, small amplitude, two-dimensional waves is the linear wave equation,

$$\frac{\partial^2 \phi}{\partial t^2} = a^2 \frac{\partial^2 \phi}{\partial x^2} \tag{3.12}$$

where a is the speed found from Eq. (3.1) for the appropriate mode. [Recall that the vertical structure was determined by Eq. (3.1).] The waves are a few kilometers long, and Eq. (3.12) governs their propagation over distances of

35

tens of wavelengths (e.g., distances less than 100 km). In particular, Eq. (3.12) applies over the field of vision of most radars. It is well known that

$$\phi(x,t) = f(x - at) \tag{3.13}$$

solves Eq. (3.12) for any function f. Because f is arbitrary (being determined by initial conditions), it follows that no particular wave shape is preferred by Eq. (3.12). Thus, the simplest answer to question (i), above, is negative.

In the atmosphere, long internal gravity waves that are approximately two-dimensional have been observed to propagate over hundreds of kilometers (e.g., Christie, Muirhead, and Hales, 1979; Clarke, Smith, and Reid, 1981). Equation (3.12) is inadequate to describe the propagation of these waves over very long distances, because small but cumulative effects that were omitted from Eq. (3.12) eventually have enough time to exert a measurable influence. For example, Grimshaw (1980) has shown that in a moist, compressible atmosphere, long waves of small amplitude propagate according to Eq. (3.12) on a short time scale, and according to the Korteweg-deVries equation,

$$u_\tau + 6uu_\chi + u_{\chi\chi\chi} = 0 , \tag{3.14}$$

on a long time-scale. Here $\chi = x - at$, τ is a slow time (or space) scale, and u is proportional to ϕ in Eq. (3.12). The assumptions underlying Eq. (3.14) are that weak nonlinearity and weak dispersion are of equal importance, and that both dominate weak three-dimensionality, weak dissipation and slow changes in topography (including the height of the tropopause).

If weak three-dimensionality is as important as the nonlinearity, then Eq. (3.14) should be replaced by the Kadomtsev-Petviashvili equation,

36

$$(u_\tau + 6uu_\chi + u_{\chi\chi\chi})_\chi + u_{\eta\eta} = 0 , \tag{3.15}$$

where η is measured along the crest of the wave (e.g., see Kadomtsev and Petviashvili, 1970; or Ablowitz and Segur, 1979). Other balances are possible as well.

Equations (3.14) and (3.15) are among a class of special nonlinear partial differential equations that can be solved exactly. In particular, both equations have N-soliton solutions [for (3.14), see Gardner, Greene, Kruskal, and Miura, 1967, 1974; for (3.15), see Zakharov and Shabat, 1974; and Satsuma, 1976]. The one-soliton solution for Eq. (3.14) is simply a solitary wave:

$$u(\chi,\tau) = \frac{K^2}{2} \operatorname{sech}^2 \frac{1}{2} K(\chi - K^2\tau + \chi_0) , \tag{3.16}$$

where K and χ_0 are arbitrary parameters. This solution is shown in Figure 3.6. It is also a solution of Eq. (3.15). In both cases, it represents a plane wave, traveling without change of form in the χ-direction. In the original coordinate system (x,t), it travels in the x-direction with a speed slightly faster than a in Eq. (3.12), and travels as a permanent wave over distances much longer than the range of validity of Eq. (3.12).

The relation between Eqs. (3.12) and (3.14) may be stated as follows. Consider a long, two-dimensional wave of small amplitude. Its vertical structure is given by Eq. (3.1), but its horizontal structure may be specified arbitrarily, provided only that it is made up entirely of long waves. It will propagate as a wave of permanent form, according to Eq. (3.12), over relatively short distances (less than 100 km, say). Over much longer distances, most of these waves will evolve slowly, according to Eq. (3.14) if weak nonlinearity and dispersion dominate in other small effects. The only waves that retain their shape over these large distances are solitary waves,
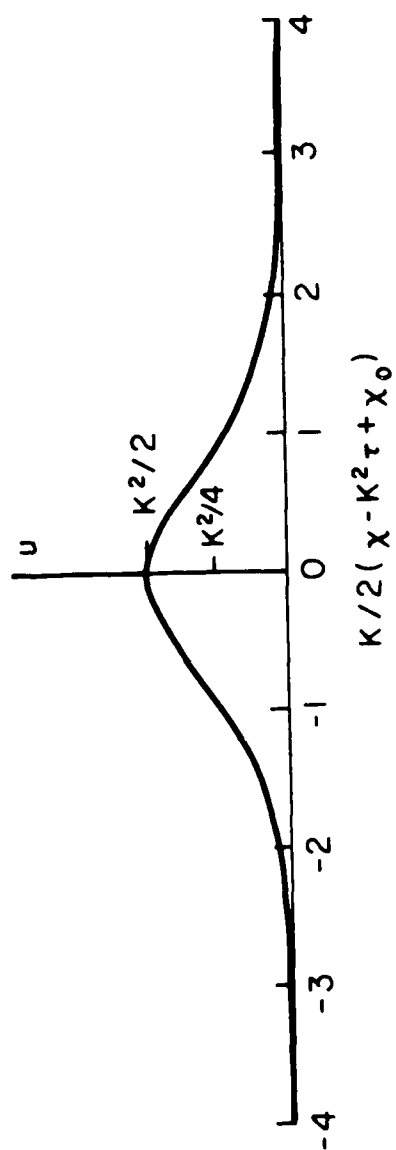
Figure 3.6 - Soliton solution of Eq. (3.15).

given by Eq. (3.16). A spectacular example of such a two-dimensional solitary wave in the atmosphere is discussed by Clarke, Smith, and Reid (1980). [For a detailed experimental study of the accuracy of Eq. (3.14) in the closely related problem of long gravity waves in shallow water, see Hammack and Segur, 1974, 1978.]

Now let us consider weakly three-dimensional waves, and Eq. (3.15). A two-soliton solution of Eq. (3.15) is

$$u(\chi, \eta, \tau) \quad = \quad 2 \frac{\partial^2}{\partial \chi^2} \ln \{1 + \exp(\phi_1) + \exp(\phi_2) + \exp(\phi_1 + \phi_2 + A_{12})\} ,$$

$$(3.17)$$

where

$$\phi_i \quad = \quad K_i(x + p_i \eta - C_i \tau) , \qquad C_i \quad = \quad K_i^2 + p_i^2 , \qquad i = 1, 2$$

and

$$\exp(A_{12}) \quad = \quad \frac{3(K_1 - K_2)^2 - (p_1 - p_2)^2}{3(K_1 + K_2)^2 - (p_1 - p_2)^2} .$$

The pattern of the wave crests in the χ-η plane (i.e., in the x-y plane, scaled appropriately) is shown in Figure 3.7, for a particular choice of the parameters. This entire pattern moves in the x-direction as a wave of permanent form. More complicated wave patterns have been considered in detail by Anker and Freeman (1978).

We are not aware of any observations in the atmosphere of long internal gravity waves that resemble the pattern shown in Figure 3.7. However, Eq. (3.15) also describes the evolution of surface gravity waves in shallow

Figure 3.7 - Sketch of two-soliton solution of Eq. (3.16).
In this symmetric case, $K_1 = K_2$, $p_1 = -p_2 > \sqrt{3} K_1$.
This pattern moves in the x-direction with speed $(K^2 + p^2)$.

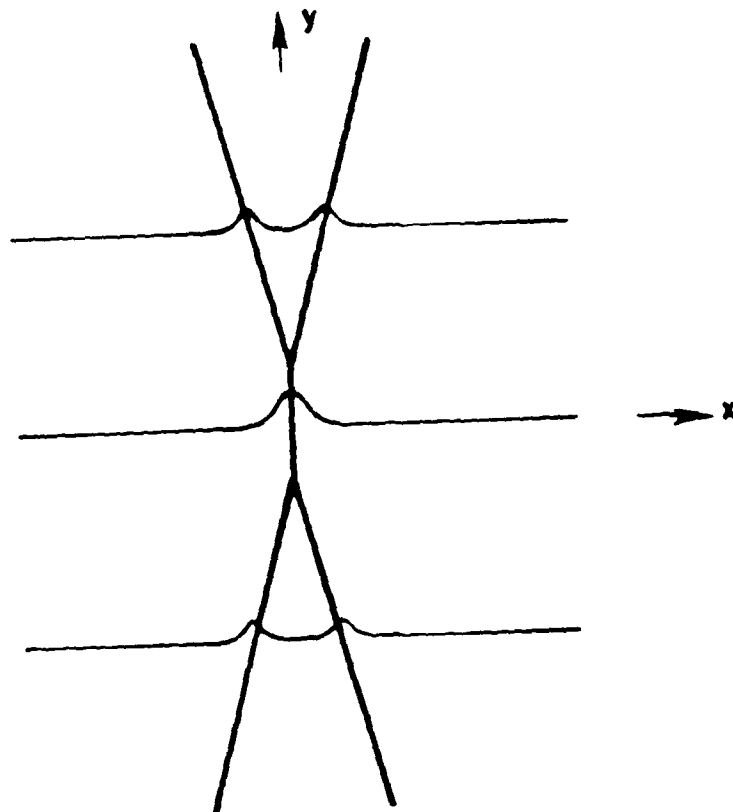water (here "shallow water" is equivalent to "long waves"). In shallow water such waves have been observed, as may be seen in Figure 3.8. They occur commonly on beaches of very gentle slope, with waves that are too small to break. There seems to be no reason why they should not occur in the atmosphere as well.

An interesting feature of the waves shown in Figure 3.8 is that these waves are breaking only in the relatively small region of intersection, where the wave amplitude is larger (roughly because the amplitudes of the two waves add in this region). The level of turbulence in this localized breaking region, therefore, should be significantly higher than anywhere else in the entire wave pattern. Consequently, a measuring device that responds only to very short wavelengths, such as a radar, is likely to ignore the long-crested waves, and to "see" only the localized region of intersection. Thus the radar return would show a three-dimensional target even though the waves that produced it are primarily two-dimensional.

Generating mechanisms for these waves were discussed in the previous section. From the viewpoint of the radar operator, however, the specific generating mechanism may be unimportant. Because the waves propagate over long distances, they need not be related to any features within the operator's field of vision, such as anomolies in the temperature of the sea surface. He sees only waves that propagate across his field of vision without any significant change of form. If the waves were generated only moderately far away, their shape will bear the signature of the generating mechanism. If they were generated very far away, they may have evolved into solitons. There seems to be no reason to expect that solitons should appear more often than other long waves, however, unless it is known that all sources of these waves are very distant. [Conceivably an operator in Hawaii would see solitons relatively often.] From the operator's standpoint, the most important features of these long internal gravity waves are that they travel relative to the wind at all levels, and that they evolve very slowly, if at all.

Figure 3.3 - Oblique interaction of two shallow water waves, taken off the coast of Oregon. (Photograph courtesy of Toedtmeier and No Nukes Calendar, 1979.)

Turbulence intensities produced by such waves are likely to be associated with the incremental shear added by the wave forcing the local value of Ri to decrease below 0.25 leading to the K-H instability detailed in Appendix A.

3.4 Review: Possible Sources of Clear Air Radar Returns in the Marine Boundary Layer

The preceeding discussion has focused on the various mechanisms which can give rise to clear air returns and details some observations of such phenomena. We conclude this section with a review of these phenomena in outline format. The phenomena are first grouped according to whether they will or will not travel with the ambient wind. This is followed by a cross referencing according to various other observable features. Our goal is to provide the reader with a way to discriminate between flow types based on the observed characteristics of the radar target.

I. Clear air returns which travel with the local wind velocity.

A. Convective phenomena associated with the statically unstable boundary layer.
   (1) Individual convective cells; horizontal size: 50 to 2000 meters, lifetime: 20 to 40 minutes.
   (2) Bénard cell pattern, collective motion of individual cells, size: 5 to 10 km; lifetime: several hours.
   (3) Thermal streets, collective motion of individual convective cells, bands of thermals aligned with mean wind; spacing between bands: 1 to 8 km; lifetime: several hours.

B. Kelvin-Helmholtz Instabilities.
   (1) Unstable waves associated with mean shears present in the atmospheric boundary layer. Wavelengths, periods and phase velocities of the order 100 to 400 meters, 100 to 300 seconds, and 1 to 5 m/sec, respectively, have been observed.

II. Clear air returns which travel at velocities different from the local wind. (Wave phenomena which can result in localized, propagating regions of turbulence.)

A. Tropospheric waves, propagating internal gravity waves which extend throughout the troposphere. Observed horizontal wavelengths; 5 to 400 km; periods 5 to 100 minutes; and phase speeds: 5 to 50

m/sec. Common mechanisms for wave excitation are storms and fronts.

B. Ducted waves. Internal waves which are confined to the boundary layer due to strong inversions. Wavelengths: 50 to 1000 meters, periods: 30 to 500 seconds, and phase speeds: 1 to 20 m/sec.

C. Solitons. Long wavelength internal gravity waves of moderately large amplitude which are shape-preserving over long distances.

D. Individual convective cells in the presence of strong vertical wind shear.

III. Radar Returns which are Localized

A. Individual convective cells. Scale of such thermals ranges from 50 to 2000 meters depending on position within boundary layer.

B. Localized turbulence associated with internal gravity waves. Regions of small scale shear instabilities can appear which are associated with propagating waves. Computations show that the size of turbulence region should be of order $10 \, (\ell/\Delta u) \, C_{phase}$, where ℓ and Δu are the thickness and velocity difference of the locally unstable region, and C_{ph} is the phase velocity. Typical values for these parameters yield sizes of order 100 to 500 meters.

C. Solitons. The possible intersection of two solitary waves could lead to localized breaking and large C_n^2.

IV. Radar returns which are relatively short-lived.

A. Individual convective cells. Lifetimes range from 20 to 40 minutes, but near the end of its existence, cell begins to break up. Therefore, one may only have a trackable entity for times of order 20 minutes.

B. Localized turbulence associated with internal waves, same as category III.B. Turbulence lifetimes are of order $10 \, \Delta\ell/\Delta u$, and typical values yield times of order 1 to 10 minutes.

V. Radar returns which can be observed through the well-mixed boundary layer.

A. Individual convective cells are observable due to increased C_n^2 at their boundaries, and may be tracked throughout the boundary layer.

44

VI. Radar returns which will be most prominent near inversions, or mixed-layer tops.

   A. All types due to the increased humidity gradients typically found in this region.

VII. Radar returns influenced by surface conditions.

   A. Convective activity depends strongly on surface heating. Any surface mechanism which creates localized "hot spots" should lead to individual convective cells, while the creation of extended lengths of warm water over the ocean could give rise to collective motion of thermals.

   B. Topographic features or convective activity may trigger waves.

IV. Preliminary Analysis of NRL Results on in Situ Measurements
of Some Clear Air Returns

Radar returns from atmospheric disturbances were recorded during a series of field tests conducted at the AUTEC Weapons Range during May 13 to May 17, 1979. According to the Data Catalogue of Aircraft Measurements, prepared by Dr. Lothar Ruhnke of NRL, radar returns were observed during Flight #7 (afternoon of May 16) and Flight #8 (morning of May 17). As seen from Chapter III the characteristic most likely to provide discrimination between targets generated by wave breaking and those generated by convection is the speed of the target relative to the wind. In this chapter, we estimate the difference between convectively generated targets and wave generated targets that may have been present during these two flights. We will show that there exist neutrally stable gravity waves in the atmosphere, the characteristics of which are consistent with the observed radar returns, and which travel at the reported speeds. We emphasize, however, that the data available are sparse, so that these calculations are only suggestive.

Figures (4.1a,b) and (4.2a,b) show the vertical distributions of virtual potential temperature and specific humidity that were measured in the lower atmosphere during Flights #7 and #8, respectively. [The logarithmic derivative of the virtual potential temperature is approximately $\beta(z)$ in Eq. (3.9).] Note that in both cases there is the suggestion of a thin unstable layer next to the surface (as much as a few 10's of meters thick) capped by a mixed layer (i.e., $\beta \approx 0$) in the lower 800 meters or so of the atmosphere, with a stably stratified ($\beta > 0$) region above it. During Flight #7 the "mixed" layer is slightly stable but considerably less stable than the region above it. The stability measured above the mixed layer ($\sim 3°C/km$) is comparable to typical values in the entire troposphere. (For example, the lapse rate for the standard atmosphere is about 3.5°C/km.) The

Figure 4.1(a) - Vertical distribution of virtual potential temperature during Flight #7. Taken from Ruhnke (1979).

Figure 4.1(b) - Vertical distribution of specific humidity during Flight #7.   Taken
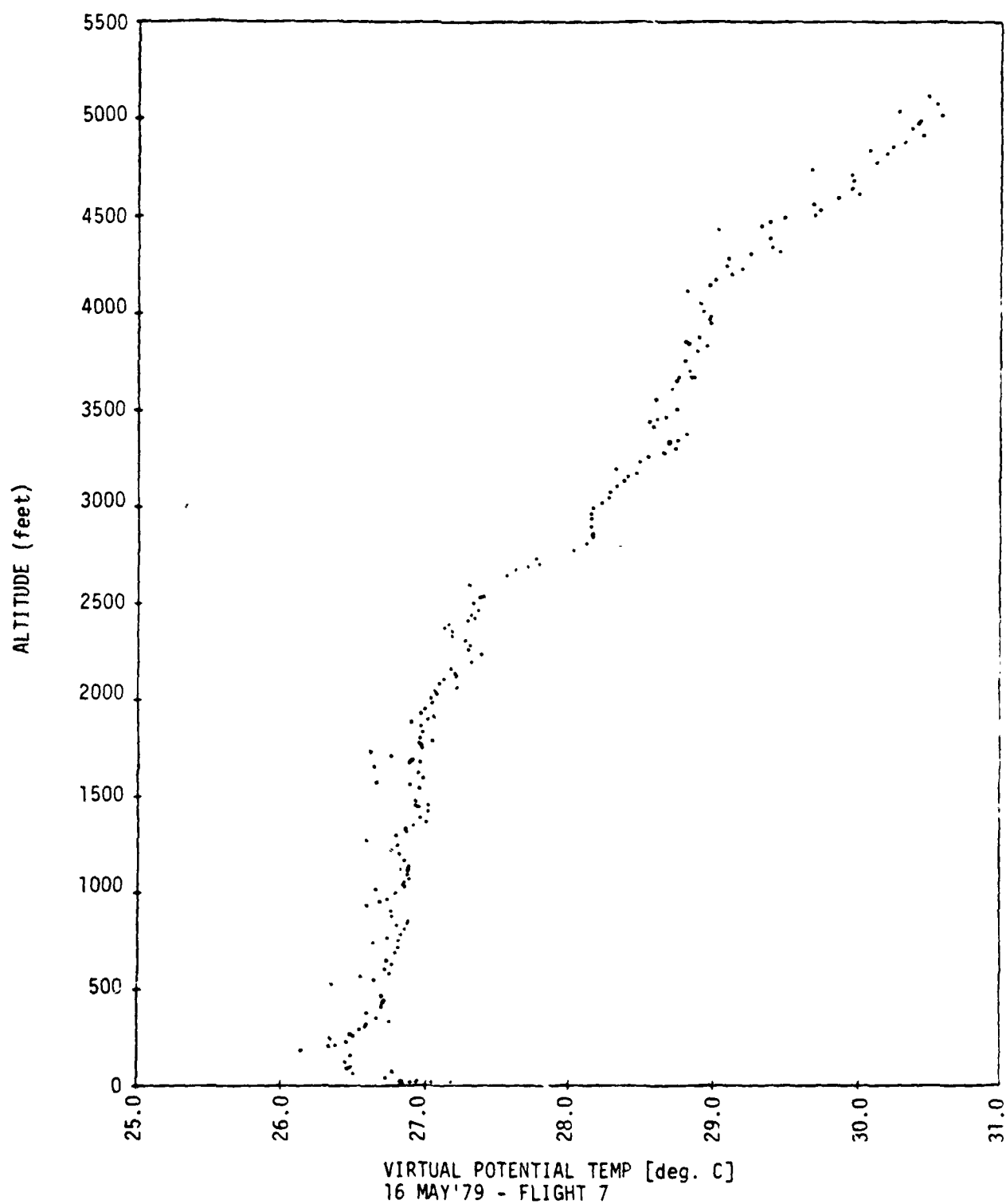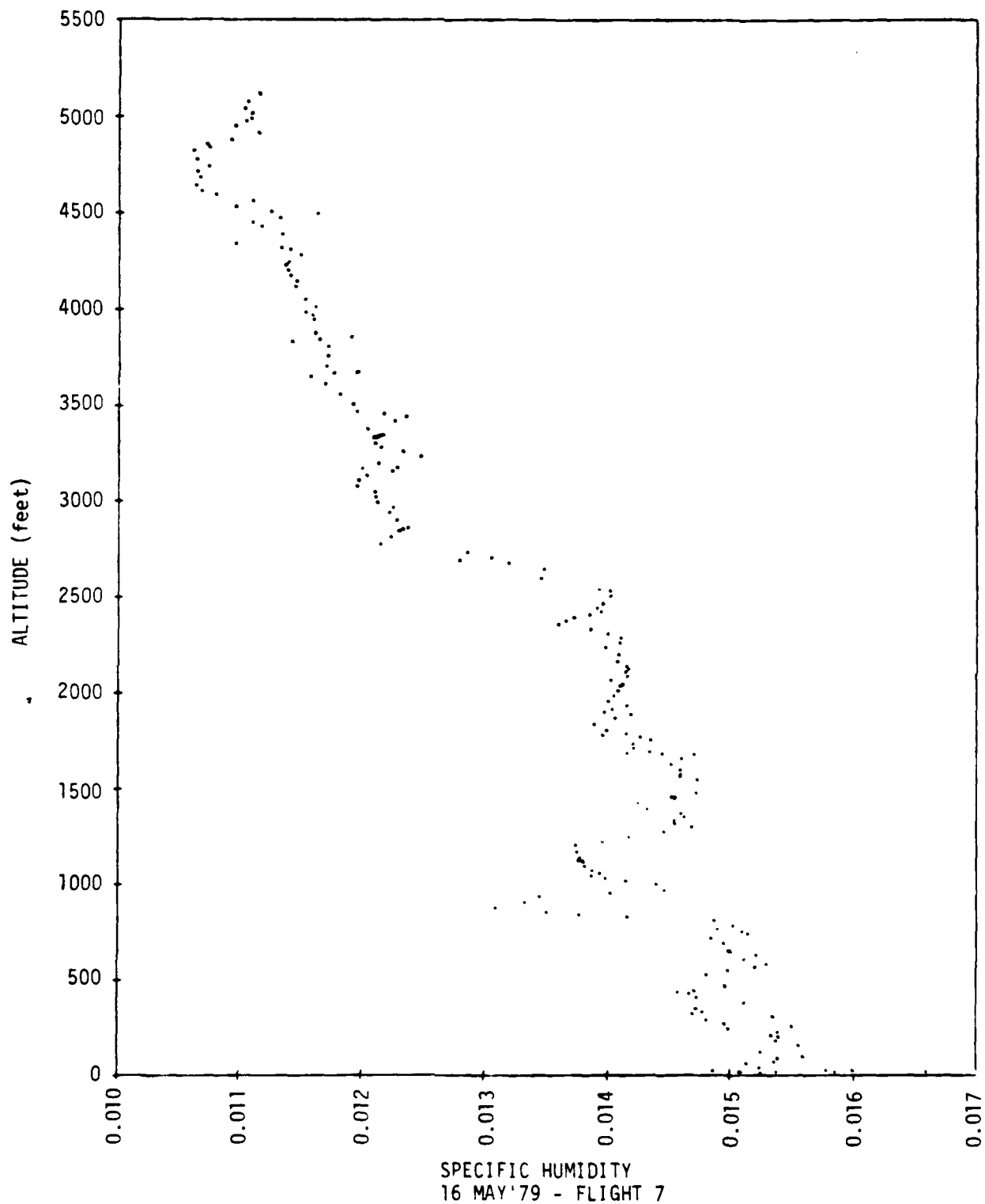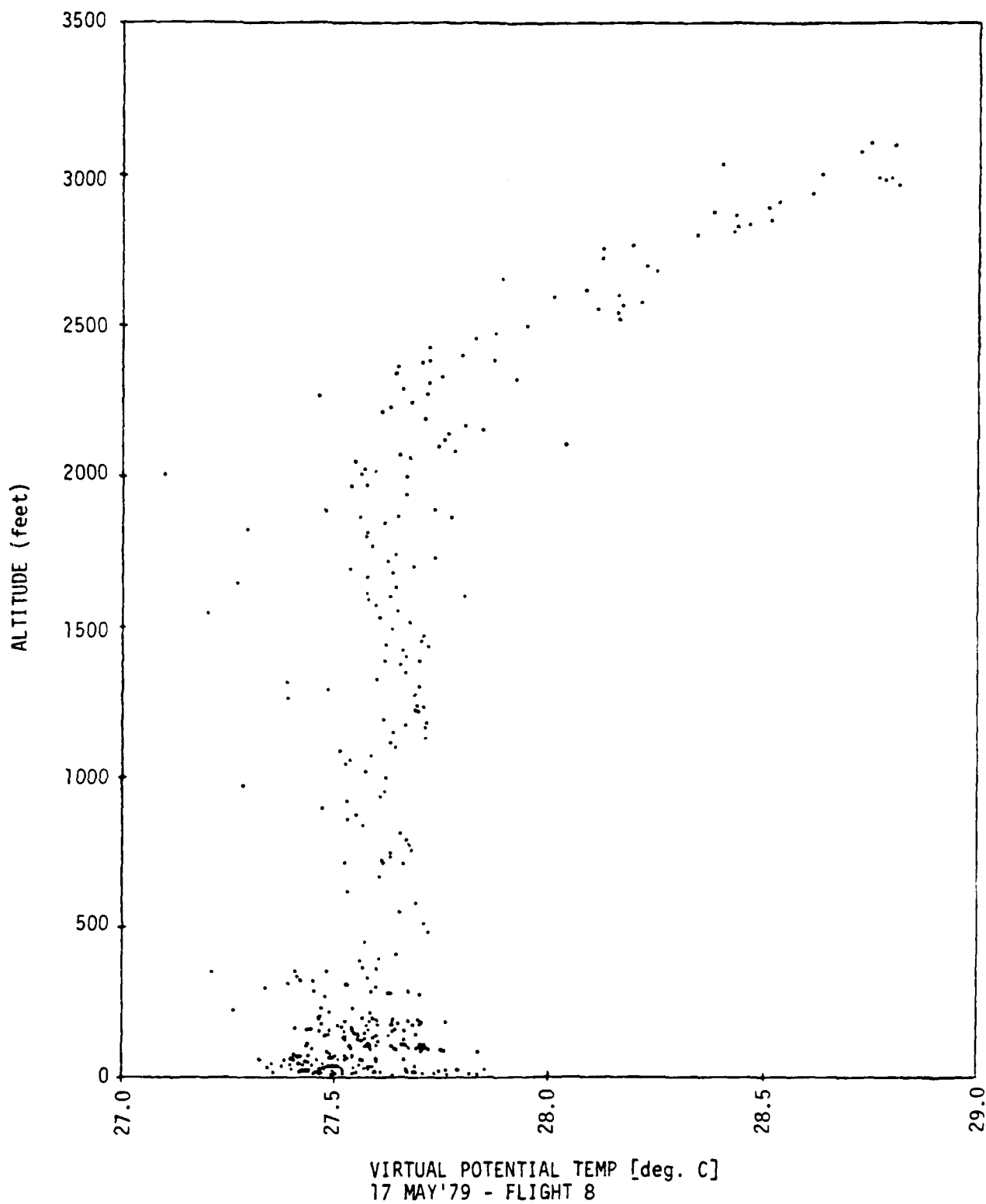from Ruhnke (1979).

Figure 4.2(a) - Vertical distribution of virtual potential temperature during
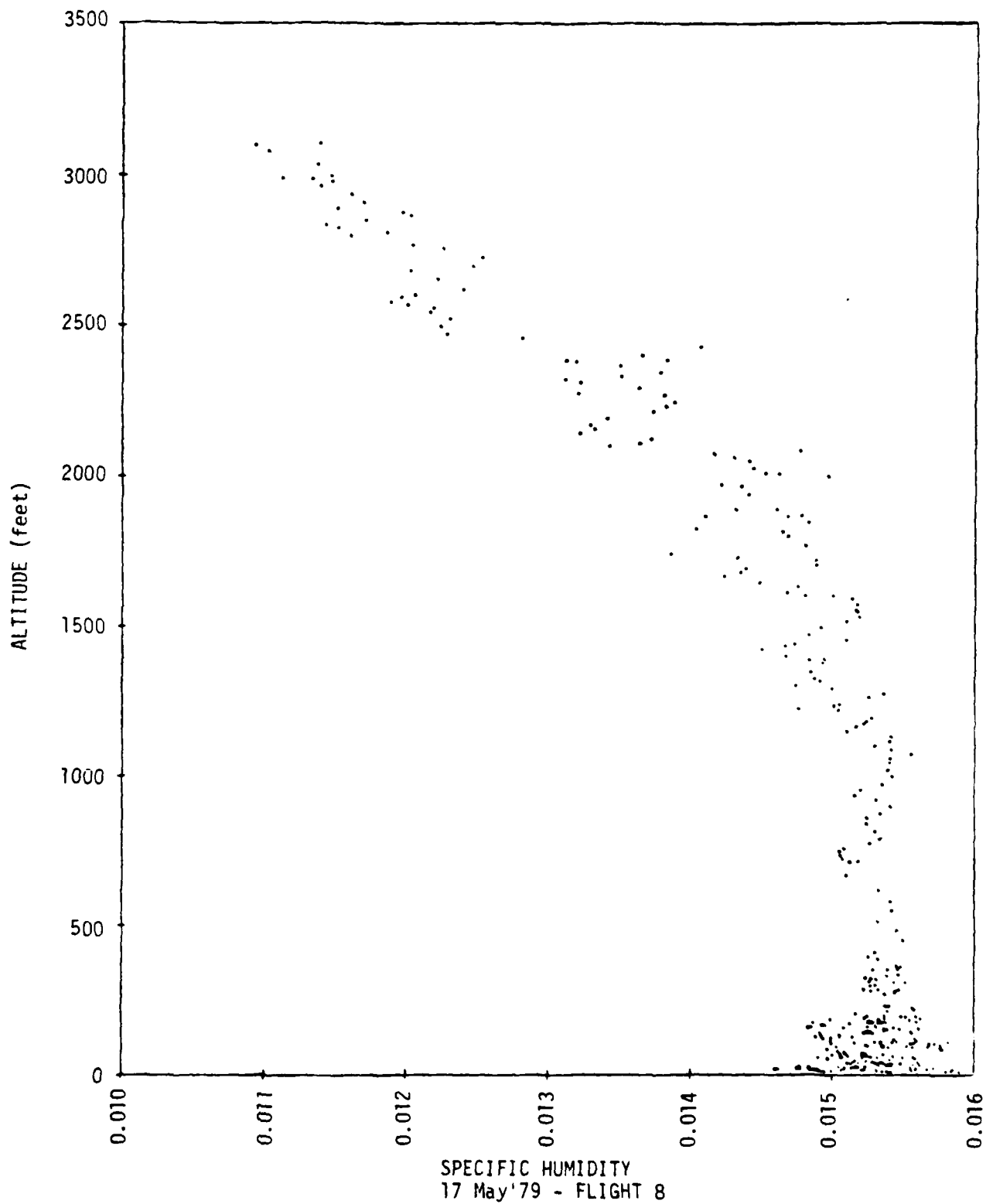Flight #8. Taken from Ruhnke (1979).

50

Figure 4.2(b) - Vertical distribution of specific humidi:y during Flight #8. Taken from Ruhnke (1979).

inversions capping the mixed layer on these two days should be considered weak, in comparison with much stronger inversions that have been measured (e.g., Metcalf, 1975).

As discussed in Chapter III, if there were a very strong inversion at the top of the mixed layer, then

(i) the gravity waves would be ducted within this layer, with exponentially decreasing amplitudes above it; and

(ii) their speeds would be determined primarily by the distribution of virtual potential temperature in the lowest 1 or 2 kilometers of the atmosphere (i.e., by the measured distributions).

However, because the measured inversions are so weak, neither of these statements is true. In particular, the measured distributions of stability in Figures (4.1a) and (4.2a) are inadequate to estimate wave speeds. The wave speeds we calculate below depend on an assumed distribution of stability in the entire troposphere and on an assumed location of the tropopause.

The observed features of the radar targets were the following:

(i) Location: They were observed near the top of the mixed layer (about 800 m).

(ii) Size and shape: The horizontal extent of a disturbance was 5 km or more. (An aircraft flying at about 50 m/sec traversed the target in about 100 seconds.) Some of the returns had a "crescent" shape.

(iii) Speed: Some of the targets travelled at speeds different from the winds. The available information on wind speed and direction in the lowest 2 km of the atmosphere is shown in Table 4.1. Typical wind speeds did not exceed about 6 m/sec (~ 12 knots). Some radar targets, on the other hand, travelled at speeds of 10-15 m/sec and in directions significantly different from the wind. Thus these targets travelled at speeds on the order of 5-10 m/sec relative to the winds.

Table 4.1 - Vertical distribution of wind direction (degrees from North) and wind speeds (knots) measured at AUTEC during May 14-17, 1979. Data from D. F. Hemenway.

Alt (Ft)	14 May 1927Z	14 May 2140Z	15 May 1815Z	16 May 1805Z	16 May 2217Z	17 May 1807Z	17 May 2114Z
1000	117/14.6	098/10.8	116/13.3	062/10.9			
1100	103/14.2	108/13.3	114/13.2	064/8.9			
1200	118/13.4	115/11.8	117/14.2	064/8.6	070/9.0		
1300	110/13.4	122/9.4	118/13.3	062/9.5	066/8.0		
1400	110/15.6	128/7.0	119/13.0	063/9.0	061/8.4		
1500	124/11.5	108/6.8	120/13.0	066/9.1	067/10.0	064/12.1	
1600	113/13.6	098/10.4	118/12.7	059/9.1	065/10.1	075/10.8	
1700	108/13.6	110/10.4	121/12.6	056/8.9	074/8.4	073/11.6	051/9.8
1800	122/10.6	123/9.5	123/12.0	055/8.2	070/9.9	062/12.8	057/9.4
1900	124/10.0	123/10.4	125/11.9	058/9.1	068/10.0	074/8.8	052/10.0
2000	130/7.3	124/9.0	126/11.8	057/8.6	079/11.4	083/9.4	-
2100	129/9.7	132/8.1	126/11.7	053/7.9	075/11.5	082/10.1	-
2200	120/12.8	133/9.7	126/11.6	053/8.4	073/11.1	078/10.3	047/10.2
2300	122/11.3	130/10.3	122/11.7	050/8.4	068/11.1	070/10.8	058/9.4
2400	129/10.7	130/11.1	127/11.6	056/7.9	061/12.3	080/10.9	052/10.6
2500	110/9.3	140/10.5	127/11.6	055/8.1	054/10.7	084/10.2	057/10.5
2600	120/6.4	140/9.7	126/11.4	053/8.3	037/10.1	064/11.4	051/10.1
2700	119/7.5	142/10.0	126/11.5	059/8.3	040/10.2	064/12.6	052/9.3
2800	125/7.4	142/10.7	125/11.4	061/8.1	052/9.9	069/13.1	048/10.9
2900	130/8.4	141/11.6	124/11.4	061/8.4	047/9.4	076/12.3	050/9.7
3000	125/9.5	139/12.1	120/11.8	066/8.0	034/8.9	063/12.8	049/9.5
3100	121/8.7	138/10.5	122/12.3	062/7.5	044/8.3	053/13.7	048/8.8
3200	111/8.7	138/10.1	120/11.9	060/8.1	054/8.3	055/12.6	050/8.5
3300	117/8.5	133/11.4	120/11.8	059/8.1	057/9.4	054/10.6	053/7.6
3400	125/8.8	132/10.9	117/11.2	056/9.1	056/9.4	053/9.9	055/7.5
3500	123/9.2	135/8.4	120/11.0	058/7.7	040/8.6	057/11.1	056/7.8
3600	119/7.6	149/8.3	119/10.7	055/8.6	028/9.1	049/13.7	054/7.9
3700	121/8.3	142/7.9	120/10.3	050/8.0	023/8.7	051/10.7	051/7.8
3800	137/11.3	157/9.0	119/10.3	053/7.4	023/8.4	058/8.2	056/8.3
3900	139/15.5	143/9.5	117/10.0	052/6.8	032/9.7	048/11.7	054/8.7
4000	126/16.4	127/10.0	121/9.4	061/6.9	031/8.8	054/11.5	053/9.7
4100	116/14.3	143/9.4	117/8.3	059/8.0	028/8.2	054/11.5	053/10.4
4200	118/13.4	140/10.6	116/8.5	066/7.2	023/8.1	058/10.9	049/10.8
4300	113/14.1	128/10.7	116/7.8	068/7.7	027/6.8	057/11.9	050/10.6
4400	120/12.2	136/10.4	120/8.0	069/6.8	016/7.7	048/14.2	046/10.6
4500	113/11.8	122/8.6	122/8.2	077/6.5	022/8.2	054/13.7	045/10.4
4600	112/13.2	110/10.4	122/8.5	078/7.2	037/7.0	066/12.8	042/10.0
4700	119/13.4	109/12.2	121/8.2	072/7.0	007/9.4	052/10.9	040/9.9
4800	121/13.8	106/9.9	118/7.9	076/7.3	016/8.4	044/10.9	038/9.7
4900	114/13.6	098/8.9	113/7.5	064/7.6	003/5.0	050/11.4	033/10.8
5000	098/13.6	103/8.0	108/8.1	072/8.2	003/7.4	047/13.2	033/10.2
5100	097/15.3	120/6.4	104/8.4	066/7.2	012/6.2	043/14.4	
5200	102/13.6	100/6.6	102/8.7	066/6.3	026/7.6	035/12.3	
5300	106/13.7	089/8.8	100/8.4	060/6.4	040/9.3	028/10.5	
5400	105/15.0	076/7.5	099/7.3	064/7.4	004/6.3	036/11.4	
5500	096/12.1	074/9.0	100/7.6	064/7.7	079/2.2	030/10.9	
5600	096/8.1	083/8.7	098/7.1	066/7.6	060/6.1	036/10.4	
5700	094/7.5	079/7.8	092/7.4	069/6.7	009/8.2	026/11.0	
5800	094/6.7	065/9.0	094/7.3	069/6.6	000/8.1	038/11.9	
5900	101/7.8	046/7.5	096/6.5	064/7.0	020/5.5	040/12.6	
6000	186/6.9	076/6.5	100/6.2	061/7.1	040/4.6	039/12.6	
6100	073/6.0	064/6.3	096/5.5	057/7.1	011/3.9	017/12.6	
6200	092/5.5	059/7.0	090/6.2	056/7.8	017/5.7	021/11.3	
6300	089/5.2	059/7.5	091/6.7	052/7.5	021/6.9	030/9.3	
6400	062/5.7	049/6.9	082/5.8	044/6.9	015/6.1	030/10.1	
6500	043/5.9	045/7.3	071/4.9	050/7.1	018/5.3	029/13.4	

There is a high probability that numerous convective cells existed on these two occasions. Figures 4.1a and 4.2a show that an anomalous warm spot on the surface of as much as a few tenths of a degree should be adequate to induce a buoyant cell with sufficient buoyancy to rise to heights of 800 meters or more. The evaporative cooling of the ocean surface suggested by Figures 4.1b and 4.2b strongly suggests that the upper-most layer of the ocean is also unstably stratified. As this layer randomly turns over it should occassionally provide sufficiently warm surface spots to induce distinct convective cells in the atmosphere.

A well organized convective plume that carries surface air with a humidity of approximately 0.016 gm/gm to an elevation of 800 meters where the ambient humidity is approximately 0.013 gm/gm may be expected to produce C_n^2 in the outer shell of the cell at this altitude of as much as 10^{-12}, as one may infer from Eq. (2.7). Dilution of the surface moisture as the cell rises through the mixed layer may be expected to reduce this value, but there appears to be ample potential for it to reach detectable levels.

The wind data provided in Table 4.1 indicates that there was little vertical wind shear below 1 km, so that any convective cells reaching the level of 800 meters should be expected to move with the ambient wind speed regardless of how the convective cell is generated at the surface. Thus the observations are completely consistent with convectively generated targets, except for the report that the targets moved at speeds and direction distinctly different from that of the wind. This suggests the possibility of wave-generated targets.

Because of the lack of any atmospheric data above 2 km, we will use a very simplified model of the atmosphere to calculate wave speeds. Our assumptions are these.

(i)   The height of the tropopause is 10 km, and acts like a rigid lid; i.e., $F = 0$ at $z = 10$ km for Eq. (3.1).

(ii) The sea surface acts like a rigid floor; $F = 0$ at $z = 0$.

(iii) The stability parameter, $\beta(z)$ in Eqs. (3.1) and (3.9) is given by:

54

$$\beta = \begin{cases} 0 & 0 < z < 800 \, m \\ 1.2 \times 10^{-4} \, m^{-1}, & 800 \, m < z < 10 \, km \end{cases} \qquad (4.1)$$

(iv) The wind speed and direction are constant. Consequently, we may rewrite Eq. (3.1) in a coordinate system traveling with the wind, so that the computed wave speed will be the speed relative to the wind.

(v) We may use the Boussinesq approximation $[\rho_0 = constant$ in Eq. (3.2)].

Probably none of these assumptions precisely simulates the atmospheric conditions on May 16 or May 17, 1979. However, they should be sufficiently accurate that the resulting wave speeds may be considered representative.

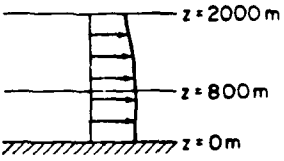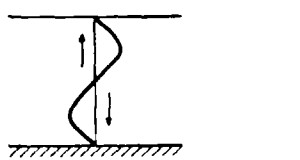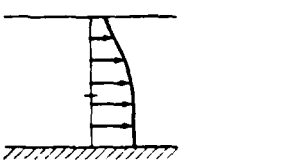With these assumptions, Eq. (3.1) becomes:
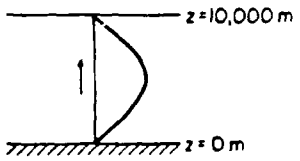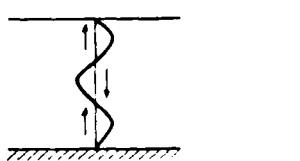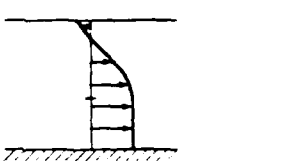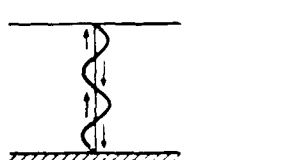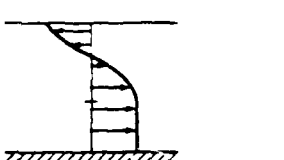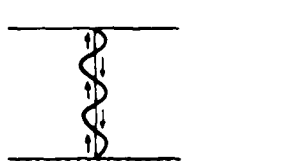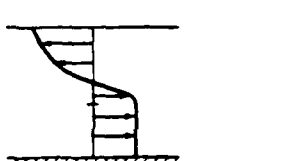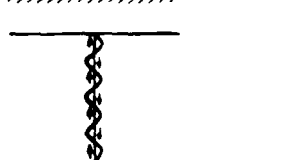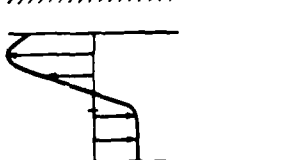
$$\frac{d^2F}{dz^2} + \left[\frac{\beta(z)}{a^2} - k^2 \right] F = 0 , \qquad 0 < z < 10^4 m ,$$

$$(4.2)$$

$$F(0) = 0 = F(10^4) ,$$

with $\beta(z)$ given by Eq. (4.1). Because the observed wavelengths exceed 5 km, we will also take the long wave limit ($k \to 0$). Now Eq. (4.2) may be solved by elementary means. It has an infinite number of solutions, each representing a different vertical mode. Table 4.2 gives the vertical structure and wave speed (relative to the wind) of the first seven vertical modes. We note several points.
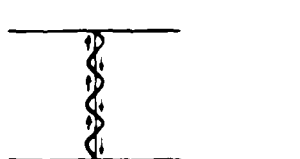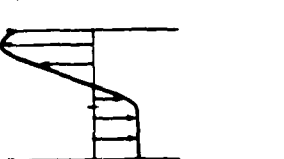
(i) If the rigid lid at the tropopause were replaced with a free surface, the results in Table 4.2 would not change significantly. An additional mode (#0) would enter at the top of the table, with a speed significantly larger than 35 m/sec.

(ii) The first three or four modes would be virtually unaffected if the

55

Table 4.2 - Vertical structure and speeds of the lowest modes, for Eq. (4.2).

Vertical mode number	Distribution of vertical velocity below the tropopause (at a fixed time and horizontal position)	Distribution of Horizontal velocity in the lowest 2 km	Height of lowest maximum in horizontal shear, $\|\partial u/\partial z\|$ (m)	Wave speed relative to the wind (m/sec)
1			5009	34.8
2			2595	17.3
3			1764	11.5
4			1405	8.6
5			1211	6.8
6			1094	5.6
7			1021	4.8

mixed layer below 800 m were removed.

(iii) Modes 4 - 7 all have wave speeds in the range of those observed (roughly 5-10 m/sec relative to the wind).

(iv) For all modes beyond about 5, the long wave approximation holds for any wave significantly longer than about 1 or 2 km. Waves in these modes with horizontal wavelengths on the order of 5 km or more certainly would propagate like long waves.

(v) Modes 5 - 7 (and all higher modes) possess regions of maximal shear within a few hundred meters of the top of the mixed layer. Such regions are capable of generating radar returns, by the scenario given in the following paragraph.

The data in Table 4.1 are consistent with vertical wind shears of the order of 1 to 2 knots over a 100 ft (30 meters) altitude change at the top of the mixed layer, where Figures 4.1a or 4.2a show the potential temperature change to be of the order of 0.1 to 0.3°C. These estimates yield a Richardson number of the order of 0.1 to 1.0. It is thus quite possible for there to be a region where $Ri \approx 0.3$. The addition of the shear associated with wave modes 5 to 7 with even modest amplitudes would then be sufficient to reduce the Ri below 0.25 and induce the type of wave breaking calculated in Appendix A. This region of breaking wave would travel with the wave as long as the time scale of the wave breaking is less than the time required for the wave to pass. Figure A.10 shows that the time scale over which there appears a large increase in temperature variance (which should be the same as that for humidity variance) is approximately $10 \, \ell/\Delta u$. For a shear layer 30 meters (100 feet) thick with a Δu of 1 m/sec (2 knots) this gives a lifetime of approximately 300 sec. This would provide a region 1.5 to 3.0 km long of enhanced C_n^2 travelling with a long wave of speed 5 to 10 m/sec relative to the wind. From Figure A.9 the peak value of $\overline{H'H'}$ should be approximately $0.3 \, \Delta H^2$. The moisture increments in Figures 4.1b and 4.2b just above 800 m would then be sufficient to yield values of $\overline{H'H'} \approx 10^{-6}$ which in turn through Eq. (2.7) would lead to $C_n^2 \sim 10^{-13}$, a borderline value for detectability.

These calculations demonstrate the possibility that long internal gravity waves were present on May 16 and 17, 1979, that they travelled relative to the wind at speeds of 5 to 10 m/sec, that they generated regions of high C_n^2 (i.e., radar targets) near the top of the mixed layer, and that these targets also travelled relative to the wind. As discussed earlier, targets generated by buoyant plumes also were possible on these days. Because the inversion measured on these two days was fairly weak, one would expect typical plume-generated targets (travelling with the wind) to be somewhat stronger than typical wave-generated targets (travelling different from the wind). If the inversion were stronger, this discrepancy in strength of signal would be mitigated.

V. Concluding Remarks

We have provided a catalogue of the dominant types of fluid dynamic features which may be expected to yield trackable radar targets in the atmospheric boundary layer. The simplest distinguishing feature between convectively produced targets and targets produced by wave breaking is the velocity at which the target travels relative to the wind. Except in the presence of strong vertical wind shear, convectively generated targets will travel with the ambient wind, while wave generated targets may or may not travel with the wind. Conditions favorable to convectively generated targets occur quite frequently; those for wave generated targets are likely to occur somewhat less frequently.

We have analyzed in detail one particularly interesting type of wave generated target which travels at velocities significantly different than the ambient wind. A crucial part of this scenario is the Kelvin-Helmholtz wave breaking which occurs in a fluid shear layer where the Richardson number drops below 0.25. This process is studied in detail in Appendix A to show the life history of temperature and humidity fluctuations in such a wave-breaking process. The turbulent transport model used allows the buildup and subsequent decay of these variances to be simulated as a function of the initial conditions of the shear layer. The results of this detailed numerical simulation were used in our analysis of what may have been occurring during the NRL tests.

This initial study has been primarily involved with the general features of clear air radar targets. We recommend a second phase to investigate particular ways in which these signals may become amplified. Interesting questions which should be answerable by further analysis are:

1) Are there conditions for which individual radar targets can be

59

traced back to the atmospheric disturbance which induced it in a
coherent fashion?

2) The complimentary question: Under what conditions can a discrete
atmospheric disturbance be amplified sufficiently to produce a
detectable target?

APPENDIX A

Detailed Examination of Kelvin-Helmholtz Wave Breaking*

A.1 Introduction

Shear instabilities are now widely recognized as a significant mechanism for producing turbulence and mixing in stably-stratified fluids. There are numerous observations of "billow turbulence" in the atmosphere and oceans (see Maxworthy and Browand, 1975) and these events have been associated with Kelvin-Helmholtz instabilities of the wind profile. Laboratory studies by Thorpe (1973) show similar vortex roll-up features and the generation of a turbulent layer of fluid which mixes and spreads the initial shear layer before decaying back to a quiescent flow.

The initial stages of the instability are now well understood. Finite amplitude numerical computations by Patnaik, et al. (1976), Peltier, et al. (1978) have confirmed the linear stability predictions of growth rates and mode structure of the growing waves, and have gone on to calculate the roll-up of the vortex layer. However, these laminar calculations at moderate Reynolds numbers have been unable to identify the secondary instability which results in the breakdown of the vortex into a turbulent layer. Davis and Peltier (1979) made calculations up to a Reynolds number of 500 based on shear layer thickness but failed to produce a secondary instability. In the latter paper, the authors calculated local Rayleigh numbers in the flow, and showed that with a Reynolds number of 500, a region of very high Rayleigh number was produced in the rolled-up vortex. They speculate that this region is in fact convectively unstable, but that the most unstable models will be longitudinal

---

rolls since the flow is strongly sheared. This hypothesis accounts for the fact that the instabilities have not been triggered in the two-dimensional numerical models.

The aim of the present study is to model the breakdown of the rolled-up vortex layer and the subsequent spread and decay of the turbulence using a second-order closure scheme to describe the three-dimensional, small scale turbulence field. Second-order closure models have been used extensively to study horizontally-homogeneous atmospheric boundary layer flows, and in particular are capable of representing the major dynamical processes involved in turbulent convection (see Wyngaard and Coté, 1974; Lewellen, Teske and Donaldson 1976; Yamada and Mellor, 1975). [There are difficulties associated with the turbulent transport of turbulent kinetic energy (see Zeman and Lumley, 1976; Andre, et al., 1976), but this is not a serious problem for the prediction of the mean profiles of the major second-order quantities.] Since the model calculates the growth of turbulent correlations in an unstable environment moderately accurately (because the growth is driven directly by production terms in the equations without recourse to empirical closure), we may reasonably expect the results of the calculation to have some validity. One would not have the same expectation of, say, a mixing-length closure model, since the time scale of the growth of the turbulence is the same as the mean flow time scale, while the mixing-length model implicitly assumes that the turbulence is in local equilibrium. Thus turbulent stresses and heat fluxes would be generated as soon as the density profile became unstable if the mixing-length were related to the stability as in the model of Orlanski and Ross (1973).

As we shall demonstrate, the second-order closure model produces results which are certainly qualitatively correct. Quantitative data on turbulence quantities is not sufficiently detailed to make any meaningful assessment of model accuracy, but there are more general quantities associated with the breakdown which can be used for comparison. There are estimates of the time scale of the turbulence decay and measurements of the final states from the experiments by Thorpe (1973), for example. The final state of the shear layer

is an important quantity in deciding the importance of Kelvin-Helmholtz instability as a mixing process in stratified fluids, since this is a measure of the total amount of mixing produced by the event. Another source of data is high-resolution radar probing of the atmosphere, where vortex roll-up events have been reported by many investigators, as discussed in Chapter III of the main report. However, although it is possible to estimate the intensity of the turbulent fluctuations from the intensity of the radar echo, the measurements of the initial wind and temperature profiles immediately prior to the instability are generally inadequate for a crucial test.

In spite of the lack of detailed information, there is certainly sufficient data to determine whether the turbulence model is reasonably accurate, and hopefully some of the numerical results will prompt more detailed measurements.

A.2 Model Equations and Numerical Solution

The second-order closure scheme employed in this study has been described in detail by Lewellen (1977) and we therefore present only the final equations. We consider incompressible, Boussinesq flow, and write the Reynolds-averaged equations with turbulent correlations denoted by an overbar. For two-dimensional motion in the (x,z)-plane, with z in the upward vertical direction we define a stream-function ψ, such that $u = \partial\psi/\partial z$, $W = -\partial\psi/\partial x$. Then the vorticity $\zeta = \nabla^2\psi$, and the equations of motion are

$$\frac{\partial\zeta}{\partial t} + U\frac{\partial\zeta}{\partial x} + W\frac{\partial\zeta}{\partial z} = -\frac{g}{T}\frac{\partial T}{\partial x} - \frac{\partial^2}{\partial z^2}\overline{uw} - \frac{\partial^2}{\partial x\partial z}(\overline{uu} - \overline{ww}) + \frac{\partial^2}{\partial x^2}\overline{uw}$$

$$(A.1)$$

63

$$\frac{\partial T}{\partial t} + U \frac{\partial T}{\partial x} + W \frac{\partial T}{\partial z} = - \frac{\partial}{\partial x} \overline{u\theta} - \frac{\partial}{\partial z} \overline{w\theta} \tag{A.2}$$

$$\frac{D}{Dt} \overline{u^2} = - 2\overline{uu} \frac{\partial U}{\partial x} - 2\overline{uw} \frac{\partial U}{\partial z} + v_c \frac{\partial}{\partial x} \left(q\Lambda \frac{\partial \overline{u^2}}{\partial x} \right)$$
$$+ v_c \frac{\partial}{\partial z} \left(q\Lambda \frac{\partial \overline{u^2}}{\partial z} \right) - \frac{q}{\Lambda} \left(\overline{uu} - \frac{q^2}{3} \right) - \frac{2bq^3}{3\Lambda} \tag{A.3}$$

$$\frac{D}{Dt} \overline{v^2} = v_c \frac{\partial}{\partial x} \left(q\Lambda \frac{\partial \overline{v^2}}{\partial x} \right) + v_c \frac{\partial}{\partial z} \left(q\Lambda \frac{\partial \overline{v^2}}{\partial z} \right) - \frac{q}{\Lambda} \left(\overline{v^2} - \frac{q^2}{3} \right) - \frac{2bq^3}{3\Lambda} \tag{A.4}$$

$$\frac{D}{Dt} \overline{w^2} = - 2\overline{uw} \frac{\partial W}{\partial x} - 2\overline{ww} \frac{\partial W}{\partial z} + \frac{2g}{T_0} \overline{w\theta} + v_c \frac{\partial}{\partial x} \left(q\Lambda \frac{\partial \overline{w^2}}{\partial x} \right)$$
$$+ v_c \frac{\partial}{\partial z} \left(q\Lambda \frac{\partial \overline{w^2}}{\partial z} \right) - \frac{q}{\Lambda} \left(\overline{w^2} - \frac{q^2}{3} \right) - \frac{2bq^3}{3\Lambda} \tag{A.5}$$

$$\frac{D}{Dt} \overline{uw} = - \overline{uu} \frac{\partial W}{\partial x} - \overline{ww} \frac{\partial U}{\partial z} + \frac{g}{T_0} \overline{u\theta} + v_c \frac{\partial}{\partial x} \left(q\Lambda \frac{\partial \overline{uw}}{\partial x} \right)$$
$$+ v_c \frac{\partial}{\partial z} \left(q\Lambda \frac{\partial \overline{uw}}{\partial z} \right) - \frac{q}{\Lambda} \overline{uw} \tag{A.6}$$

64

$$\frac{D}{Dt}\overline{u\vartheta} = -\overline{uu}\frac{\partial T}{\partial x} - \overline{uw}\frac{\partial T}{\partial z} - \overline{u\vartheta}\frac{\partial U}{\partial x} - \overline{w\vartheta}\frac{\partial U}{\partial z} + v_c\frac{\partial}{\partial x}\left(q\Lambda\frac{\partial\overline{u\vartheta}}{\partial x}\right)$$

$$+ v_c\frac{\partial}{\partial z}\left(q\Lambda\frac{\partial\overline{u\vartheta}}{\partial z}\right) - \frac{Aq}{\Lambda}\overline{u\vartheta} \tag{A.7}$$

$$\frac{D}{Dt}\overline{w\vartheta} = -\overline{ww}\frac{\partial T}{\partial x} - \overline{ww}\frac{\partial T}{\partial z} - \overline{u\vartheta}\frac{\partial W}{\partial x} - \overline{w\vartheta}\frac{\partial W}{\partial z} + v_c\frac{\partial}{\partial x}\left(q\Lambda\frac{\partial\overline{w\vartheta}}{\partial x}\right)$$

$$+ v_c\frac{\partial}{\partial z}\left(q\Lambda\frac{\partial\overline{w\vartheta}}{\partial z}\right) - \frac{Aq}{\Lambda}\overline{w\vartheta} + \frac{g}{T_0}\overline{\vartheta^2} \tag{A.8}$$

$$\frac{D}{Dt}\overline{\vartheta^2} = -2\overline{u\vartheta}\frac{\partial T}{\partial x} - 2\overline{w\vartheta}\frac{\partial T}{\partial z} + v_c\frac{\partial}{\partial x}\left(q\Lambda\frac{\partial\overline{\vartheta^2}}{\partial x}\right)$$

$$+ v_c\frac{\partial}{\partial z}\left(q\Lambda\frac{\partial\overline{\vartheta^2}}{\partial z}\right) - \frac{2bsq}{\Lambda}\overline{\vartheta^2} \tag{A.9}$$

$$\frac{D}{Dt}\Lambda = 0.35\frac{\Lambda}{q^2}\left(\overline{uu}\frac{\partial U}{\partial x} + \overline{uw}\frac{\partial U}{\partial z} + \overline{uw}\frac{\partial W}{\partial x} + \overline{ww}\frac{\partial W}{\partial z}\right)$$

$$+ 0.6bq + v_c\frac{\partial}{\partial x}\left(q\Lambda\frac{\partial\Lambda}{\partial x}\right) + v_c\frac{\partial}{\partial z}\left(q\Lambda\frac{\partial\Lambda}{\partial z}\right)$$

$$- \frac{0.375}{q}\left[\left(\frac{\partial q\Lambda}{\partial x}\right)^2 + \left(\frac{\partial q\Lambda}{\partial z}\right)^2\right] + \frac{0.8\Lambda}{q^2}\frac{g}{T_0}\overline{w\upsilon} \tag{A.10}$$

In the above, (U,W) is the mean velocity, T is the mean temperature, (u,v,w) is the turbulent velocity fluctuation, υ is the temperature fluctuation, and $q = [\overline{u^2} + \overline{v^2} + \overline{w^2}]^{1/2}$. Λ is a length scale, and appears in the modelled terms in the Reynolds-averaged turbulent correlation equation. The values of the empirical constants are as follows: $b = 1/8$, $A = 0.75$, $V_c = 0.3$, and $s = 1.8$. These values were previously chosen to match model results with a set of experiments with simple geometries as described by Lewellen (1977).

For the Kelvin-Helmholtz instability calculation, we begin with a profile of temperature and velocity, viz,

$$T = T_0 + \Delta T \tanh\frac{z}{\delta} \tag{A.11}$$

$$U = \Delta U \tanh\frac{z}{\delta} \tag{A.12}$$

Note that velocity and temperature both have the same profile shape. The initial conditions define a Richardson number $Ri = (g/T_0)(\Delta T\delta/\Delta U^2)$, which will be the basic dimensionless number in our experiments. The problem also contains a Reynolds number, but since we have omitted explicit laminar diffusive terms from the equations of motion, we are effectively studying the high Reynolds number limit.

In order to begin the integration, we have to specify initial values for the turbulence energy, q^2, and the length scale Λ; in the calculations reported here, all other turbulence quantities were initially set to zero. A perturbation vorticity was also added so that the instability would amplify this disturbance and produce the vortex roll-up. The specification of these initial conditions will be discussed in the next section.

Periodic boundary conditions were employed in the x-direction, and the length of the domain was chosen somewhat larger than the wavelength of the fastest growing linear mode. This choice is suggested by the nonlinear calculations of Patnaik, et al. (1976), which show that the longer waves grow to larger amplitude, and may therefore dominate the finite amplitude development of the wave. For most of our integrations, a domain length of 15δ was used, although some runs were made with different lengths to investigate the sensitivity.

The boundaries in the z-direction were placed sufficiently far from the shear layer for them to have negligible effect on the flow development. A zero normal gradient condition was specified on all flow quantities on the upper and lower boundaries.

The equations of motion are discretized on a finite-difference grid which is uniformly spaced in the horizontal but has finer vertical resolution in the vicinity of the shear layer. The equations are solved using centered spatial derivatives, and an ADI scheme for the temporal derivative. The advection operator conserves first and second moments apart from time-dependence errors arising from the use of explicit advective velocity components in the ADI

67

scheme. The time-stepping is made more stable by the introduction of a coupling between the mean variables and the turbulent fluxes by the artifice of an additional implicit eddy diffusive flux which is explicitly subtracted when the correct turbulent flux is added (Lewellen and Sheng, 1980). Provided the time-step is sufficiently small, the errors introduced by this procedure will be negligible.

Finally, the Poisson equation for the streamfunction is solved directly using the decomposition method of Swarztrauber and Sweet (1975).

A.3 Results

We consider an initial state, as described in Section A.2, given by

$$T = T_0 + \Delta T \tanh \frac{z}{\delta} \tag{A.13a}$$

$$U = \Delta U \tanh \frac{z}{\delta} \tag{A.13b}$$

which defines a Richardson number $Ri = (g\delta\Delta T/T_0\Delta u^2)$. This is in fact the minimum gradient Richardson number, defined by $Ri_G = [(g/T_0)(\partial T/\partial z)]/(\partial U/\partial z)^2$, which occurs at $z = 0$. Linear inviscid theory (Miles, 1961) shows that the flow is stable to small perturbations provided $Ri > 0.25$.

We first present detailed results from a calculation with $Ri = 0.1$. In this example, we applied a sinusoidal (in x) variation to the vorticity in order to initiate the instability. The perturbation vorticity amplitude of $0.1\Delta u/\delta$ is quite large; this is because we are mainly interested in the finite-amplitude breaking of the billow and the subsequent turbulent development, so that we do not wish to spend time computing the initial growth from a very small perturbation. Checks were made to ensure that the initial perturbation was sufficiently small that it did not influence the

68

finite-amplitude development.

The turbulence energy q^2 was initially set at $10^{-3}(\Delta U)^2$ throughout the domain, with the turbulence length scale, Λ, set equal to 0.4δ. The turbulence energy is initially small enough to be effectively zero, but the initial length scale does have some effect on the results. Variations in these initial values will be discussed in more detail in Section 6 below.

The integration was performed using a domain of length 15δ and a height of 12δ centered on the mid-point of the shear layer. The computational mesh consisted of 41×61 points, with 41 points spaced uniformly in the horizontal, and a non-uniform vertical mesh giving a grid spacing of 0.1δ in the central region and expanding out to roughly 0.2δ.

Figure A.1 shows a sequence of contour plots of the dimensionless temperature field, $(T - T_0)/\Delta T$, at dimensionless time τ = 1.5, 2.8, 4.3, 5.8, 7.3, and 11.8, where $\tau = t(g\Delta T/T_0\Delta u)$. Corresponding plots of the small-scale turbulent energy $q^2/(\Delta U)^2$ are presented in Figure A.2. The billow develops initially as an effectively laminar flow with a growing vortex core in the center, and thin braids forming between the cores. The initial turbulent perturbation in q^2 is amplified slowly in the braids where the shear is highest, and the local Richardson number is lowest. At τ = 2.8 the instability has vertically reached its maximum amplitude, with temperature contours quite convoluted in the vortex core, and the braids have become very thin. At this stage the temperature field is statically unstable in the core, and the q^2 contours show growth of turbulence associated with the buoyant instability, although the turbulence is still relatively small everywhere with the buoyantly produced turbulence in the core comparable with the turbulence levels in the braids.

At the next time, τ = 4.3, most of the temperature structure in the core has been mixed by the turbulence which has reached a relatively high level around the outer part of the core; the maximum value of q^2 is $0.18(\Delta U)^2$. The core has already begun to spread horizontally, although the braids are still
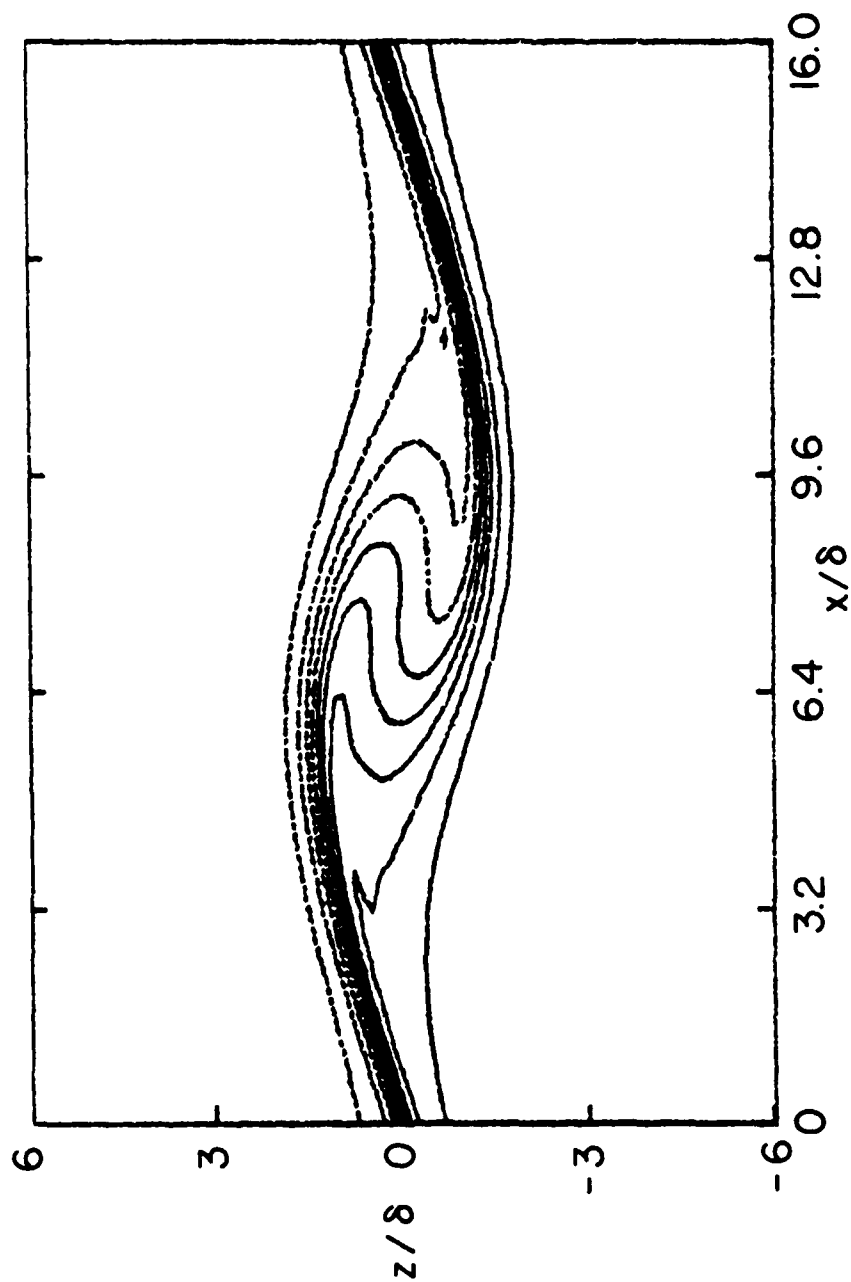
69

Figure A.1 - Isopleths of dimensionless temperature $(T - T_0)/\Delta T$ for the case with Ri = 0.1. The contour interval is 0.2, and positive contours (i.e., lighter fluid) are denoted by a dashed line. (a) $\tau = 1.5$.
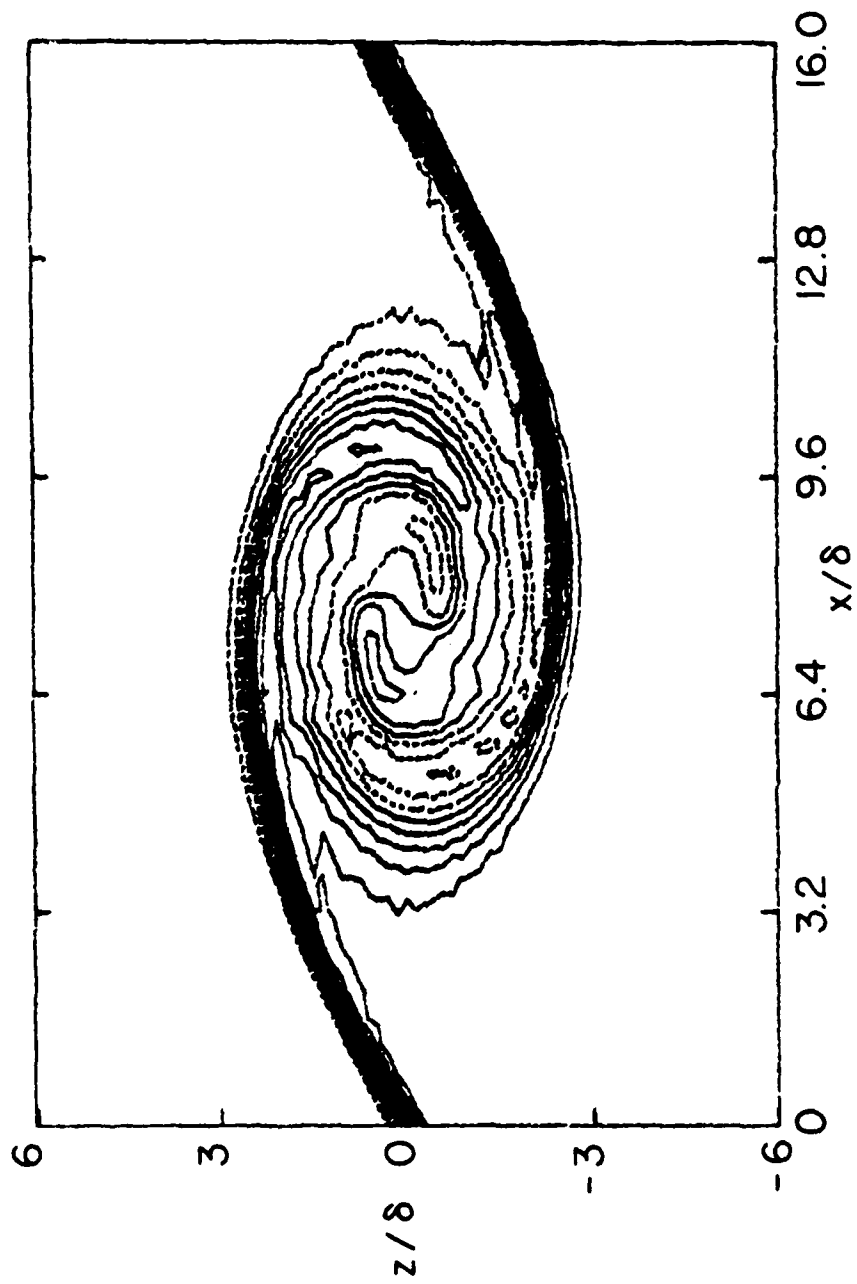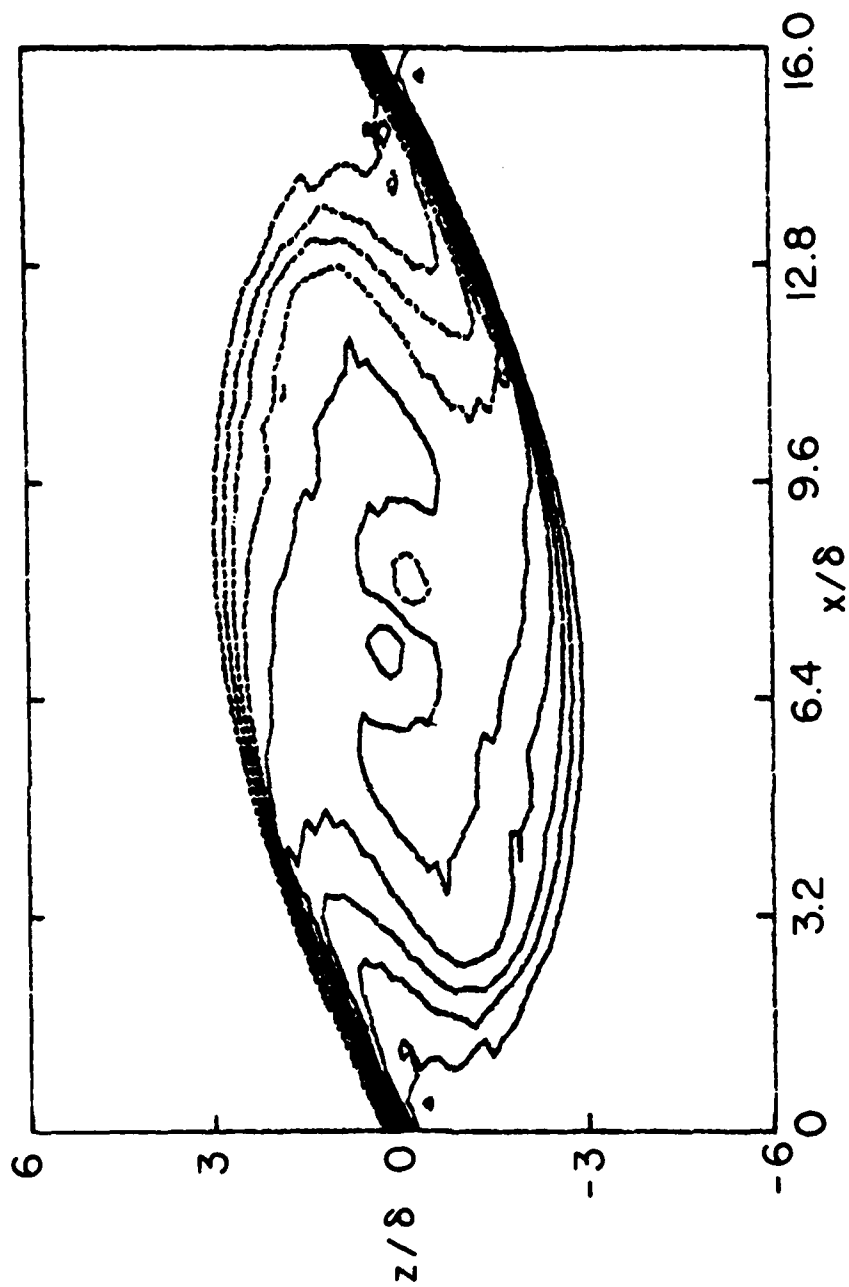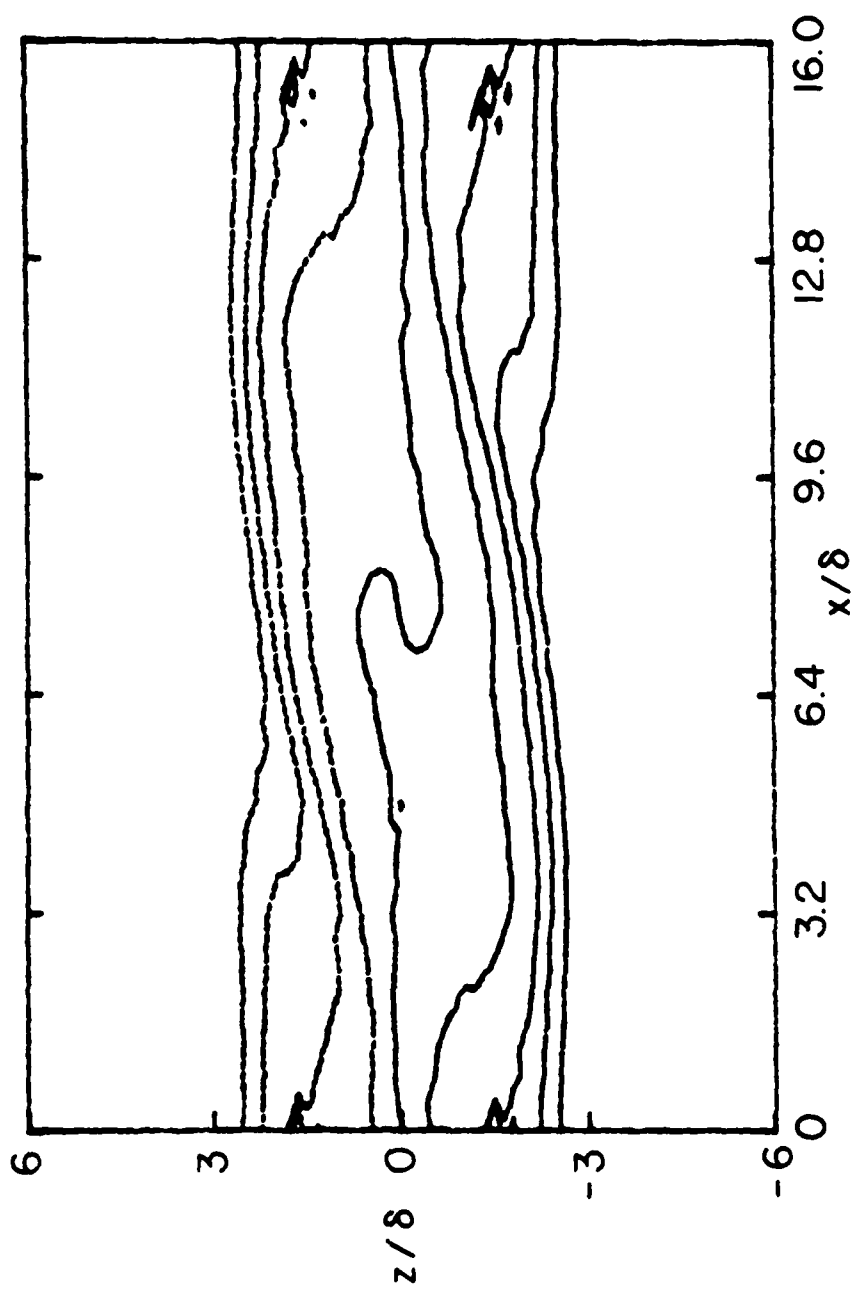
Figure A.1(b) – $\tau = 2.3$
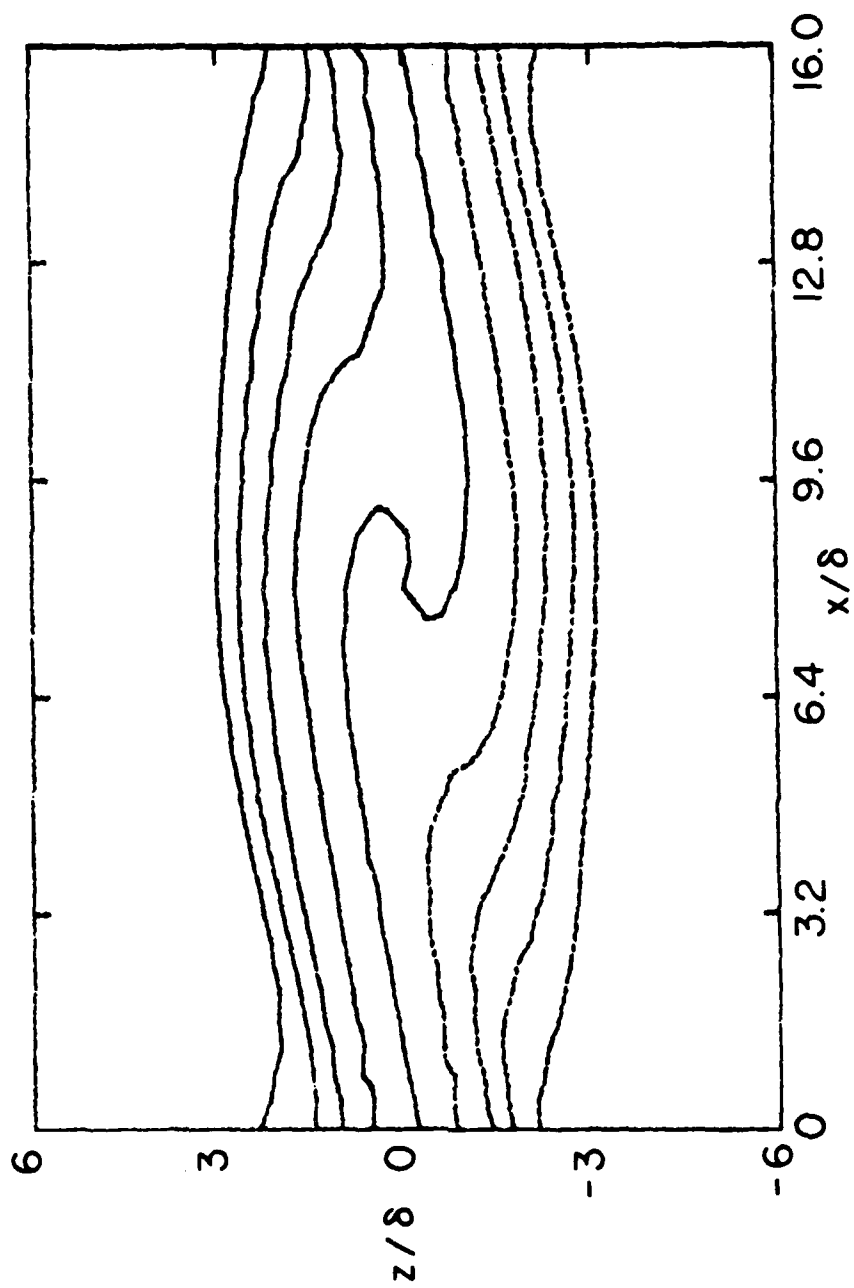
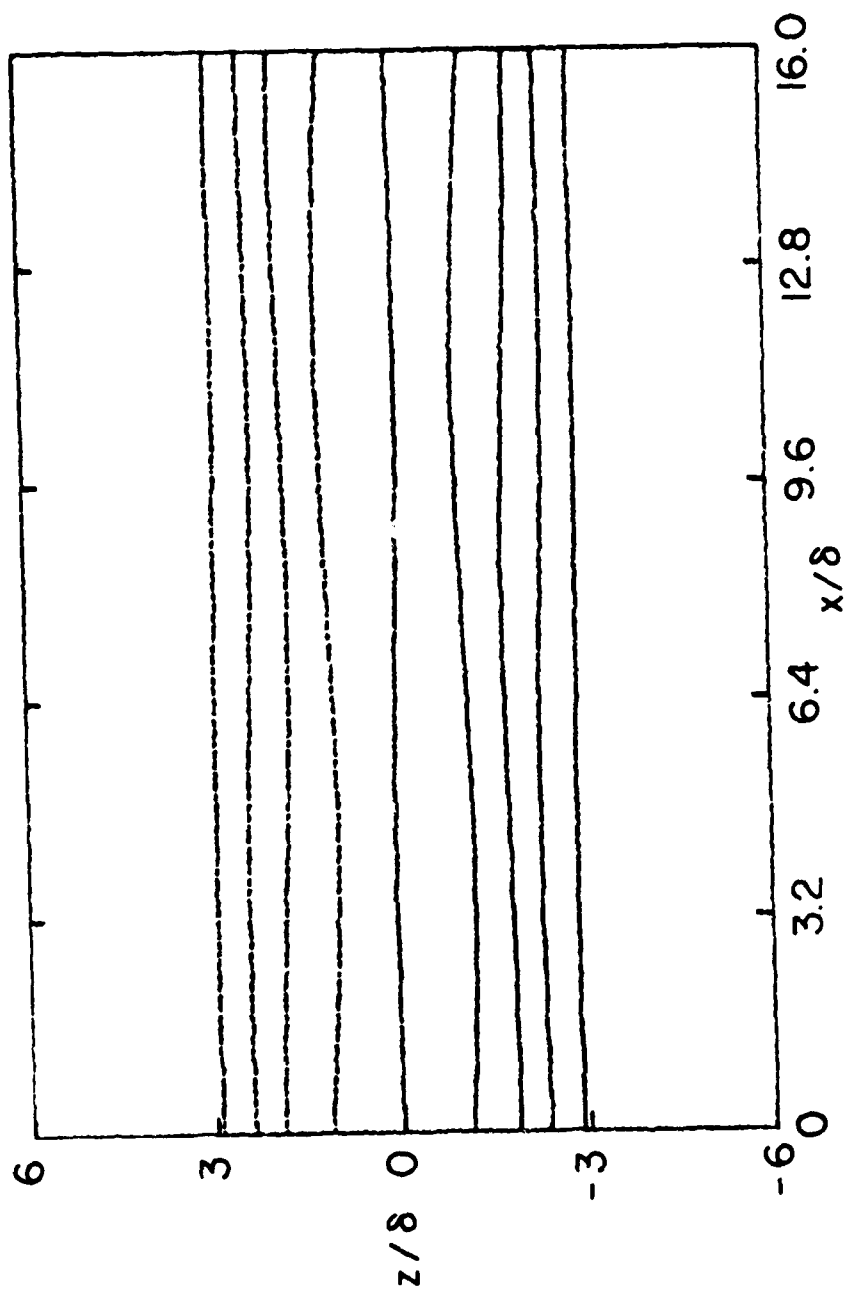Figure A.1(c) – τ = 4.3

Figure A.1(d) - τ = 5.8

73

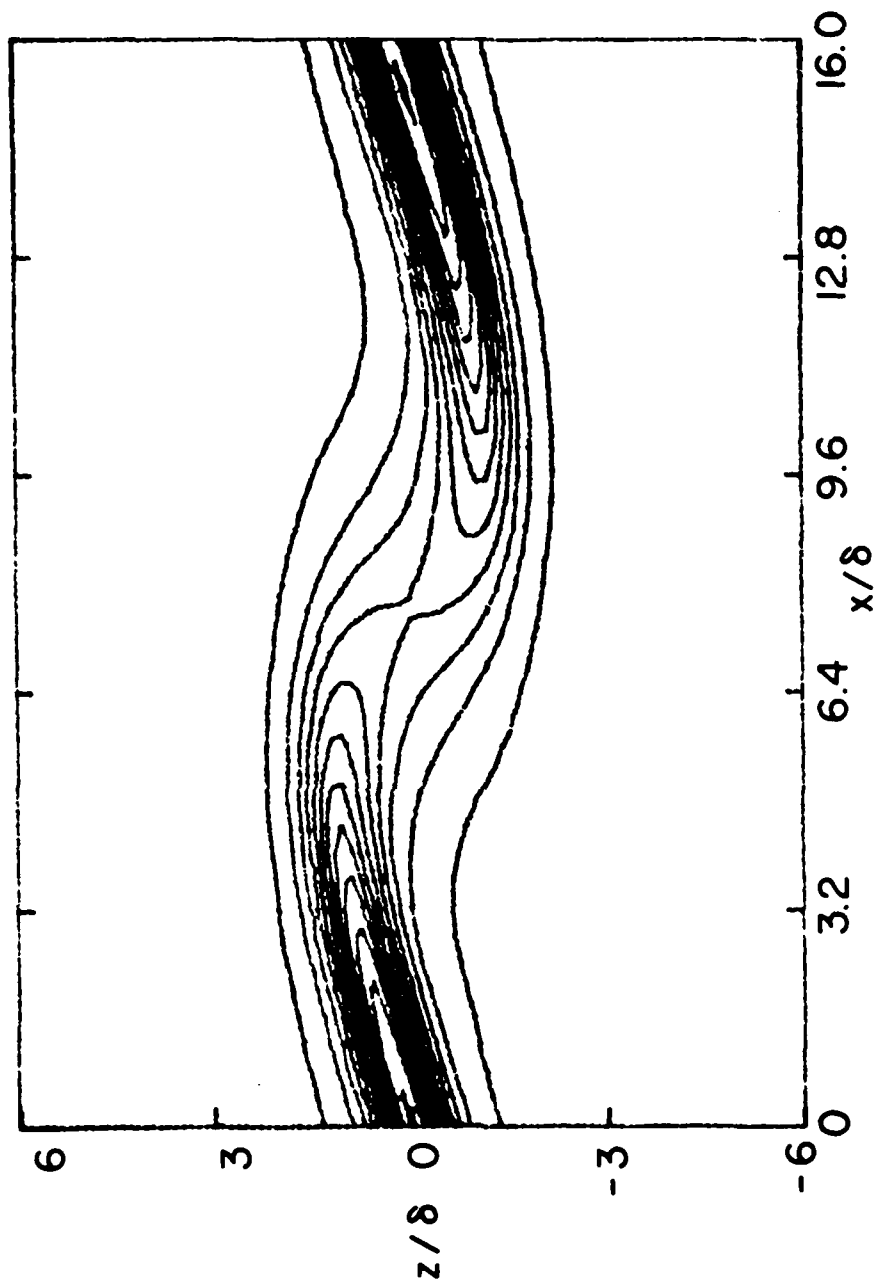Figure A.1(e) – $\tau = 7.3$

74

Figure A.1(f) - $\tau = 11.8$

75

Figure A.2 - Isopleths of dimensionless turbulence kinetic energy, $q^2/\Delta U^2$ at the same times as Figure A.1, i.e., (a) $\tau = 1.5$, contour interval is 0.001.
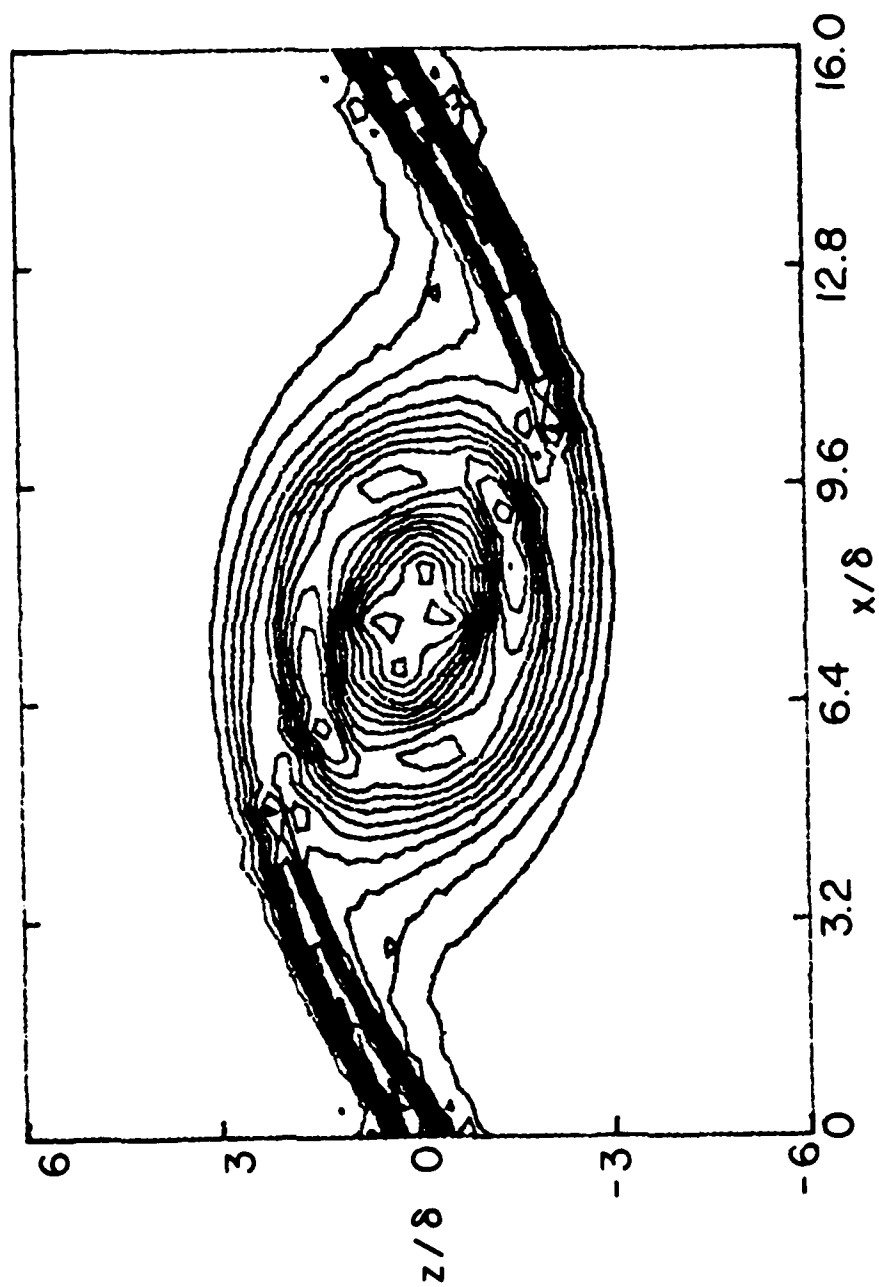
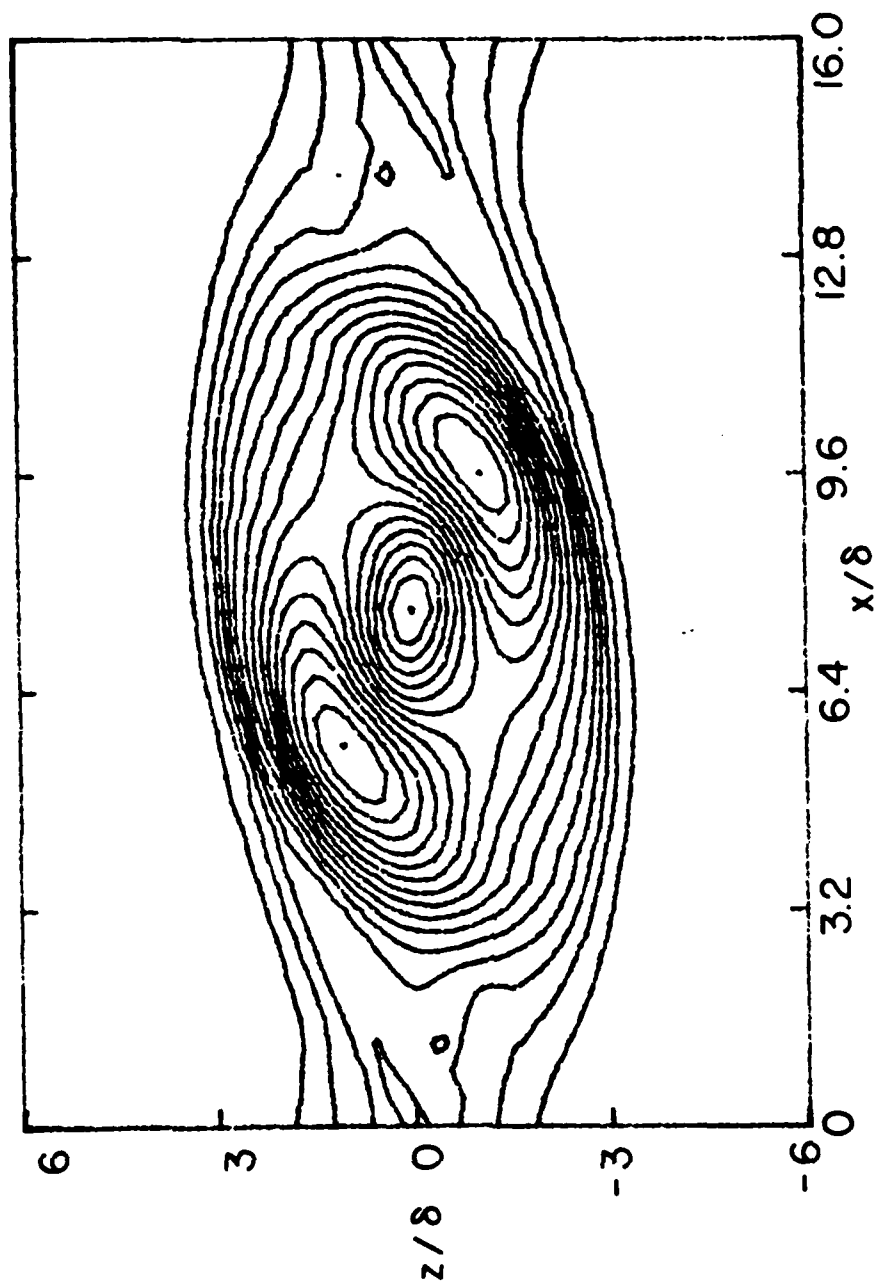Figure A.2(b) – τ = 2.8, contour interval is 0.005.

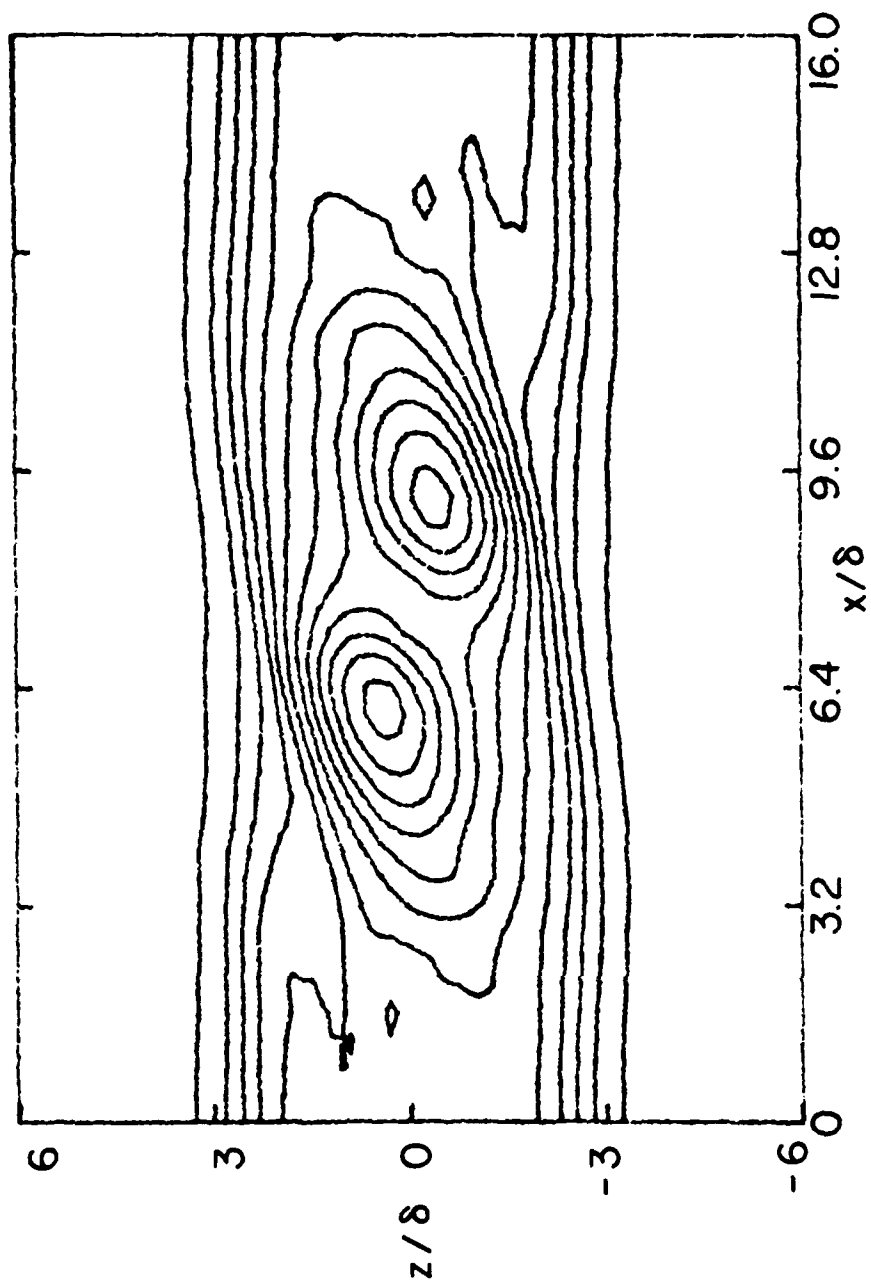Figure A.2(c) - $\tau = 4.3$, contour interval is 0.01.

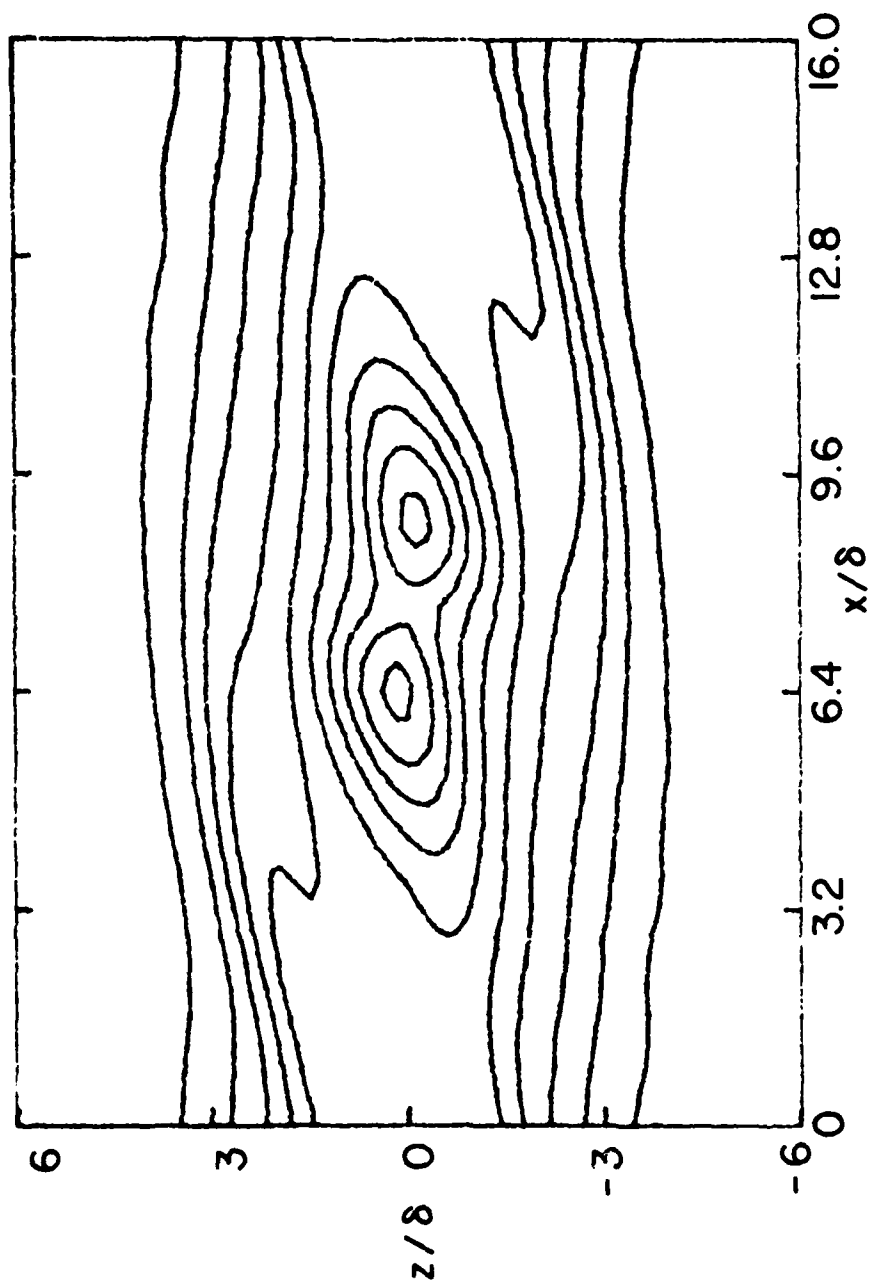Figure A.2(d) - $\tau = 5.8$, contour interval is 0.01

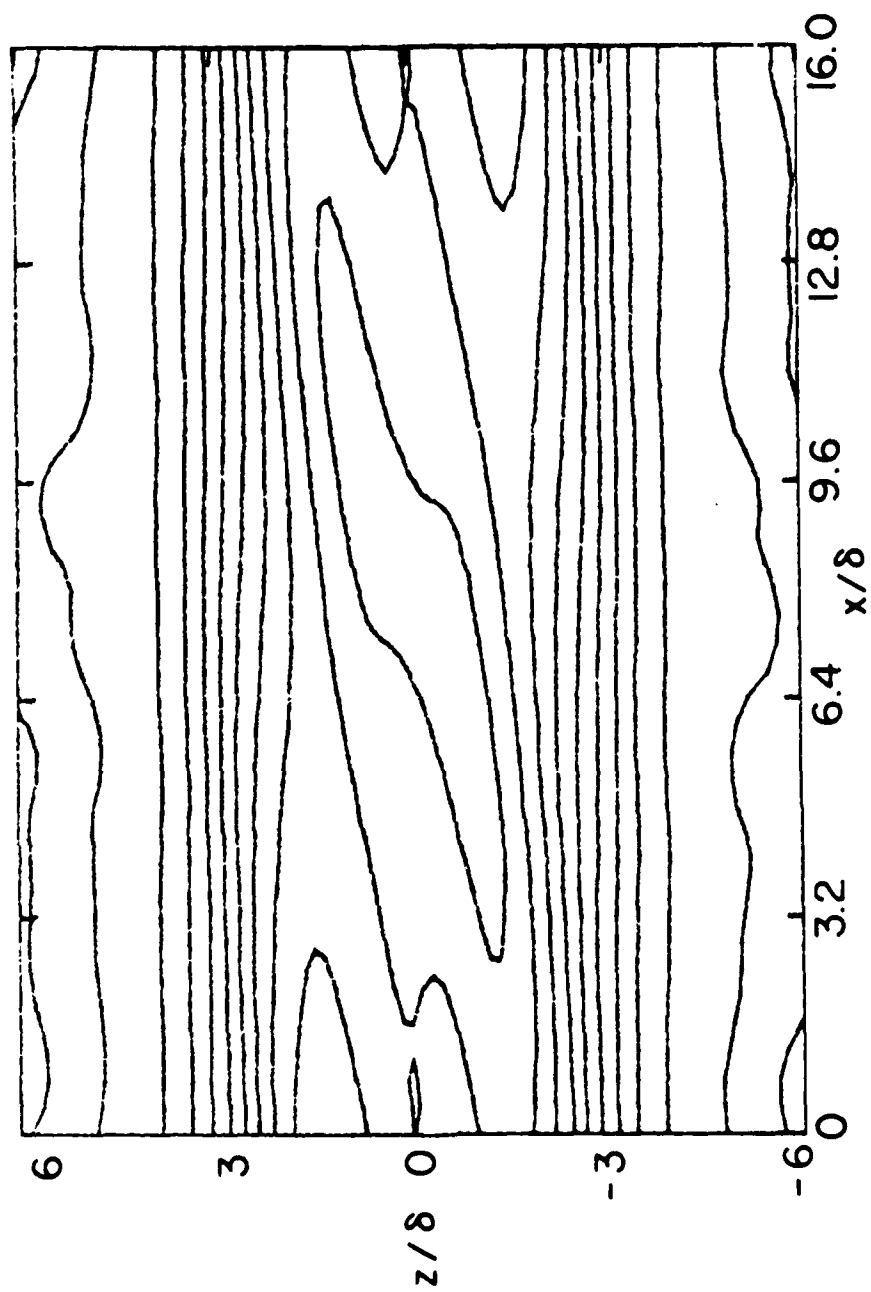Figure A.2(e) - $\tau = 7.3$, contour interval is 0.0007.

Figure A.2(f) - τ = 11.8, contour interval is 0.002.

81

quite distinct. At $\tau = 5.8$, the braids have been mixed, and the turbulence has spread throughout the layer in the horizontal. There is evidence of smaller scale disturbances in the temperature field, and a movie of the time evolution shows them to be travelling wave-like disturbances moving along the top and bottom of the layer, and also weakly rolling up in a manner similar to the original instability. However, they are also being mixed by the high background turbulence so that they do not persist long. There is also some remnant of the original large scale vortex which continues to slowly turn the isotherms. We can still identify the regions of production of the turbulent energy, since the level of q^2 in the center is about twice the level at the edges of the domain.

The trend toward flattening the isotherms, and spreading the turbulence horizontally continues until at the latest time, $\tau = 11.8$, there is virtually no further mean motion, and the turbulence is almost homogeneous in the horizontal. The turbulence level has dropped to $0.022(\Delta U)^2$ at this stage, i.e., almost a factor of 10 below its maximum amplitude which occurred around $\tau = 4.3$.

The evolution described above is qualitatively similar to the turbulent breakdown of Kelvin-Helmholtz billows generated in the laboratory as described by Thorpe (1973). In the tank experiments, the small-scale turbulence is generated in the vortex cores, and spreads horizontally to amalgamate the billows at dimensionless time of roughly $\tau = \tau_0 + 2$, where τ_0 is the time at which the fine-scale turbulence first appears. Since $\tau_0 \approx 3$ in the numerical integration, the obsesrvation that the turbulence merges horizontally at some time between $\tau = 4.3$ and $\tau = 5.8$ is quite consistent with the experimental data. Furthermore, the thickness of the region of turbulent fluid increases slowly after merging in the horizontal and seems to reach an equilibrium level near the end of the integration. This is again consistent with the experimental observations of Thorpe (1973), which show the layer increasing in thickness up to $\tau = \tau_0 + 7$, i.e., $\tau = 10$ in our case. Also the non-dimensional height, $R_L = g(\Delta T.h)/(2\Delta U^2)$ where h is the thickness of the turbulent layer, reaches a value of about 0.4 in accordance with the

82

experiments.

Some insight into the dynamics is obtainable from examination of the energy budgets. In Figure A.3, we plot the roll energy, EK, and the small-scale turbulence energy, EQ, defined by

$$EK = \frac{1}{\Delta U^2 \delta^2} \iint \{[u - \bar{u}(z)]^2 + w^2\} \, dx \, dz \qquad (A.14)$$

$$EQ = \frac{1}{\Delta U^2 \delta^2} \iint q^2 \, dx \, dz \qquad (A.15)$$

where

$$\bar{u}(z) = \frac{1}{L} \int_0^L U \, dx \qquad (A.16)$$

We can see the rapid initial build-up of roll energy as the growing billow extracts kinetic energy from the mean shear, whilst the turbulence energy EQ remains virtually constant at its initial perturbation level. At roughly $\tau = 2.5$, EQ begins to increase as the billow starts to break, and EK levels off at its maximum value. The kinetic energy is effectively transferred via potential energy to the small-scale turbulence which reaches a peak at $\tau = 5$. The large scale motion loses its energy very rapidly after breaking, while the small-scale turbulence persists throughout the integration, and exhibits a relatively slow rate of decay. Thorpe (1973) shows that the turbulence persists until roughly $\tau = \tau_0 + 12 = 15$, at which
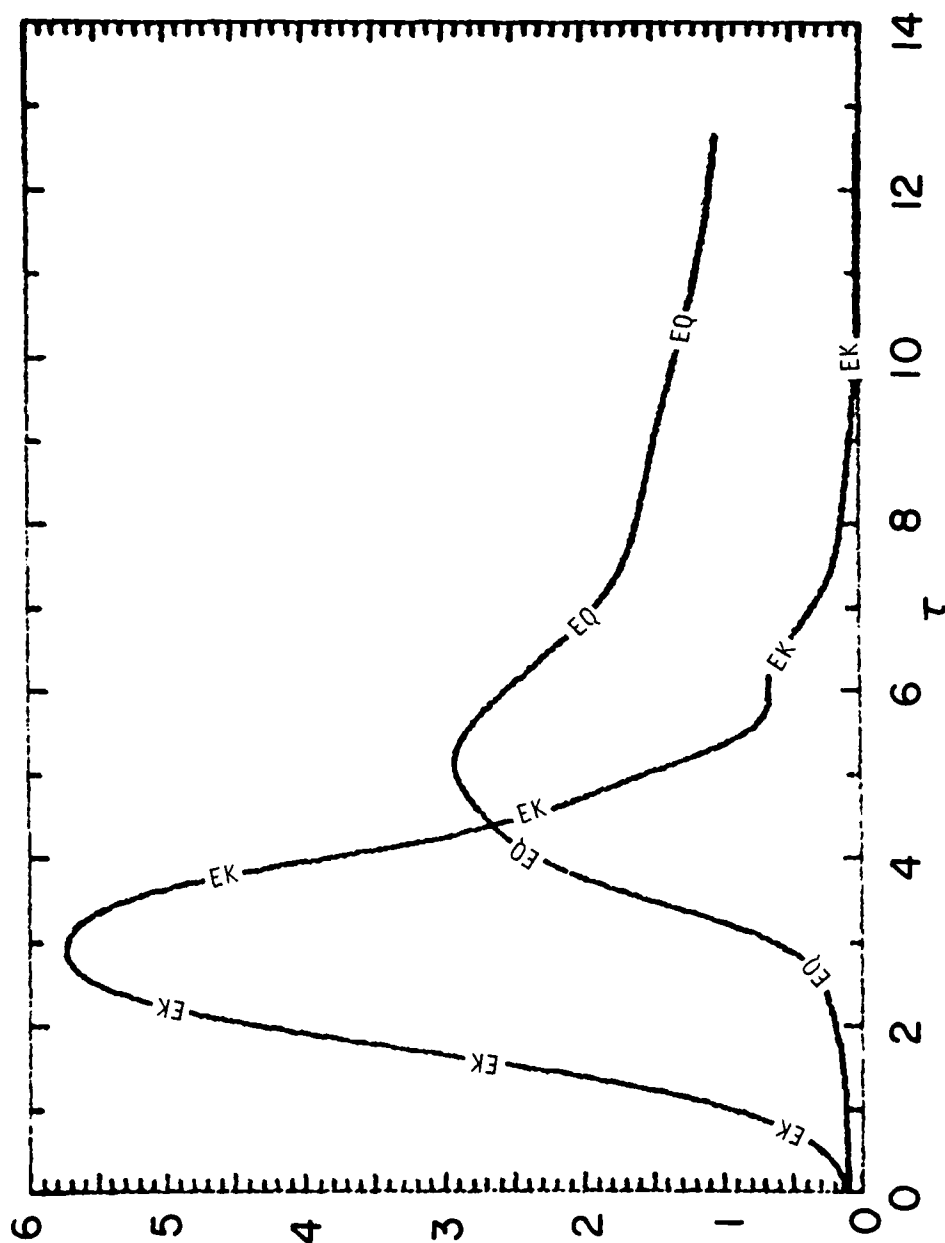
83

Figure A.3 - Evolution of total kinetic energies, EK and EQ, for the large eddy and the small-scale turbulence in the Ri = 0.1 case.

point there appears to be a collapse of the turbulent eddies into striated structures. The present second-order closure model of the small-scale eddies provides a poor representation of this final stage of the decay of turbulence in a stably-stratified medium, and we have therefore not attempted to integrate beyond $\tau = 13$.

Profiles of the initial and final ($\tau = 11.8$) local gradient Richardson number,

$$Ri_G = \frac{g}{T_0} \frac{\partial T/\partial z}{(\partial U/\partial z)^2} \tag{A.17}$$

are shown in Figure A.4. The final value of Ri_G in the layer is not quite constant, but lies between 0.3 and 0.35. This is again consistent with Thorpe's estimate of the final Richardson number. This value is significantly larger than the critical value of 0.25, so that the mixing-process apparently extracts sufficient energy from the initially unstable flow to mix the mean profiles further than the point at which no more energy can be extracted. The agreement between the calculation and the experiment on this number is some confirmation that the model describes the energy transfers in the initial stages reasonably accurately. The basic energy source is kinetic energy produced by the billow acting on the mean shear, and it seems likely that the final amount of mixing will be determined by the amount of energy that the billow can extract before it breaks. If the turbulence model predicted the wrong time-scales for the breaking process, we would be unlikely to obtain the correct final state.

The evolution from an initial Richardson number of 0.2 is illustrated in figures A.5 and A.6. A mesh of 41×61 grid points was used, as in the previous case, with a domain size of 15δ in the horizontal again, but only 6δ in the vertical. Contours of temperature and small-scale turbulent kinetic energy at $\tau = 3.0$, 6.0, 9.0, 14.6, and 20.6. Clearly, the billow is much more restricted in the vertical due to the fact that there is relatively less
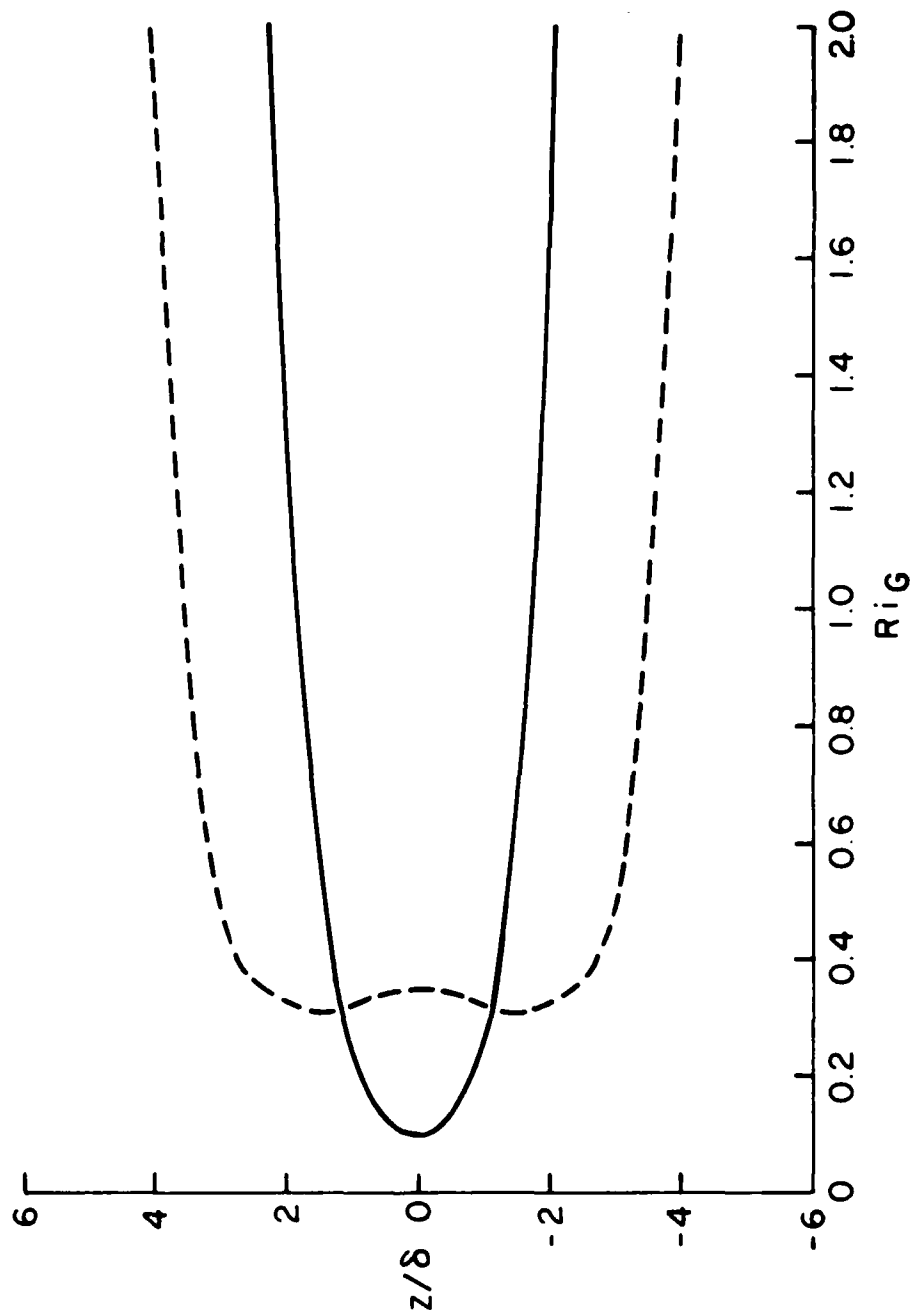
85

Figure A.4 - Profiles of gradient Richardson number, Ri_G, for the $Ri = 0.1$ case. Solid line is the initial profile at $\tau = 0$, dashed line is the profile at $\tau = 11.8$.
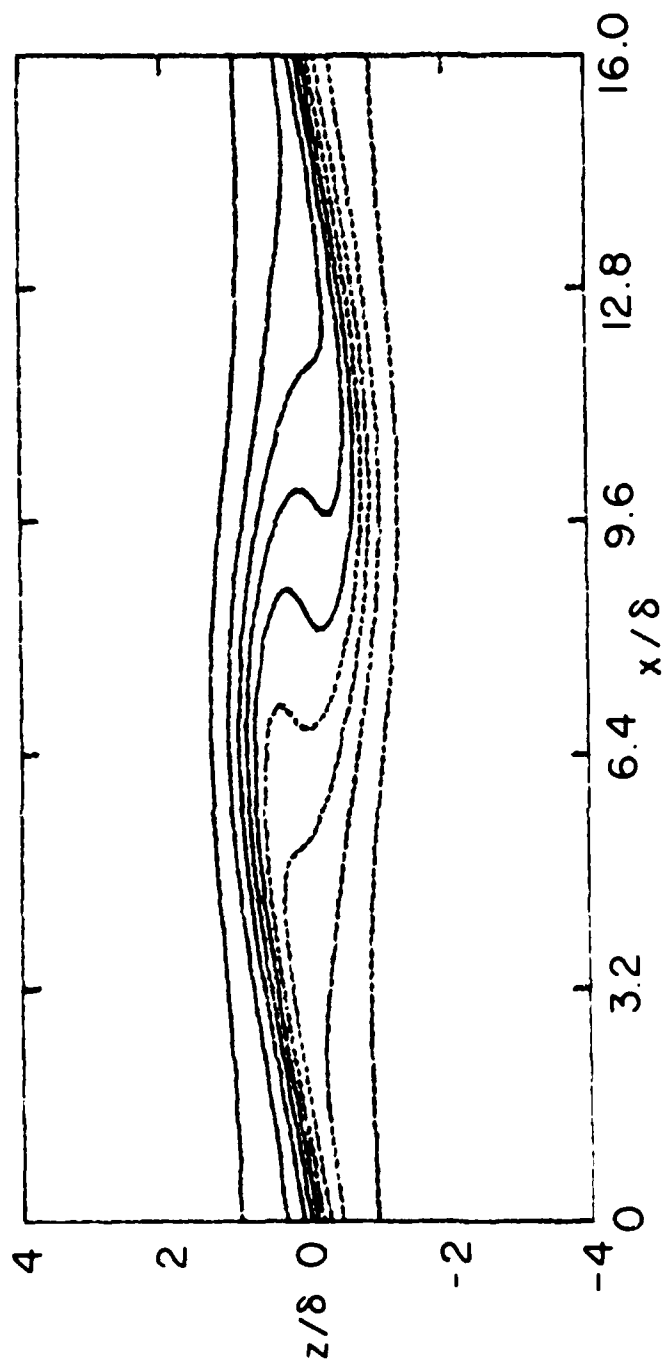
Figure A.5 - Isopleths of dimensionless temperature $(T - T_0)/\Delta T$ for the case with $Ri = 0.2$ at (a) $\tau = 3$. Contour interval is 0.2
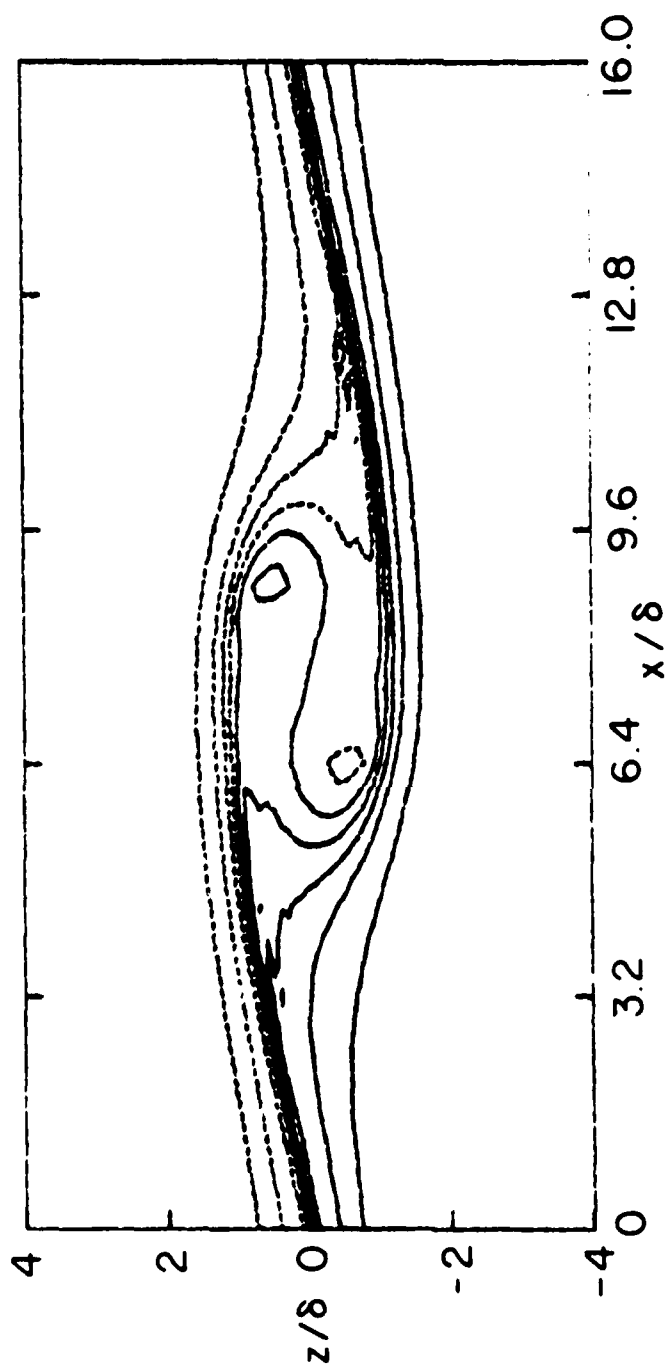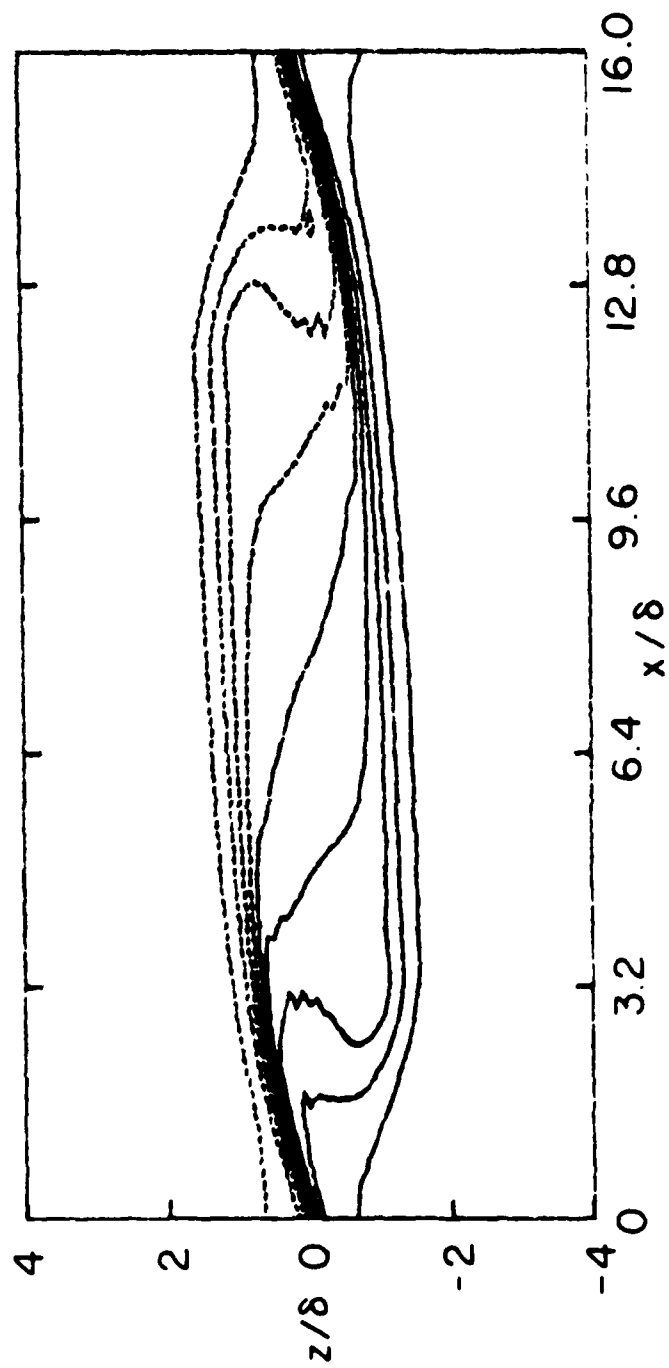
87

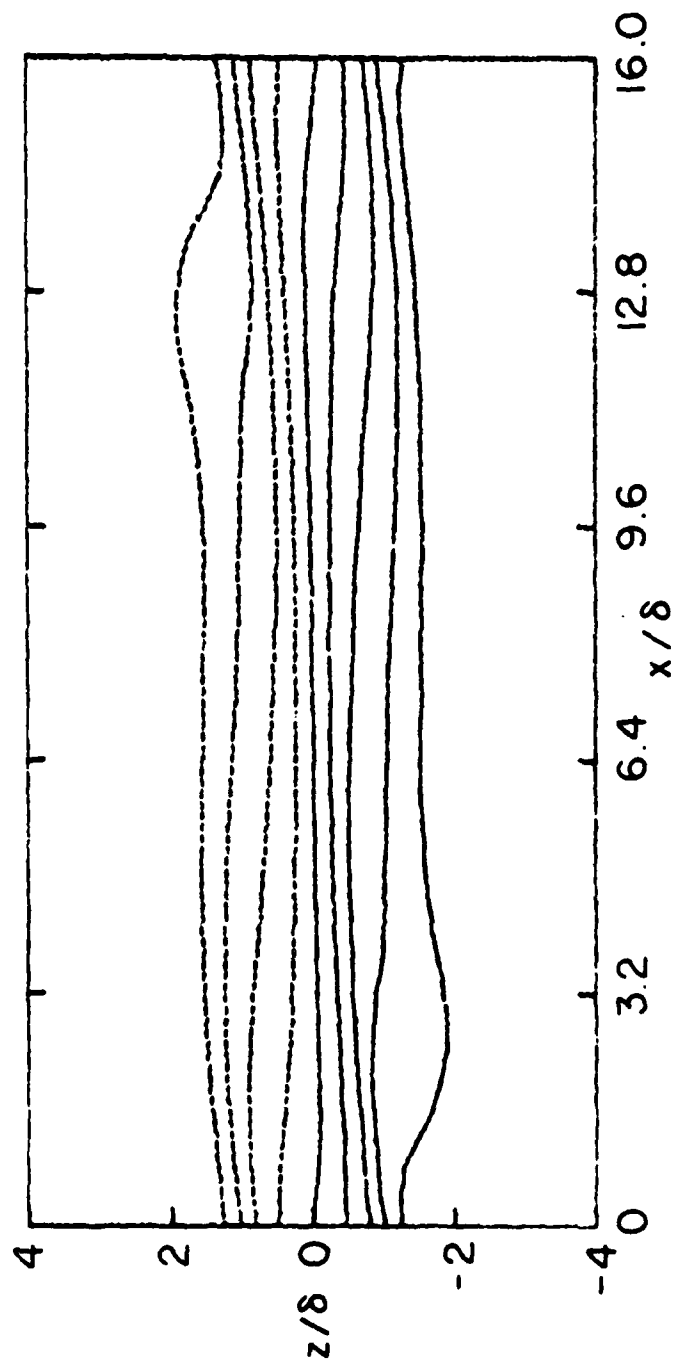Figure A.5(b) - $\tau = 6$.

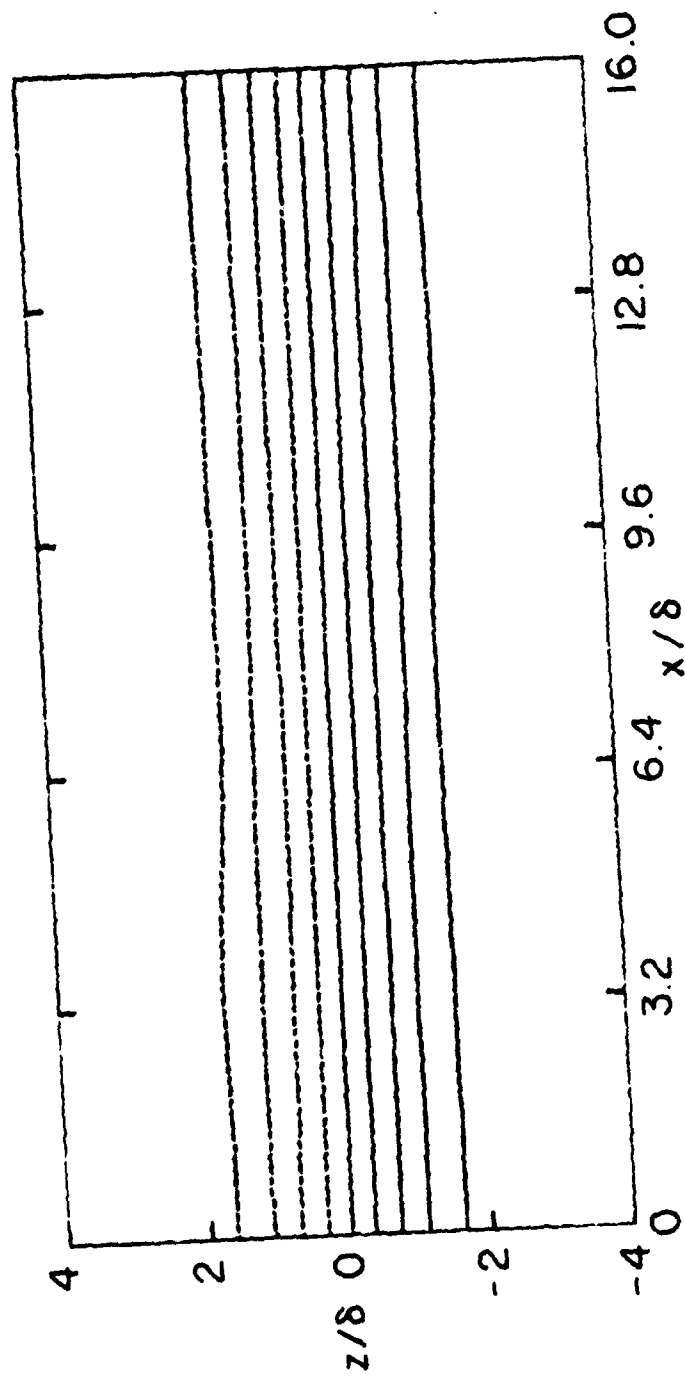Figure A.5(c) - τ = 9.

Figure A.5(d) - τ = 14.6

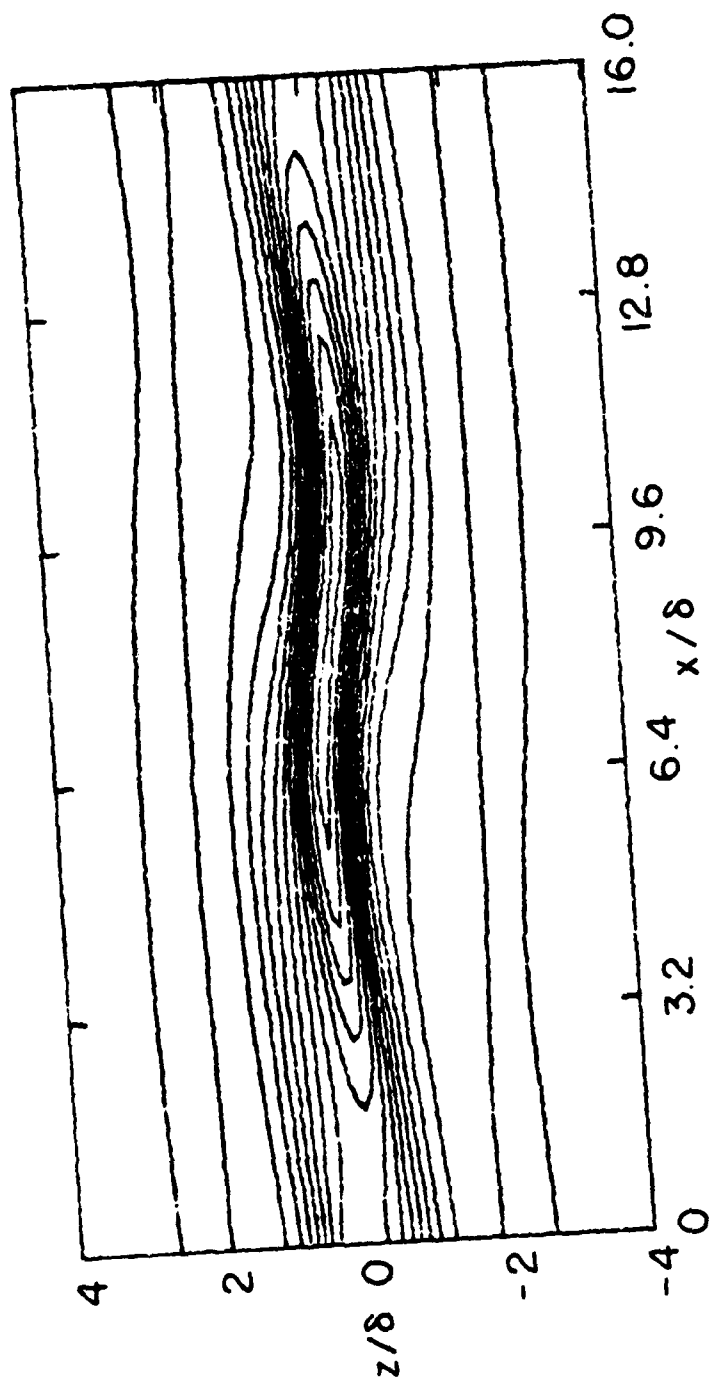Figure A.5(e) - τ = 20.6.

91

Figure A.6 - Isopleths of dimensionless turbulence kinetic energy $q^2/\Delta U^2$ for $Ri = 0.2$ at (a) $\tau = 3$, contour interval is 0.0003.
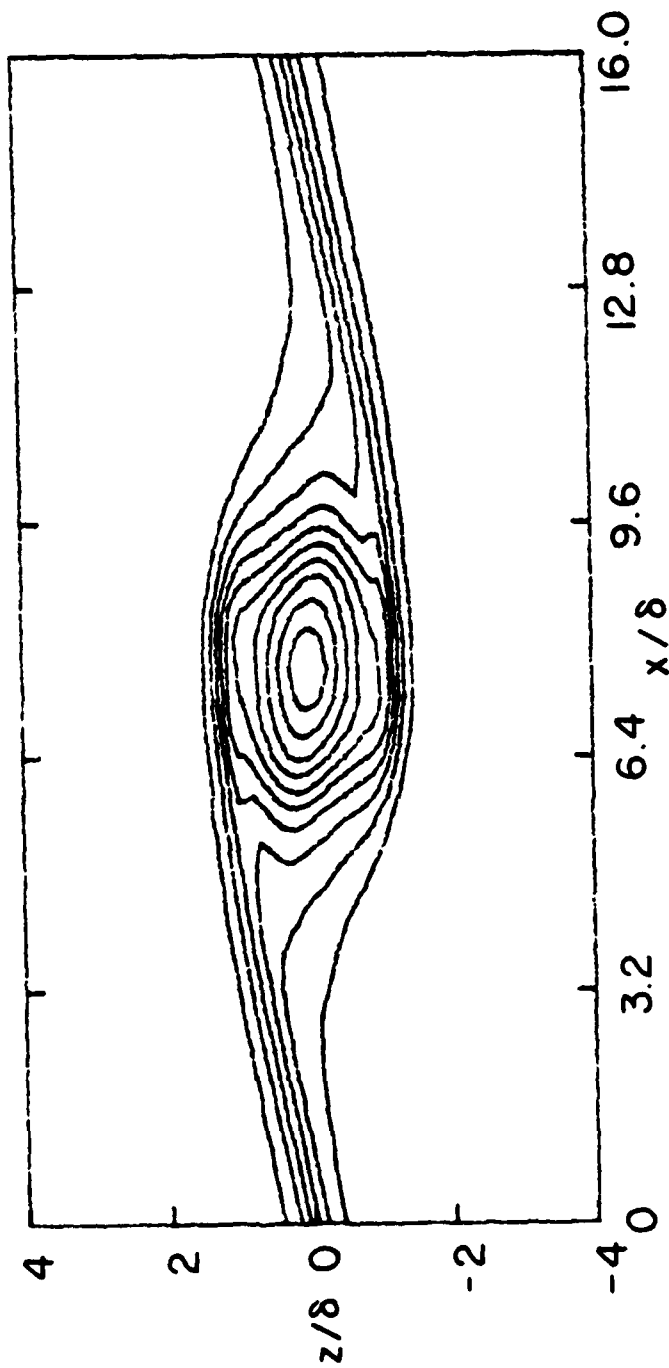
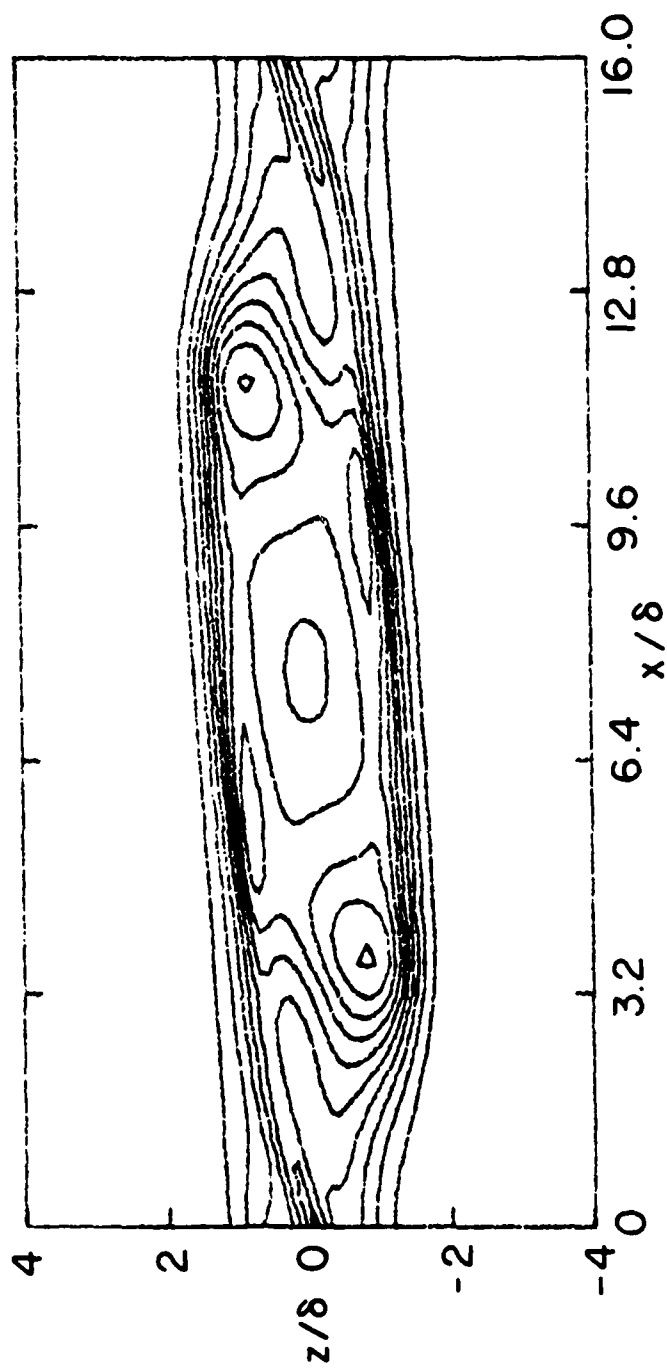Figure A.6(b) – τ = 6, contour interval is 0.006.

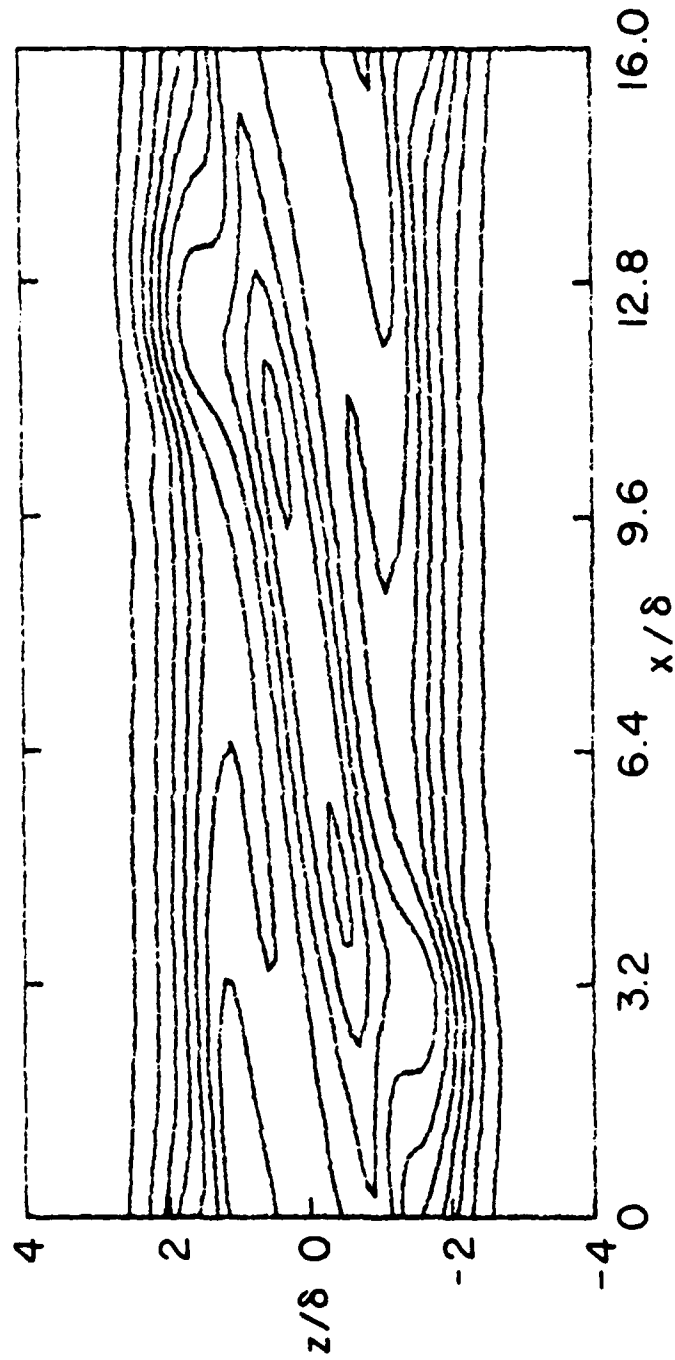Figure A.6(c) – τ = 9, contour interval is 0.007.

94

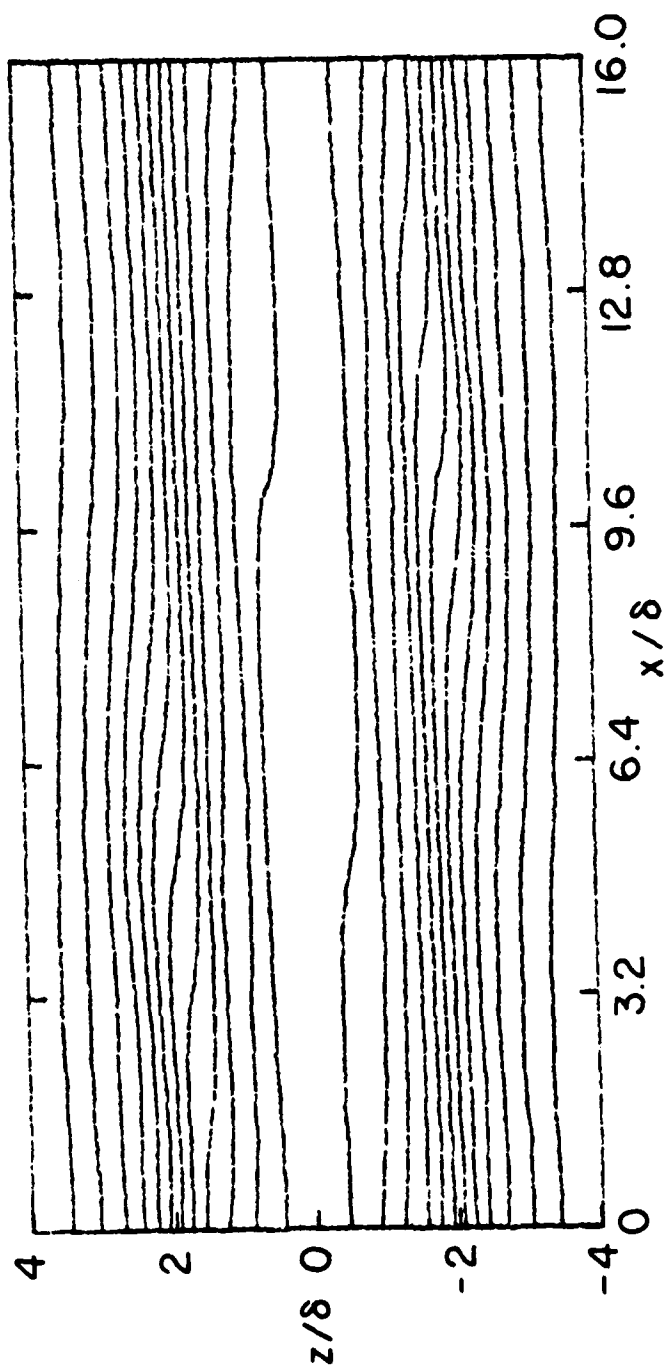Figure A.6(d) – τ = 14.6, contour interval is 0.003.

Figure A.6(e) - $\tau = 20.6$, contour interval is 0.001.

96

kinetic energy available in the mean shear to drive the instability against the restoring buoyancy forces. The higher initial Richardson number also makes the turbulent kinetic energy production in the braids less important, so that at $\tau = 3$ when the isotherms are only just being overturned, the maximum energy is already in the vortex core. Furthermore, the restricted size of the vortex core appears to result in the turbulence being spread throughout the region rather than being confined to the outer half of the vortex as in the $Ri = 0.1$ case. The velocity in the core is also smaller in the $Ri = 0.2$ case, so there is less tendency for the turbulence to be swept around the outer part of the vortex.

As in the $Ri = 0.1$ case, the turbulent vortex core spreads horizontally, with small scale waves running along the top and bottom of the layer producing local turbulence maxima. Finally, the mean motion is totally suppressed, and the isotherms become horizontal, and we have a homogeneous layer of turbulence.

The evolution of the large- and small-scale kinetic energies is shown in Figure A.7. Comparing this with Figure A.3, we see that the large-scale roll-up extracts much less energy than the $Ri = 0.1$ case, but the maximum in small-scale energy is almost as large as the large-scale. Since the small-scale energy arises from the potential energy created by the roll-up process, this demonstrates that there is more potential energy per unit kinetic energy in the $Ri = 0.2$ case. This should not be a surprise, since the Richardson number is a measure of the ratio of potential to kinetic energy in the initial profile, and a linearized disturbance will contain energy in the same proportion.

We may also note that if the time scale for the $Ri = 0.2$ case is divided by two, then a number of features match up with the $Ri = 0.1$ case. Defining $\tau' = \tau/Ri$, then the large scale energy maximizes at $\tau' \approx 50$ in both cases. Furthermore, the small-scale energy is down to about half its maximum value at $\tau = 100$. It seems that the time scale is determined by the shear velocity and the layer thickness, while the buoyancy time scale determines the details of
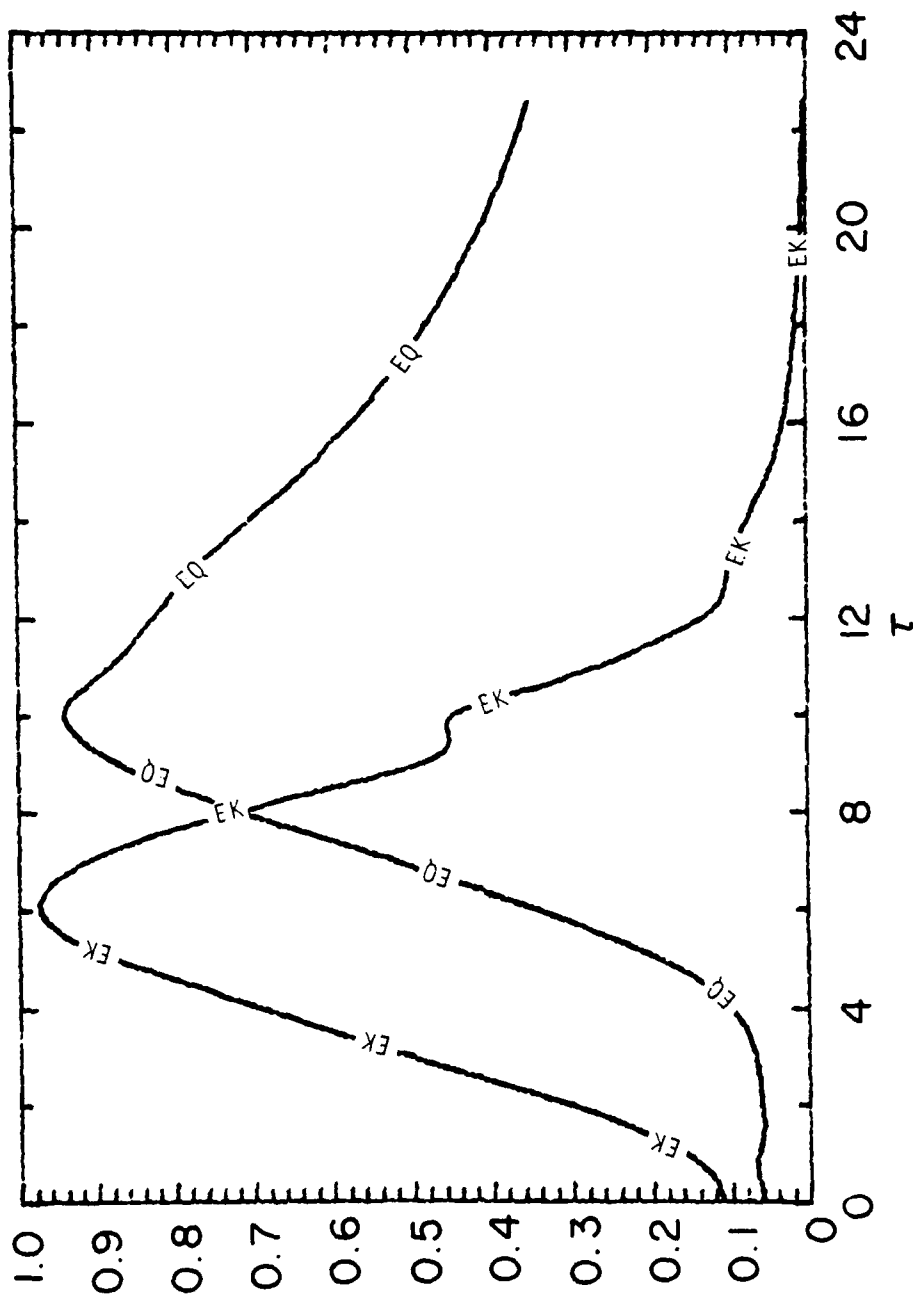
97

Figure A.7 - Evolution of large scale and small scale eddy kinetic energies for the case with Ri = 0.2.

the roll-up such as core size and energy partitioning.

The profile of gradient Richardson number at the final time, τ = 20.6. is shown in Figure A.8 for the case with initial Ri = 0.2. The final state is a region of virtually constant Richardson number at a value of roughly 0.45, slightly larger than the case with Ri = 0.1. The laboratory experiments of Thorpe (1973) indicate that the final Richardson number is independent of the initial value, the final value being between 0.26 and 0.385, but this result is for initial Richardson number less than 0.14.

In considering atmospheric observations, we must recognize the fact that the high-resolution radars are measuring small-scale refractive index changes. As discussed in Chapter II, the latter are very closely related to humidity and temperature fluctuations rather than the turbulence energy itself. Since humidity is a scalar, it satisfies the same equation as temperature, and it can be shown that the mean square humidity fluctuations are identical to the mean square temperature fluctuation provided the initial profiles are identical. It is therefore instructive to look at the behavior of temperature fluctuations, remembering that asymmetries can be introduced by having an asymmetric humidity profile. In fact, the length scale of the energy-containing turbulent eddies also affects the refractive index fluctuations at the short wavelengths visible to the radar, but variations in the length scale do not produce any significant changes in the pattern.

Contours of the mean square temperature fluctuation, $\overline{\theta^2}/\Delta T^2$, for the case with initial Ri = 0.1 are shown in Figure A.9 at τ = 1.5, 2.8, 4.3, and 8.8. The most obvious feature is the highly localized nature of $\overline{\theta^2}$. Initially, $\overline{\theta^2}$ is concentrated in the developing braids, where the temperature gradient is very large. As the billow begins to break, there are local patches of high temperature variance in the mixing regions around the edges of the core, but these patches do not spread throughout the vortex core as it breaks. Rather, as the vortex breaks down, the temperature variance vanishes, and only remains in the braids at τ = 4.3. As the braids are eroded by the turbulent mixing, the temperature variance decays, but remains in narrow bands which are drawn

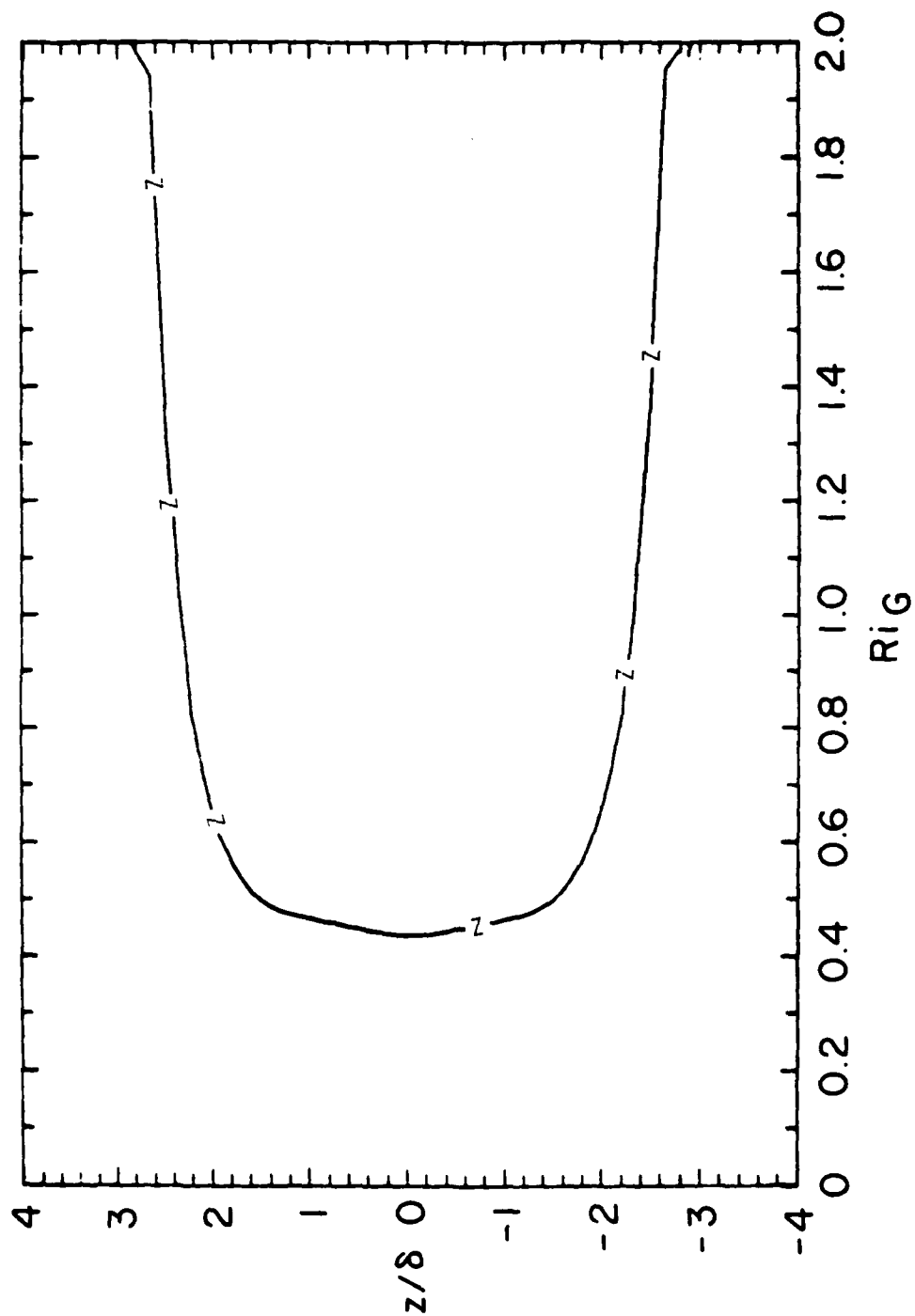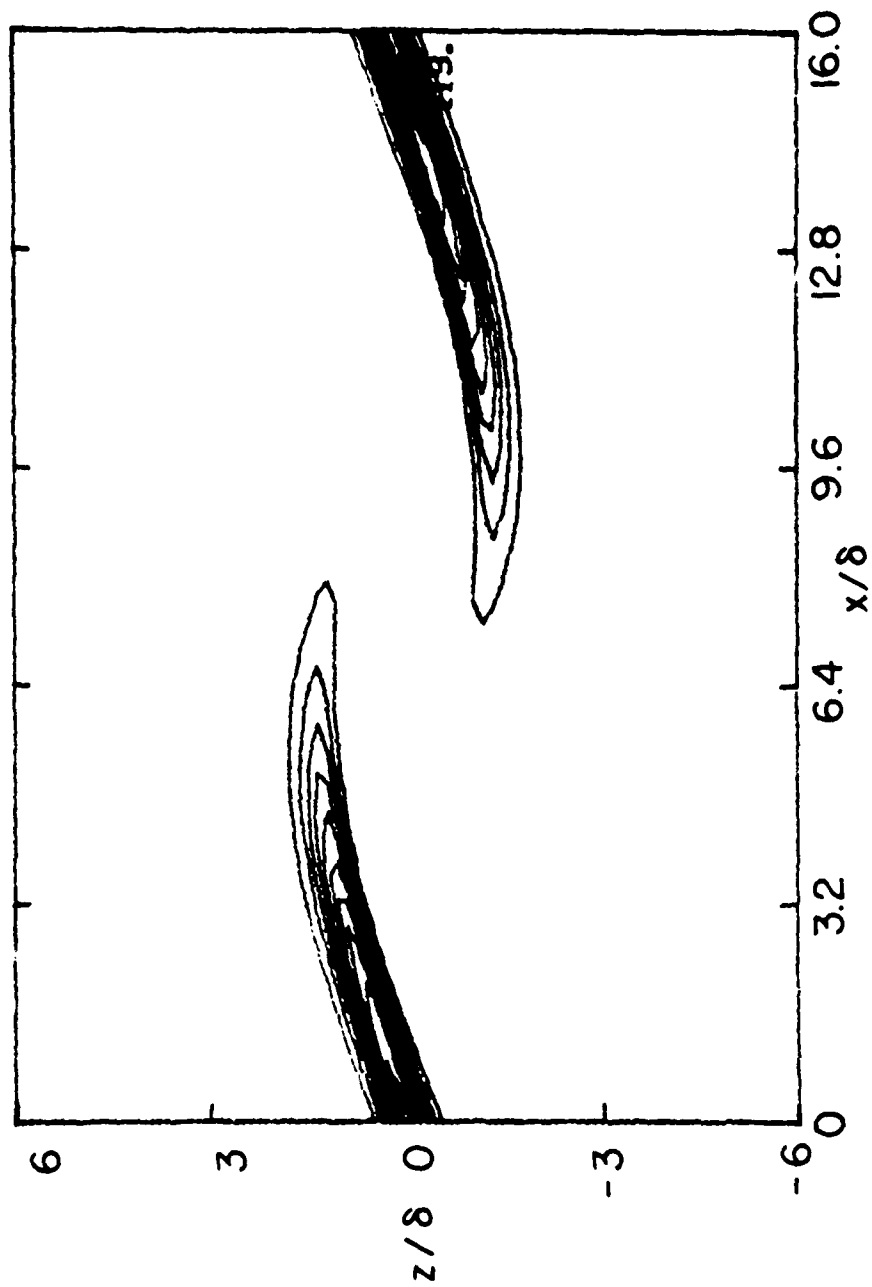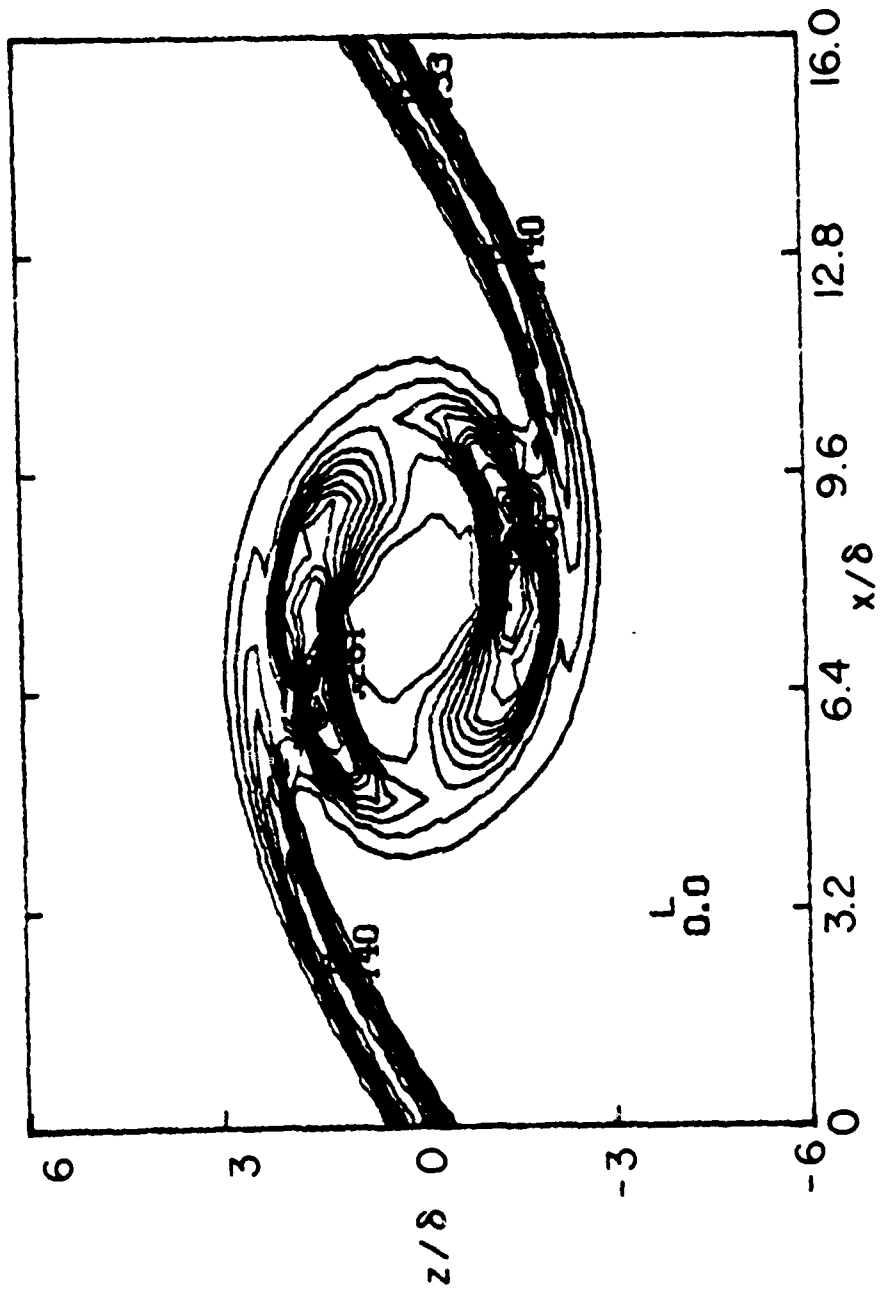Figure A.8 - Profile of gradient Richardson number, Ri_G, for the $Ri = 0.2$ case, at $\tau = 20.6$.

Figure A.9 - Isopleths of dimensionless temperature variance $\overline{\theta^2}/\Delta T^2$ for the case with Ri = 1. (a) τ = 1.5, contour interval is 0.004.

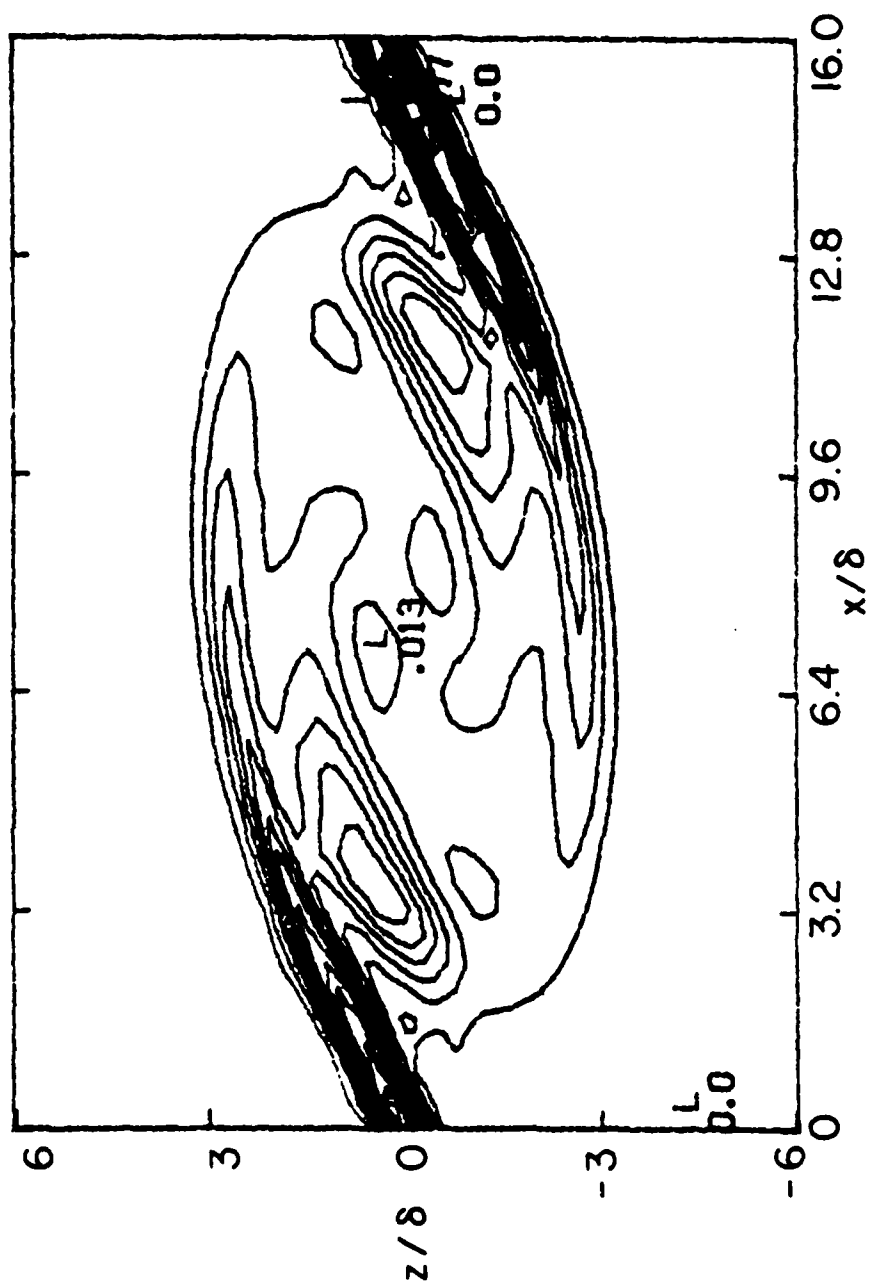Figure A.9(b) - τ = 2.8, contour interval is 0.02

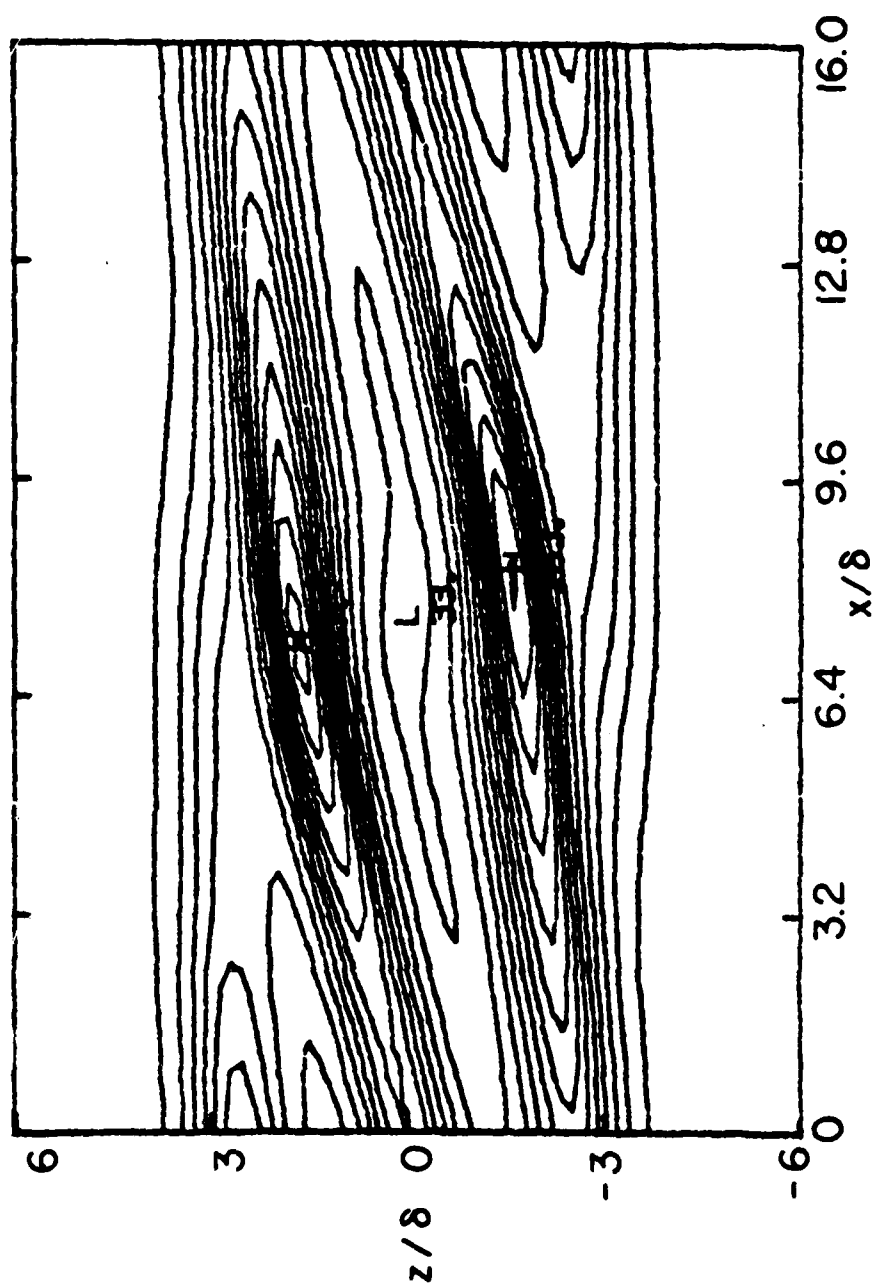Figure A.9(c) - $\tau = 4.3$, contour interval is 0.02.

Figure A.9(d) – $\tau = 8.8$, contour interval is 0.002.

out horizontally until they are almost flat. This qualitative description also applies to the Ri = 0.2 case.

The difference between the temperature variance and velocity variance is also evident by comparing Figure A.10 with Figures A.3 and A.7. The integrated value of the temperature variance tends to both grow and decay more rapidly then the integrated velocity variance.

The contrast in behavior between the temperature variance and turbulent kinetic energy may be somewhat better understood by examining the production terms in the second-order turbulence correlations. We have

$$P(q^2) \quad = \quad - 2 \, \overline{u_i u_k} \, \frac{\partial U_j}{\partial x_k} + \frac{2g}{T_0} \, \overline{w\theta} \tag{A.18}$$

$$P(\overline{w\theta}) \quad = \quad - \overline{w^2} \frac{\partial T}{\partial z} - \overline{uw} \frac{\partial T}{\partial x} - \overline{w\theta} \frac{\partial W}{\partial z} - \overline{u\theta} \frac{\partial W}{\partial x} + \frac{g}{T_0} \, \overline{\theta^2} \tag{A.19}$$

$$P(\overline{\theta^2}) \quad = \quad - \overline{w\theta} \frac{\partial T}{\partial z} - \overline{u\theta} \frac{\partial T}{\partial x} \tag{A.20}$$

where P( ) denotes production terms. The only other terms in the relevant equations are diffusion and dissipation terms. Now, as the vortex core rolls up, large gradients of mean quantities are generated, and consequently the production terms are also large.

Once the vortex breaks the mean gradients are rapidly mixed away, and therefore there is only diffusion and dissipation of $\overline{\theta^2}$ which must begin to decay immediately. However, there is still production of $\overline{w\theta}$ due to the term involving the temperature variance. Thus heat flux does not decay as quickly as $\overline{\theta^2}$. Furthermore, $\overline{w\theta}$ is the main production term in the q^2 equation within the core, so the turbulent kinetic energy continues being produced while $\overline{\theta^2}$ is
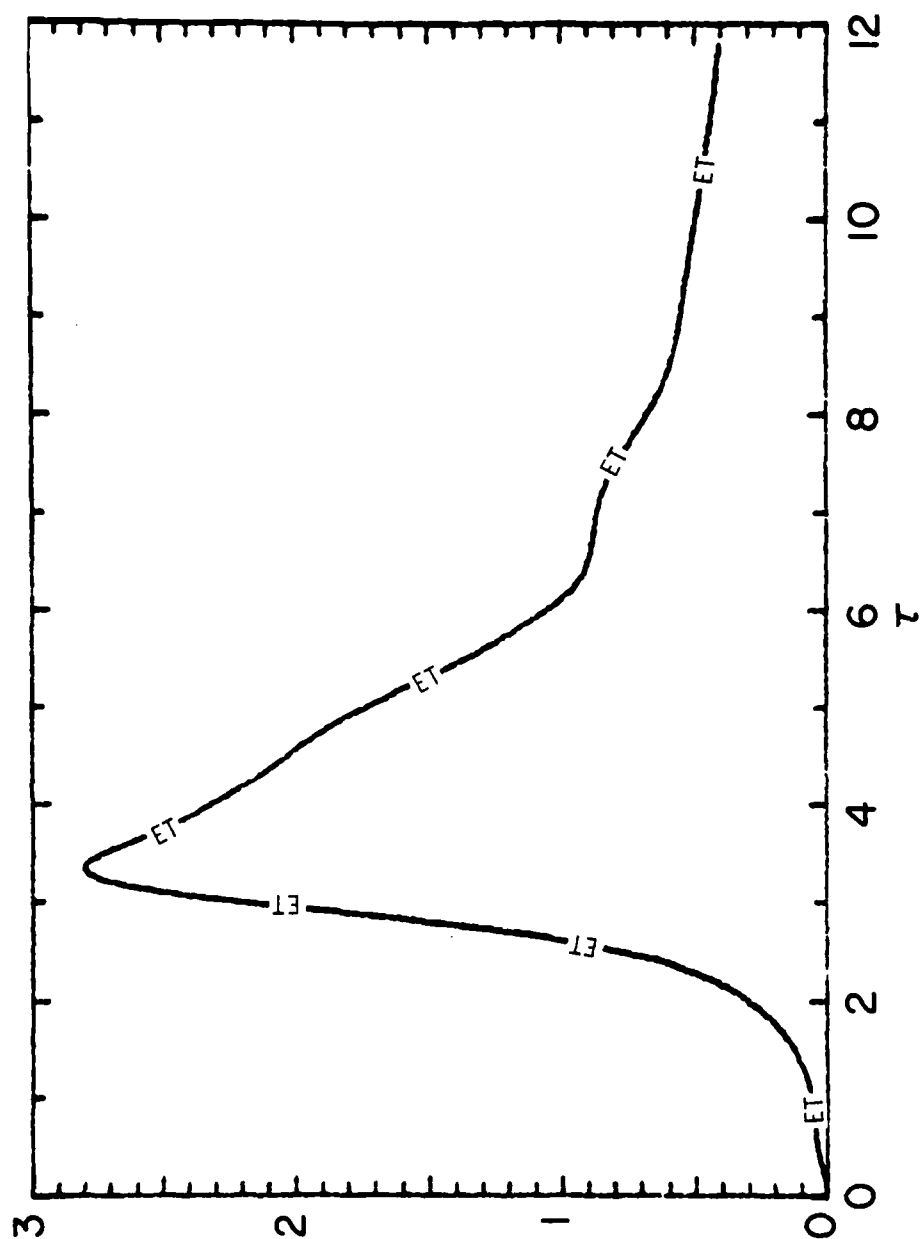
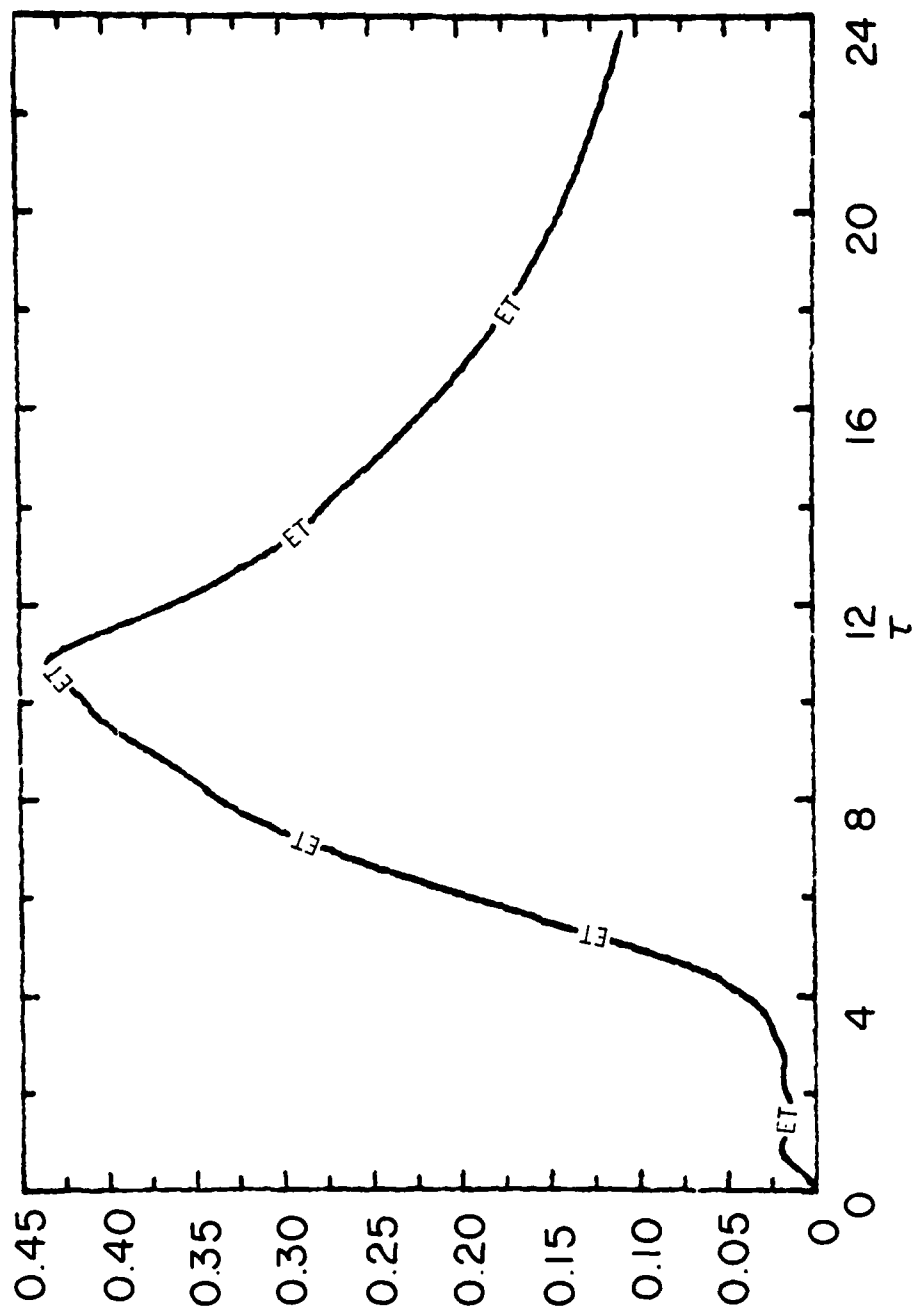Figure A.10(a) - Evolution of the total volume-integrated temperature variance, ET, for the case with Ri = 0.1.

Figure A.10(b) - Ri = 0.2.

107

decaying. Thus q^2 grows in the core, and eventually spreads outward horizontally, whilst $\overline{\theta^2}$ vanishes in the core, and only remains significant in the braids, where there is gradient production. When the braids are eroded, the temperature variance is slowly diffused and dissipated, while the mean shear stretches the regions of high $\overline{\theta^2}$ into nearly horizontal stratifications.

The differences between the q^2 and $\overline{\theta^2}$ patterns are thus quite plausible. We note that this dynamical effect could not be reproduced by an effective viscosity model which has no equivalent interaction between second-order quantities. We should also note the implication that high resolution radar returns from atmospheric billow events of this type should always show highly-structured patterns with narrow bands of high intensity, rather than a homogeneous layer of turbulence. This is quite consistent with the observations reported in the literature (See Section 3.2). Figure A.11 showing the evolution of K-H wave breaking as received by radar (Browning and Watkins, 1970) shows the same features as exhibited in Figure A.9.

A.4 Sensitivity Studies

There are a number of parameters in the numerical integrations presented in the previous section which must be chosen independently from the physical constants of the problem. These parameters include numerical discretization quantities such as the grid size and initial conditions for the dynamic variables. We do not include the empirical constants in the second-order turbulence closure model, since these are taken to be fixed from comparison with other experimental data. It is important to obtain some indication of the dependence of the results or these external parameters if we are to gain a useful understanding from the numerical integrations. The few main quantities which need to be chosen are:

A.4.1   numerical resolution

A.4.2   initial turbulence level

A.4.3   initial turbulence length scale

A.4.4   length of the integration domain
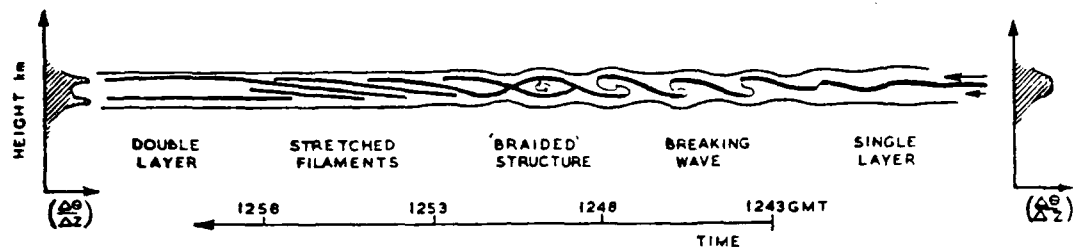
Figure A.11 - Schematic representation of the life cycle of an individual Kelvin-Helmholtz billow based on the data in the earlier figures. Time progresses from right to left. Thick lines correspond to the detectable clear air radar echo, which started as a single layer at 1243 and finished as a double layer at 1258 GMT. Schematic vertical profiles of $(\Delta\theta/\Delta z)$ are indicated before and after the occurrence of Kelvin-Helmholtz instability. (From Browning and Watkins, 1970.)

We shall investigate variations in each of these quantities independently for the case with Ri = 0.2.

A.4.1   Numerical resolution. The integration presented in the previous section was carried out with a mesh of 41×61 points; this was chosen to provide adequate resolution of the small scale flow features. This fact is demonstrated by comparing the results with those from an integration using 32×40 grid-points. The kinetic energy evolution from both integrations is shown in Figure A.12. Unfortunately, the low resolution integration had a slightly smaller initial vorticity perturbation which is responsible for some of the differences, but notwithstanding this initial discrepancy, the overall budgets are within about 10%.

Contour plots from the two runs show that the low resolution integration has much more numerical noise around the point where the vortex is breaking and gradients are highest. However, this does not adversely affect the evolution, as can be seen from the kinetic energy plots, and the two integrations do remain very close together throughout the period.

A.4.2   Initial turbulence level. The remaining sensitivity tests are all carried out using the low resolution model, so we are comparing with the run in Figure A.12(b). Figure A.13 shows the kinetic energy evolution using an initial value for q^2 of 3×10^{-3}, which is three times that of the previous run. The main effect here is a reduction in the large scale energy by about 12%, and an increase of about 10% in the small scale energy maximum. Thus a higher background turbulence level retards the development of the instability slightly, and also allows the vortex to break a little more quickly, extracting more of the potential energy from the roll-up. However, the effect is not large, and it can be reasonably assumed that the results are representative of small background turbulence levels. In fact, the initial value for q^2 was chosen as large as reasonably possible in order to provide some turbulent mixing to prevent the braids from becoming too thin to be resolved by the numerical grid. Since the growth of q^2 in the breaking is via the buoyancy term, it is virtually independent of the initial value for q^2,
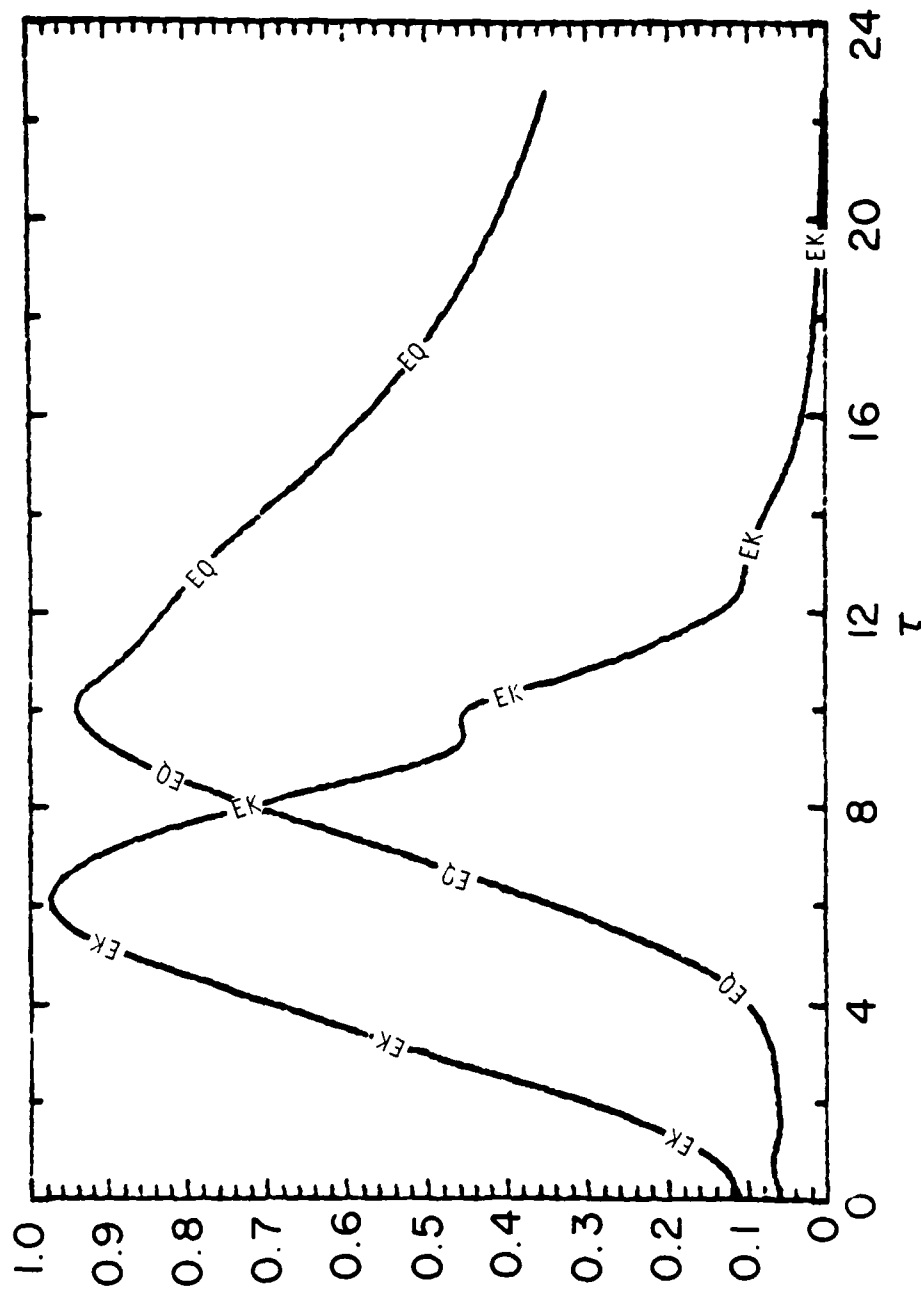
Figure A.12 - Evolution of eddy kinetic energies for Ri = 0.2 with (a) high resolution 41 x 61.
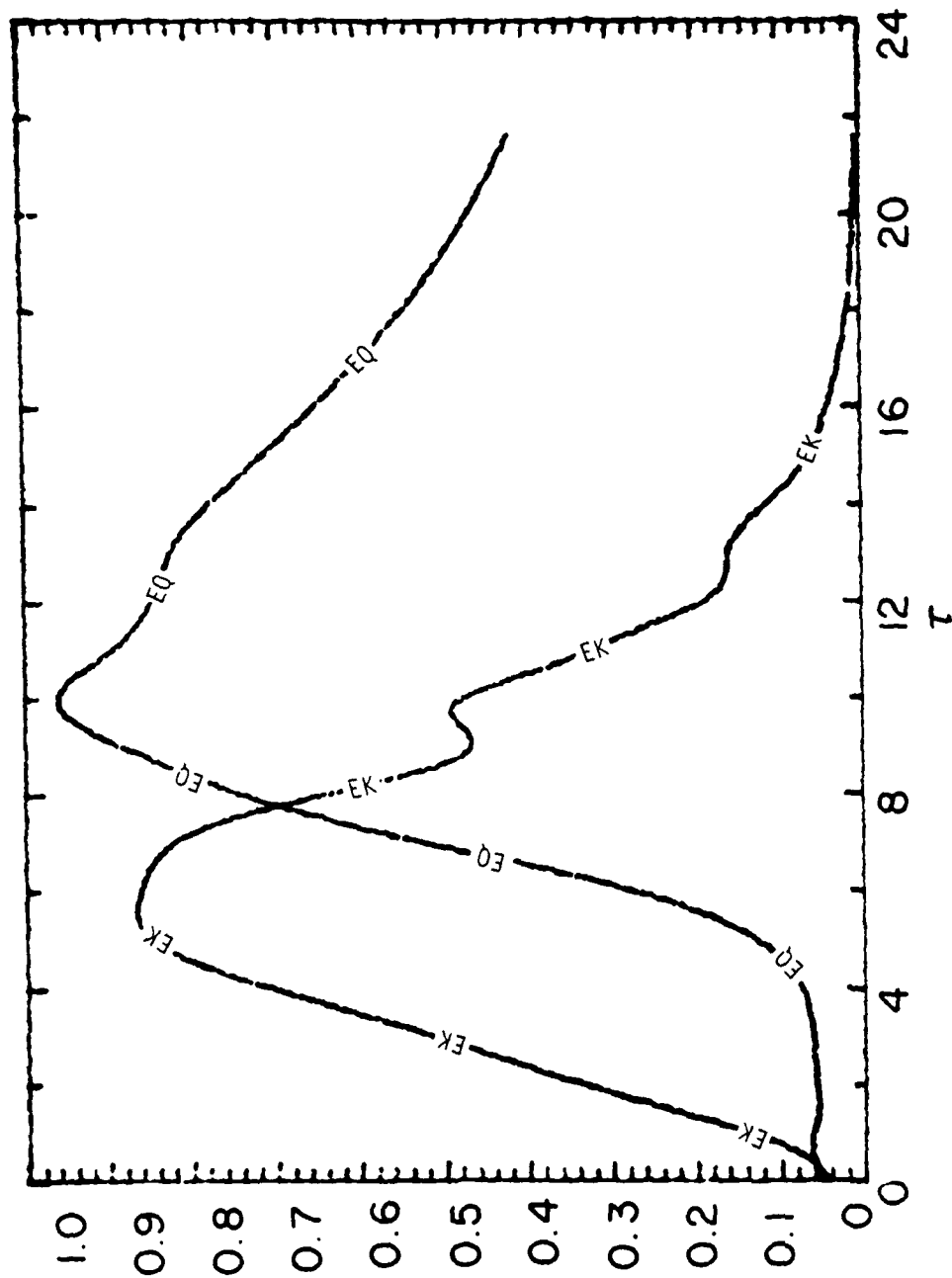
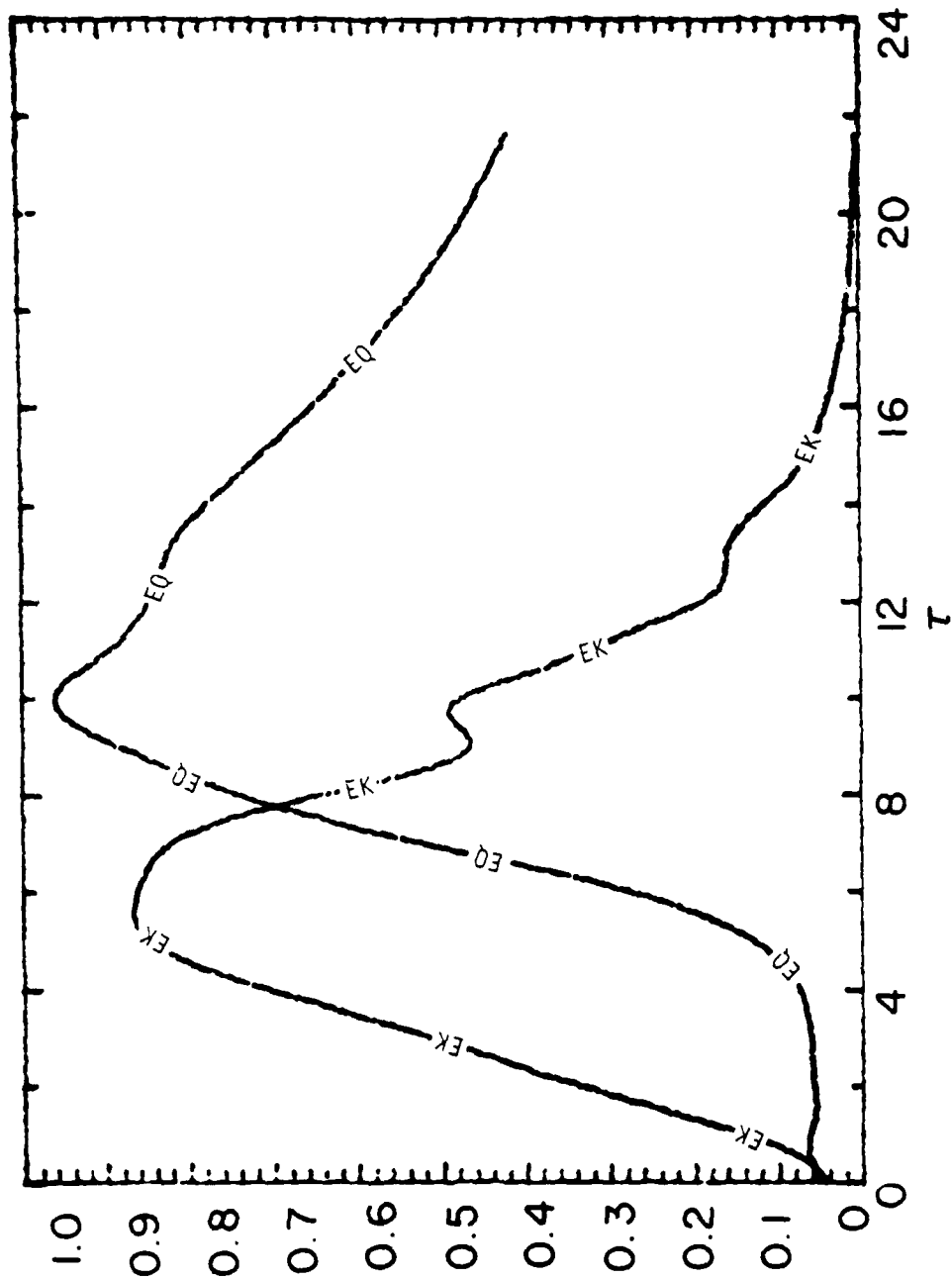Figure A.12(b) - low resolution 32 x 40.

112

Figure A.13 - Evolution of eddy kinetic energies for Ri = 0.2 with different initial values of $q^2/\Delta U^2$, (a) 10^{-3}.
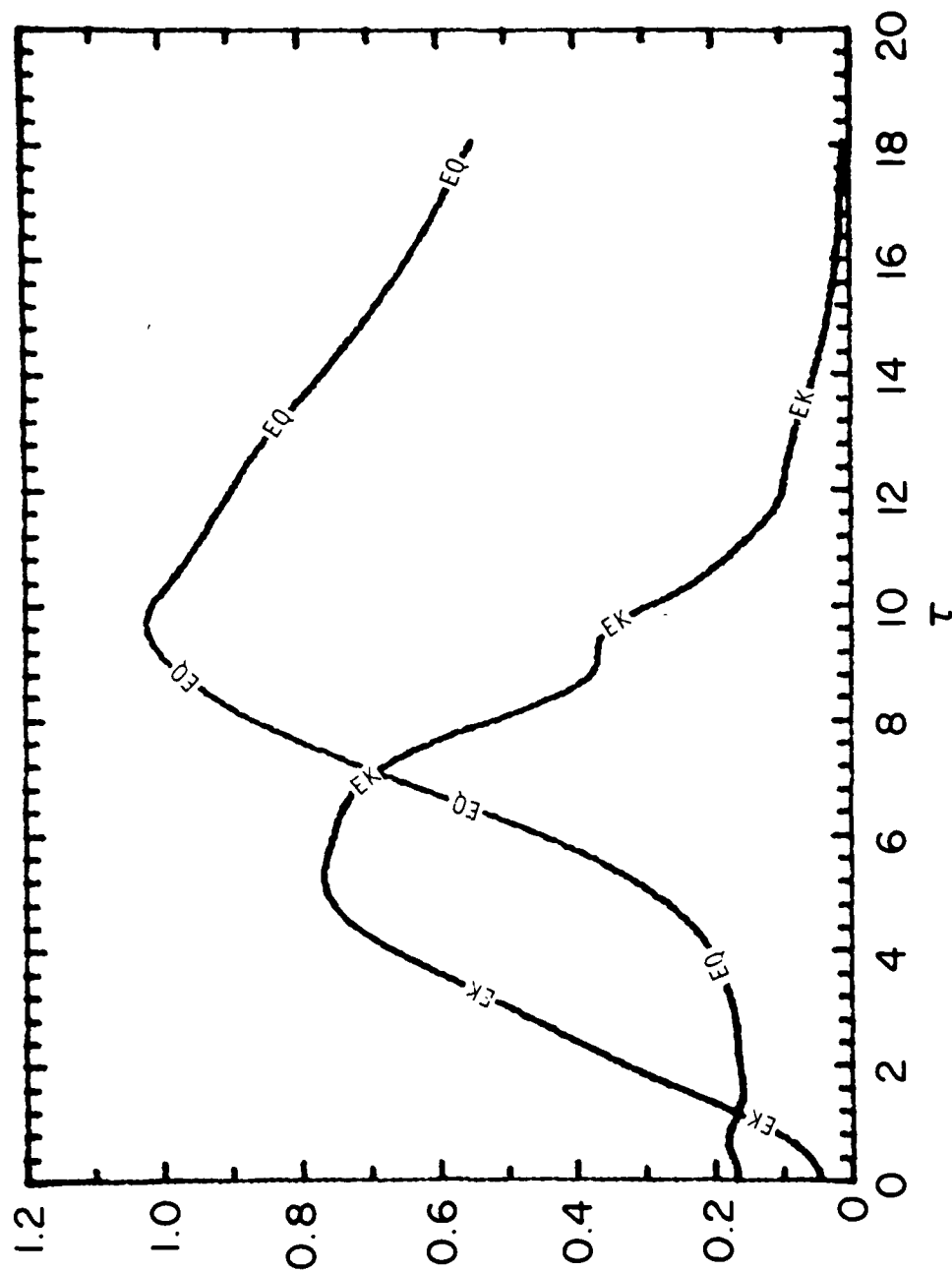
113

Figure A.13(b) — 3×10^{-3}.

due to the rapid exponential growth in the initial stages. We therefore feel justified in choosing q^2 large enough to control the braid thickness, as long as it is not large enough to influence the dynamics of the breaking.

Although the higher value of initial q^2, 3×10^{-3}, appears to have a small effect on the energy budgets, there was much less energy in the short numerical grid modes, so this run was chosen as the base integration for comparison of turbulence length scale and domain length variations.

A.4.3   <u>Initial turbulence length scale.</u> This is probably the most difficult and unfortunately one of the most sensitive parameters to choose. The choice of initial Λ is not entirely arbitrary, since it must bear some relation to the thickness of the shear layer, δ, if we are studying turbulence generated by the instability mechanism itself. We chose the value 0.4δ for the runs presented in the previous section; this is a reasonable value for a turbulence length scale, but cannot be justified too strongly. In order to test the sensitivity, we carried out integrations with initial $\Lambda = 0.2\delta$ and 0.8δ, and the energy evolutions from all three runs are shown in Figure A.14.

Firstly, the large scale kinetic energy is largely unaffected by the choice of Λ. The only difference is in the oscillation in the decaying phase of EK, which is accentuated by small values of Λ. However, the small scale energy does depend quite strongly on the initial value of Λ. Changing Λ by a factor of 2 in either direction from 0.4δ changes the maximum turbulence energy by almost a factor of 2 in the same direction. The source of the problem is the length scale equation, which does not allow the length scale to grow sufficiently quickly during the breaking stage, so that the turbulence <u>does</u> remember its initial condition for a long time. The length scale does grow as the billow breaks, but not so fast as q^2 which is virtually independent of its initial condition.

On this point, all we are able to say is that 0.4δ is a reasonable initial value for Λ, and the results of this section illustrate the effect of varying Λ. We should emphasize that the qualitative results, both in the
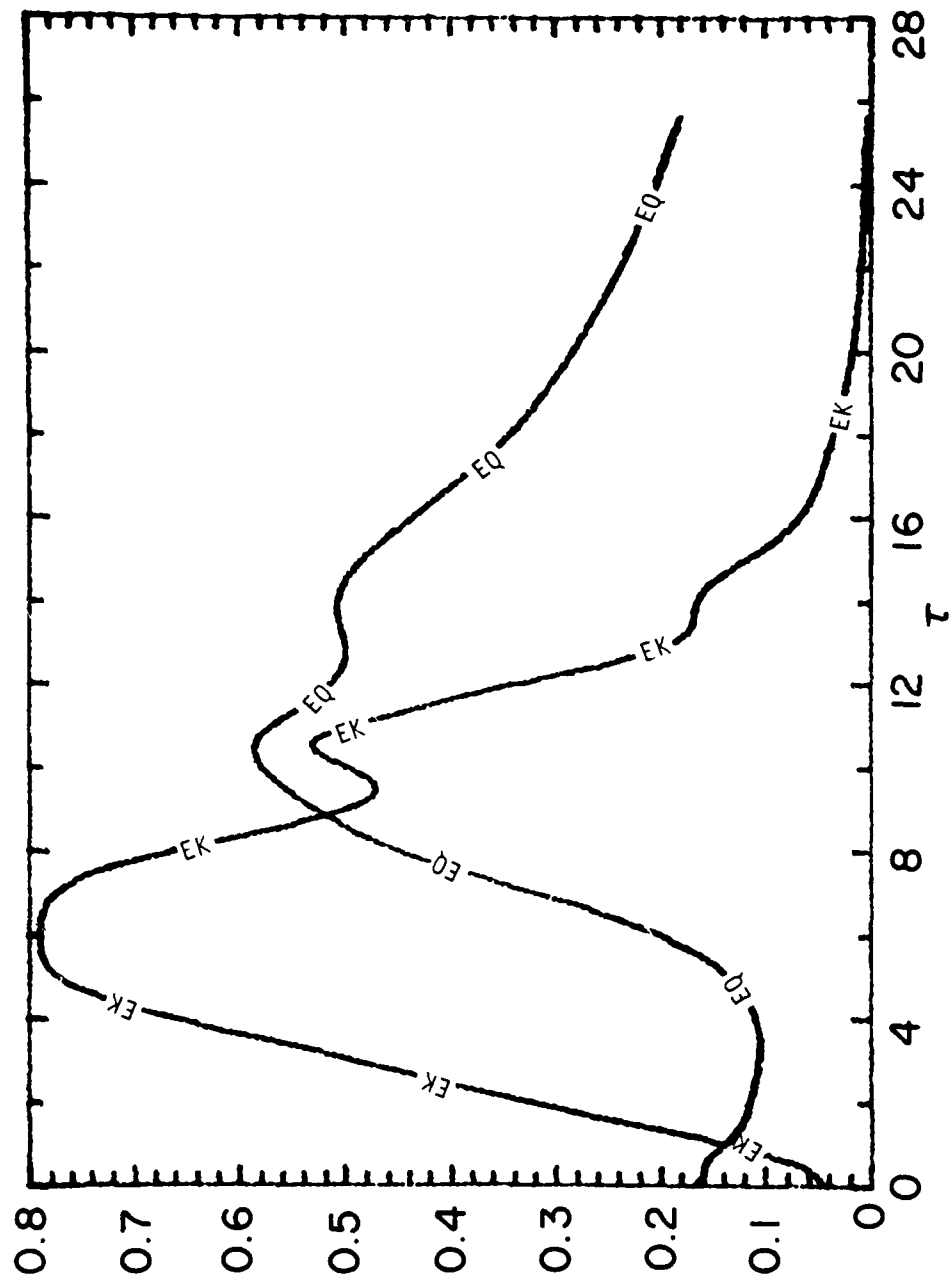
115

Figure A.14 - Evolution of eddy kinetic energies for Ri = 0.2 with different initial values of Λ/δ, (a) 0.2.
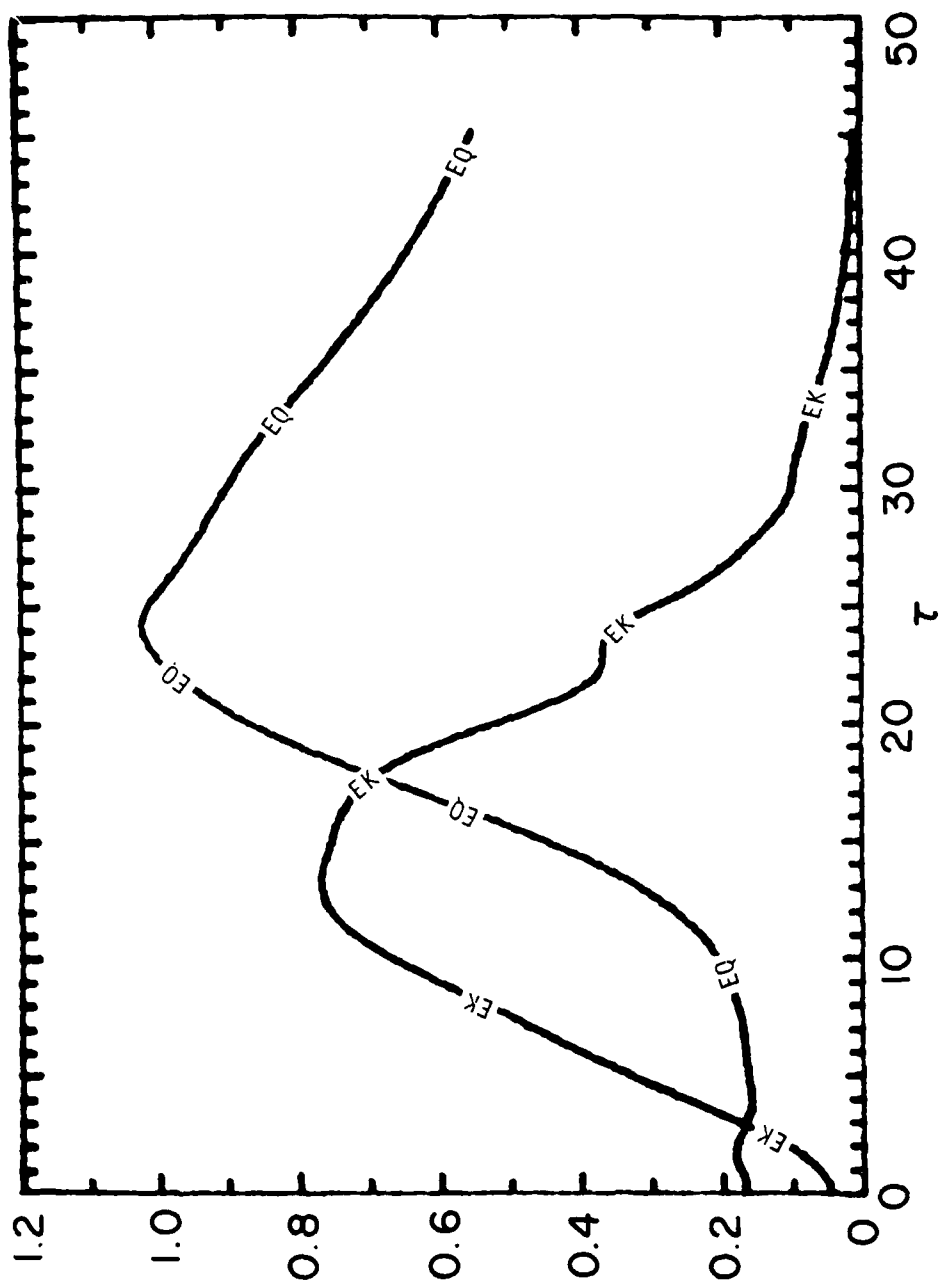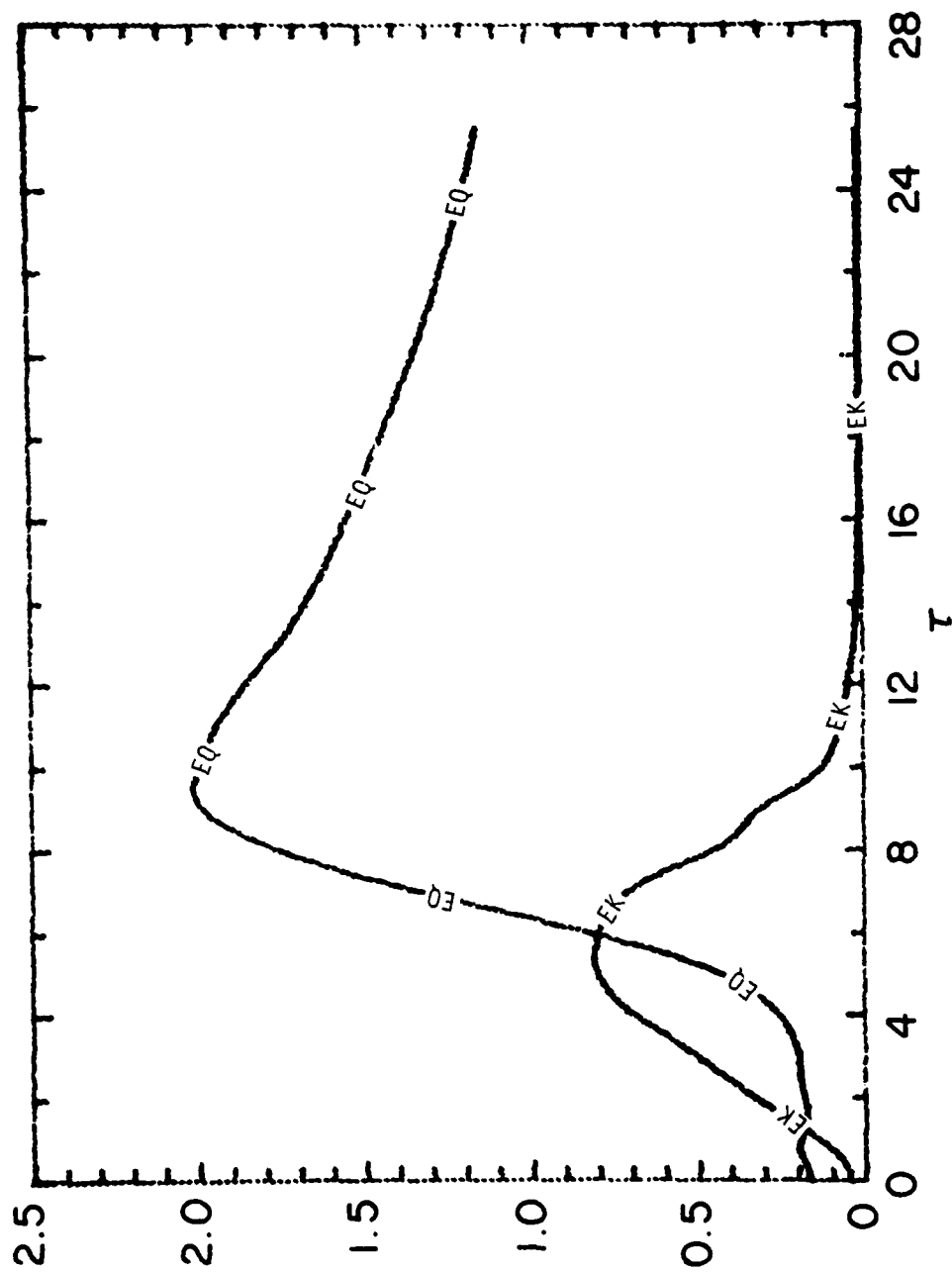
116

Figure A.14(b) - 0.4.

117

Figure A.14(c) - 0.8.

118

energy plots and the details of the contour fields, are not significantly changed by this variation in Λ. Apparently the initial value for Λ ought to be fixed by comparison of turbulence levels with experimental observation, or an improved dynamical equation for Λ is needed.

A.4.4   Integration domain length. We choose the wavelength of the unstable mode we are studying by fixing the length of our periodic domain. The runs in the previous section used a length of 15δ, which was suggested by the laminar numerical integrations of Patnaik, et al. (1976) as giving the mode which grew to largest amplitude.

Figure A.15 shows the energies from three runs with domain lengths of 10δ, 15δ, and 20δ. Allowing for the length of the domain, the short domain clearly restricts the growth of the billow significantly; the large scale energy maximum is nearly a quarter of the 15δ domain case (i.e., the energy density is about 35%), and the turbulence energy is about half (i.e., energy density is 70%). It is therefore unlikely that this mode would be the dominant finite amplitude mode, since the longer modes would continue to grow. The long domain, 20δ, has a significantly larger energy in the vortex, but allowing for the length of the domain, the energy density per unit horizontal length is only a little longer. The turbulence energy per unit length is actually smaller.

Thus the case with a domain length of 15δ seems to represent the most efficient mode for producing kinetic energy, although there is not a great deal of difference with a length of 20δ.

A.5 Conclusions

This two-dimensional numerical study of breaking Kelvin-Helmholtz waves using a second-order turbulence closure model to describe the small-scale turbulence has shown agreement with experimental observations on several points. More importantly, given the lack of precise quantitative experimental data, the numerical integrations have suggested several general features of
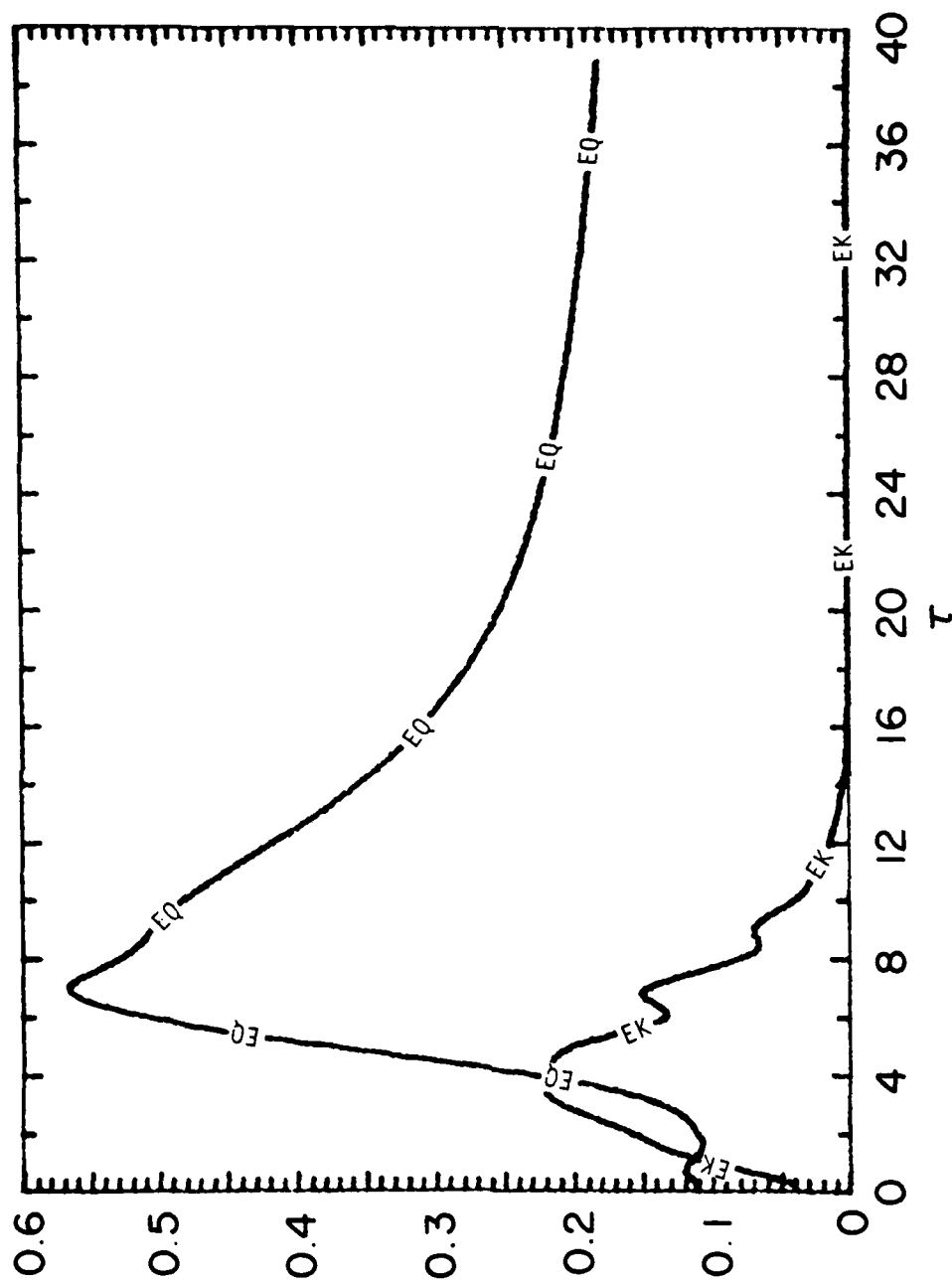
119

Figure A.15 - Evolution of eddy kinetic energies for Ri = 0.2 with different domain lenghts, (a) 10δ.
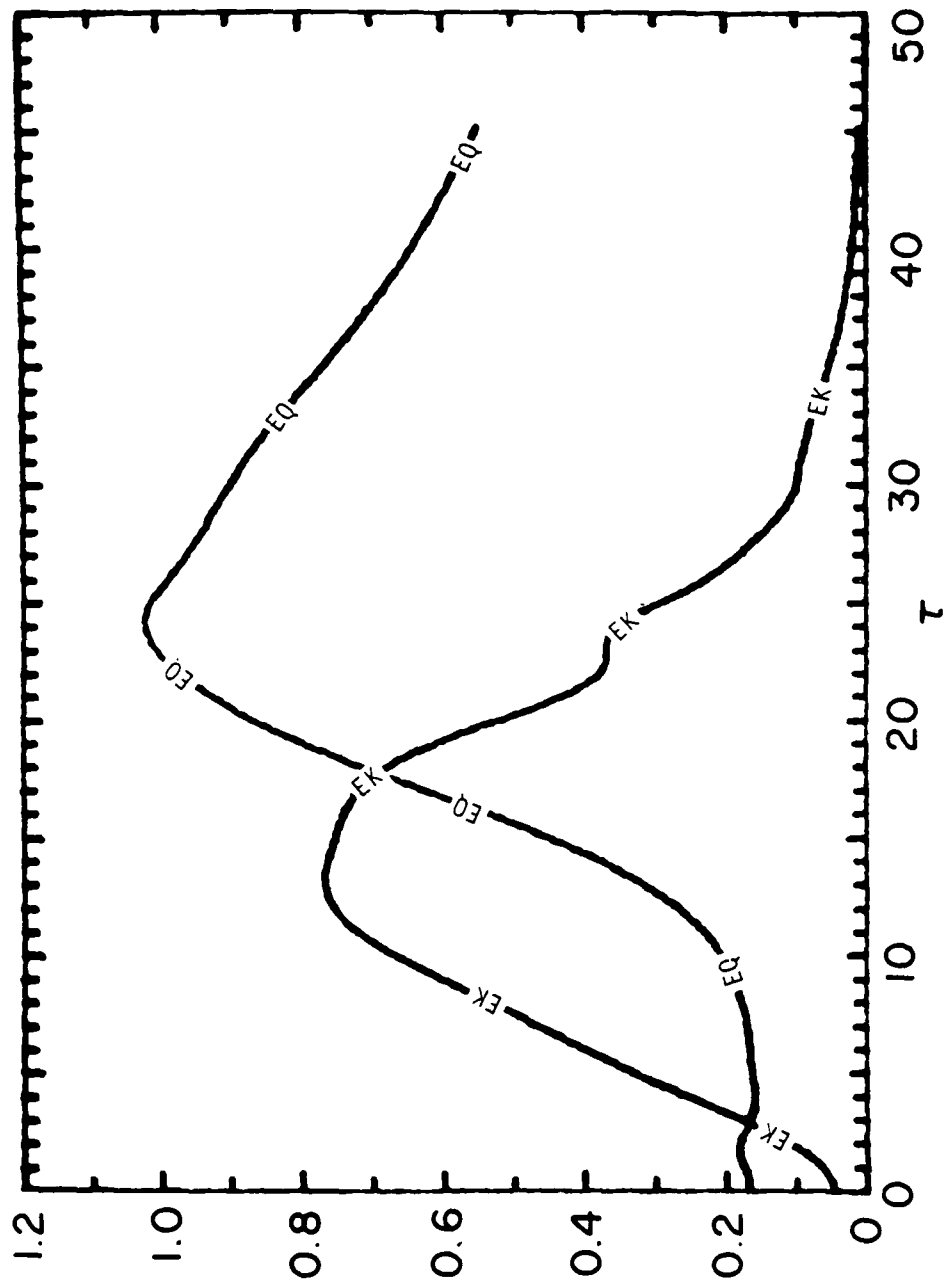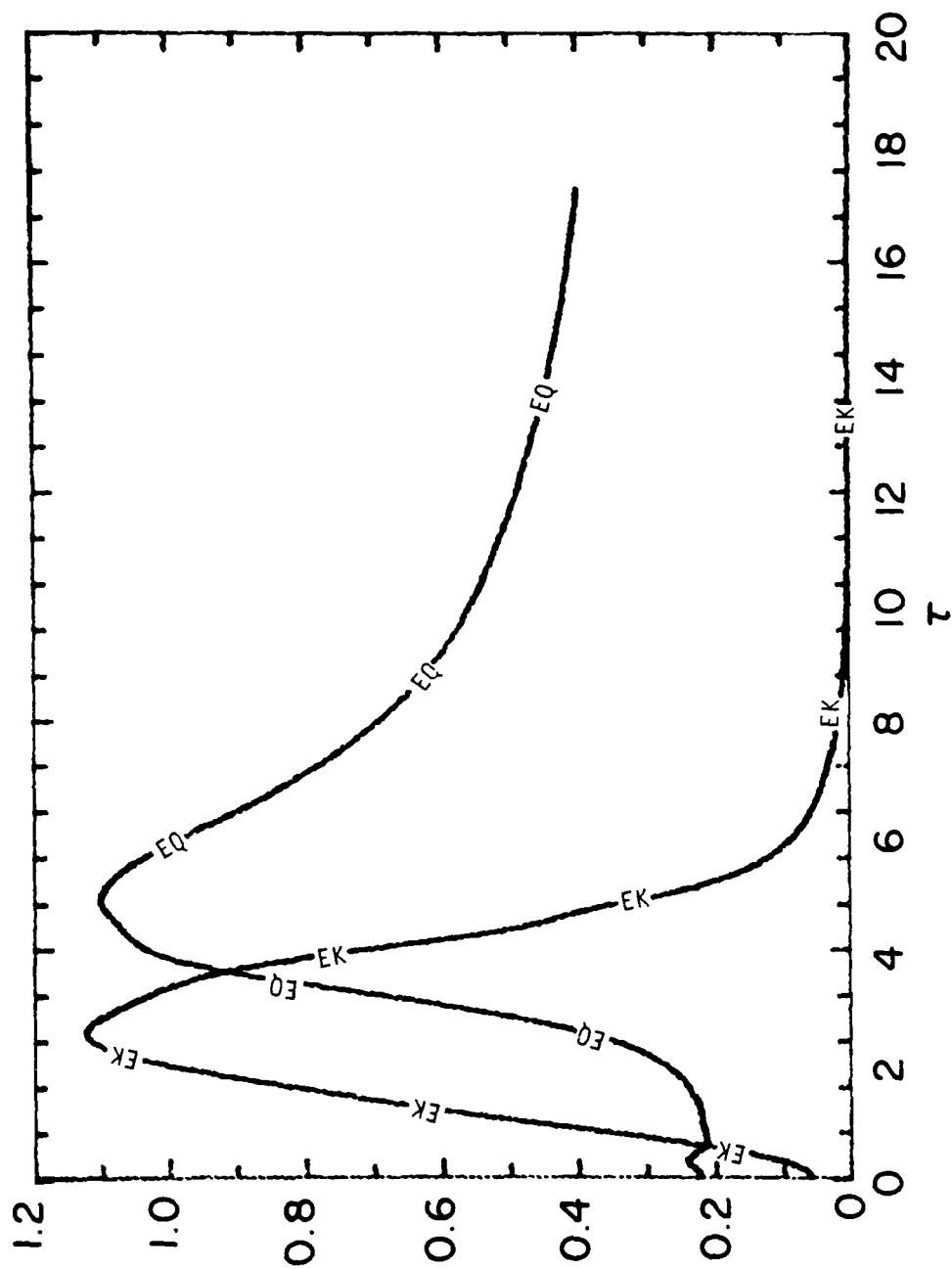
Figure A.15(b) - 15δ.

121

Figure A.15(c) - 206.

122

the dynamics of the fine-scale turbulence in addition to the specific quantitative predictions of the particular cases studied. These general points await further experimental evidence to provide confirmation or refutation.

The results demonstrate the utility of the closure model in studying this problem; closure model contains most of the important dynamical effects necessary for a description of the flow. Furthermore, it is probably the minimum sophistication capable of describing the fine-scale turbulence, since it has shown that the turbulence develops on the same time scale as the mean flow, so that equilibrium assumptions would not be correct.

The numerical results indicate the correct qualitative behavior, namely the billow breaks to produce turbulence in the vortex core, which then spreads horizontally to form a homogeneous layer. The layer also spreads a little vertically. The time-scale and extents of the spreading are in broad agreement with the visual observations of Thorpe (1973). The final value of the Richardson number for an initial Ri of 0.1 is consistent with Thorpe's measured value of 0.32 ± 0.06. Moreover, Thorpe notes no dependence on initial Ri for Ri < 0.14, whilst our final value for Ri = 0.2 is significantly higher. It remains to be clarified whether the experiments would show such a trend at higher values of Ri.

The integrations at different initial Richardson numbers suggests that the advective time scale $\ell/\Delta U$, where ℓ is the wavelength of the billow and Δu the velociity difference across the shear layer, is the important time scale for the growth, breaking, and subsequent decay of the turbulence. The buoyancy time scale affects the type of flow since the ratio of the time scales is proportional to the square root of the Richardson number. It is quite possible that the buoyancy time scale is also important in the late stages of the decay, when the turbulent eddies collapse as the mean density gradient is re-established. We have not attempted to seriously study this part of the evolution, since the closure model has deficiencies in the limit of strongly-stratified turbulence.

The breaking of the billow itself is seen to be generated by a convective instability of the overturned fluid at the top and bottom of the vortex core. This turbulence is swept around the vortex, and actually remains largely in the outer part of the vortex for a significant length of time in the small Richardson number case. The turbulence eventually spreads throughout the layer, and amalgamates to form a horizontally homogeneous layer.

Finally, the results indicate that the temperature variance, $\overline{\theta^2}$ evolves quite differently from the turbulent-kinetic energy. Different buoyancy production terms in the second-order turbulence correlation equations imply the rapid decay of $\overline{\theta^2}$ in the breaking vortex core, so that the regions of high $\overline{\theta^2}$ remain highly localized in space. Effectively, $\overline{\theta^2}$ is generated initially in the braids of the developing billow, and these long thin patches are then stretched out by the mean shear as they diffuse and decay after the braids have been moved away. The evolution of the Kelvin-Helmholtz wave breaking as observed by radar in the atmosphere is quite consistent with the evolution of the variance of humidity or temperature predicted by the model calculation.

References

Ablowitz, M. J., and Segur, H., (1979); "On the Evolution of Packets of Water Waves", J. Fluid Mech. 92, 691-715.

André, J. C., Moor, G., de LaCarrère, P., and Vachat, R. du, (1976); "Turbulence Approximation for Inhomogeneous Flows", J. Atmos. Sci. 33, 476-491.

Anker, D., and N. C. Freeman, (1978); "On the Soliton Solutions of the Davey-Stewartson Equation for Long Waves", Proc. Roy. Soc. London A 360, 529-540.

Apel, J. R., Byrne, H. M., Proni, J. R., and Charnell, R. L., (1975); "Observations of Oceanic Internal and Surface Waves from the Earth Resources Technology Satellite", J. Geophys. Res. 80, 865-881.

Atlas, D., Metcalf, J. I., Richter, J. H., and Gossard, E. E., (1970); "The Birth of 'CAT' and Microscale Turbulence", J. Atmos. Sci. 27, 903-913.

Battan, L. J., (1973); Radar Observation of the Atmosphere, University of Chicago Press.

Browning, K. A., and Watkins, C. D., (1970); "Observations of Clear Air Turbulence by High Power Radar", Nature 227, 260-263.

Browning, K. A., Starr, J. R., and Whyman, A. J., (1973); "The Structure of an Inversion above a Convective Boundary Layer as Observed Using High-Power Pulsed Doppler Radar", Boundary Layer Meteor. 4, 91-111.

Christie, D. R., Muirhead, K. J., and Hales, A. L., (1979); "Intrusive Density Flows in the Lower Troposphere: A Source of Atmospheric Solitons", J. Geophys. Res. 84, 4959-4970.

Clarke, R. H., Smith, R. K., and Reid, D. G., (1981); "The Morning Glory of the Gulf of Carpentaria: An Atmospheric Undular Bore", Monthly Weather Review (submitted).

Davis, P. A., and Peltier, W. R., (1979); "Some Characteristics of the Kelvin-Helmholtz and Resonant Overreflection Modes of Shear Flow Instability and of Their Interaction through Vortex Pairing", J. Atmos. Sci. 36, 2394-2412.

Deardorff, J. W., Willis, G. E., and Stockton, B. H., (1980); "Laboratory Studies of the Entrainment Zone of a Convectively Mixed Layer", J. Fluid Mech. 100, Part I, 41-64.

Erikson, C. O., and Whitney, L. F., (1973); "Gravity Waves Following Severe Thunderstorms", Monthly Weather Review 101, 708-711.

Gardner, C. S., Greene, J. M., Kruskal, M. D., and Miura, R. M., (1967); "Method for Solving the Korteweg-deVries Equation", Phys. Rev. Lett. 19, 1095-1097.

Gardner, C. S., Greene, J. M., Kruskal, M. D., and Miura, R. M., (1974); "Korteweg-deVries Equation and Generalization. VI. Methods for Exact Solution", Comm. Pure Appl. Math. 27, 97-133.

Gedzelman, S., (1981); "Short-Period Atmospheric Gravity Waves", Abstracts, 61st Annual Meeting, American Meteorological Society.

Goldstein, H., (1931); "On the Stability of Superposed Streams of Fluids of Different Denisities", Proc. Roy. Soc. A 132, 524-548.

Gossard, E. E., Richter, J. H., and Atlas, D., (1970); "Internal Waves in the Atmosphere from High-Resolution Radar Measurements", J. Geophysical Research 75, 3523-3536.

Gossard, E. E., Jensen, D. R., and Richter, J. H., (1971); "An Analytic Study of Tropospheric Structure as Seen by High-Resolution Radar", J. Atmos. Sci. 28, 794-807.

Gossard, E. E., Richter, J. H., and Jensen, D. R., (1973); "Effect of Wind Shear on Atmospheric Wave Instabilities Revealed by FM/CW Radar Observations", Boundary Layer Meteor. 4, 113-131.

Grimshaw, R., (1980); "Solitary Waves in a Compressible Fluid", University of Melbourne, Mathematics Research Report, No. 44.

Hammack, J. L., and H. Segur (1974); "The Korteweg-deVries Equation and Water Waves. Part 2. Comparison with Experiments", J. Fluid Mech. 65, 289-314.

Hammack, J. L., and H. Segur (1978); "The Korteweg-deVries Equation and Water Waves. Part 3. Oscillatory Waves", J. Fluid Mech. 84, 337-358.

Hardy, K. R., Ottersten, H., (1969); "Radar Investigations of Convective Patterns in the Clear Atmosphere", J. Atmos. Sci. 26, 666-672.

Holmboe, Forsythe, and Gustin (1943); Dynamic Meteorology, Wiley, New York.

Hooke, W. H., and Hardy, K. R., (1975); "Further Study of the Atmospheric Gravity Waves over the Eastern Seaboard on 18 March 1969", J. App. Meteor. 14, 31-38.

Hooke, W. H., Hall, F. F., and Gossard, E. E., (1973); "Observed Generation of an Atmospheric Gravity Wave by Shear Instability in the Mean Flow of the Planetary Boundary Layer", Boundary Layer Meteor. 5, 29-49.

Howard, L. N., (1961); "Note on a Paper by John W. Miles", J. Fluid Mech. $\underline{10}$, 509-512.

Jordan, A. R., (1972); "Atmospheric Gravity Waves from Winds and Storms", J. Atmos. Sci. $\underline{29}$, 445-456.

Kadomtsev, B. B., and Petviashvili, V. I., (1970); "On the Stability of Solitary Waves in Weakly Dispersing Media", Sov. Phys. Doklady $\underline{15}$, 539-541.

Klostermeyer, J., Ruster, R., (1980); "Radar Observation and Model Computation of a Jet Stream-Generated Kelvin-Helmholtz Instability", J. Geophys. Res. $\underline{85}$, 2841-2846.

Konrad, T. G., (1970); "The Dynamics of the Convective Process in Clear Air as Seen by Radar", J. Atmos. Sci. $\underline{27}$, 1138-1147.

Koop, C. G., and G. Butler (1981); "An Investigation of Internal Solitons in a Two Fluid System", J. Fluid Mech., to appear.

Lee, C.-Y., and Beardsley, R. C., (1974); "The Generation of Long Nonlinear Internal Waves in a Weakly Stratified Shear Flow", J. Geophys. Res. $\underline{79}$, 453-462.

Lenschow, D. H., and Stephens, P. L., (1980); "The Role of Thermals in the Convective Boundary Layer", Boundary Layer Meteor. $\underline{14}$, 509-531.

Lewellen, W. S., (1977); "Use of Invariant Modeling", in Handbook of Turbulence, (edited by Walter Frost and Trevor H. Moulden), Plenum Publishing Corporation, Vol. 1, pp. 237-280.

Lewellen, W. S., Teske, M. E., and Sheng, Y. P., (1980); "Micrometeorological Applications of a Second-Order Closure Model of Turbulent Transport", in Turbulent Shear Flows 2, Selected Papers from the Second International Symposium on Turbulent Shear Flows, Imperial College London, July 2-4, 1979, Springer-Verlag (New York).

Lewellen, W. S., and Sheng, Y. P., (1980); "Modeling Tornado Dynamics", Nuclear Regulatory Commission, NTIS No. NUREG/CR-1585, 227 pp.

Lewellen, W. S., and Teske, M. E., (1973); "Prediction of the Monin-Obukhov Similarity Functions from an Invariant Model of Turbulence", J. Atmos. Sci. $\underline{30}$, 1340-1345.

Lewellen, W. S., Teske, M. E., and Donaldson, C. duP., (1976); "Variable Density Flows Computed by a Second-Order Closure Description of Turbulence", AIAA J. $\underline{14}$, 382-387.

Lilly, D. K., and Toutenhoofd, W., (1969); "The Colorado Lee Wave Program", Reprinted from Clear Air Turbulence and Its Detection, Plenum Press, pp. 232-245.

Lilly, D. K., (1971); "Observations of Mountain-Induced Turbulence", Journal of Geophysical Research 76, 6585-6588.

Maxworthy, T, and Browand, F. K., (1975); "Experiments in Rotating and Stratified Flows with Oceanographic Application", Ann. Rev. Fluid Mech. 7, 273-305.

Metcalf, J. I., (1975); "Gravity Waves in a Low-Level Inversion", J. Atmos. Sci. 32, 351-361.

Miles, J. W., (1961); "On the Stability of Heterogeneous Shear Flows", J. Fluid Mech. 10, 496-508.

Morton, B. R., Taylor, G. I., and Turner, J. S., (1956); "Turbulent Gravitational Convection from Maintained and Instantaneous Sources", Proc. Roy. Soc. A 234, 1-23.

Mowbray, D. E. and Rarity, B. S. H., (1967); "A Theoretical and Experimental Investigation of the Phase Configuration of Internal Waves of Small Amplitude in a Density Stratified Liquid", J. Fluid Mech. 28, 1-16.

Noonkester, V. R., (1973); "Breaking Wave Characteristics Determined from FM-CW Radar Observations", Bull. AMS 54, 937-941.

Oliver, V. J., (1981); "Atmospheric Gravity Waves of the Eastern Pacific", Abstracts, 61st Annual Meeting, American Meteorological Society.

Orlanski, I., and Ross, B. B., (1973); "Numerical Simulation of the Generation and Breaking of Internal Gravity Waves", J. Geophys. Res. 78, 8808-8826.

Osborne, A. R., and T. L. Burch (1980); Science 208, 451.

Ottersten, H., Hardy, K. R., and Little, C. G., (1973); "Radar and Sodar Probing of Waves and Turbulence in Statically Stable Clear Air Layers", Boundary Layer Meteor. 4, 47-89.

Patnaik, P. C., Sherman, F. S., and Corcos, G. M., (1976); "A Numerical Simulation of Kelvin-Helmholtz Waves of Finite Amplitude", J. Fluid Mech. 73, 215-140.

Reed, R. J., and Hardy, K. R., (1972); "A Case Study of Persistent, Intense, Clear Air Turbulence in an Upper Level Frontal Zone", J. App. Meteor. 11, 514-549.

Richter, J. H., Jensen, D. R., and Noonkester, V. R., (1974); "Clear Air Convection: A Close Look at Its Evolution and Structure", Geophys. Res. Lett. 1, 173-176.

Richter, J. H., (1980); "Remote Sensing of Atmospheric Water Vapor Fluctuations", Atmospheric Water Vapor, Deepak, et al. (ed.), Academic Press.

Ruhnke, L. H., (1979); "Data Catalog of Aircraft Measurements May 13 to May 17, 1979", Naval Research Laboratory (Washington, D.C. 20375)

Satsuma, J., (1976); "N-Soliton Solution of the Two-Dimensional Korteweg-deVries Equation", J. Phys. Soc. Japan 40, 286-290.

Sethuraman, S., (1977); "The Observed Generation and Breaking of Atmospheric Internal Gravity Waves over the Ocean", Boundary Layer Meteorology 12, 331-349.

Sethuraman, S., (1980); "A Case of Persistent Breaking of Internal Gravity Waves in the Atmospheric Surface Layer over the Ocean", Boundary Layer Meteorology 19, 67-80.

Scorer, R. S., (1957); "Experiments on Convection of Isolated Masses of Buoyant Fluid", J. Fluid Mech. 2, 583-594.

Segur, H., and Hammack, J. L., (1981); "Long Internal Waves of Moderate Amplitude. I. Solitons", preprint.

Stilke, G., (1973); "Occurrence and Features of Ducted Modes of Internal Gravity Waves Over Western Europe and Their Influence on Microwave Propagation", Boundary Layer Meteor. 4, 493-509.

Swartztrauber, P.N. and Sweet,R.A. (1979); "Efficient FORTRAN Subprograms for the Solution of Separable Elliptic Partial Differential Equations", Assoc. for Comp. Mach., Trans. on Math. Software, 5, 352-364.

Taylor, G. I., (1931); "Effect of Variation in Density on the Stability of Superposed Streams of Fluid", Proc. Roy. Soc. A 132, 499-523.

Thorpe, S. A., (1973); "Experiments on Instability and Turbulence in a Stratified Sear Flow", J. Fluid Mech. 61, 731-751.

Uccelini, L. W., (1975); "A Case Study of Apparent Gravity Wave Initiation of Severe Convective Storms", Monthly Weather Review 103, 497-513.

Van Dorn, W. G., (1964); Proceedings of the 9th Conference on Coastal Engineering, Lisbon, Portugal, pp. 166-190.

Woodward, B., (1956); "Exploration by Sailplanes of the Structure of Thermals", O.S.T.I.V. News, Supplement to Swiss Aero. Revue, September.

Wurtele, M. G., (1955); "The Transient Development of a Lee Wave", J. Mar. Res. 14, 1-13.

Wyngaard, J. C., and Coté, O. R., (1974); "The Evolution of the Convective Planetary Boundary Layer - A Higher Order Closure Model Study", Boundary Layer Meteorology 7, 289-308.

Yamada, T., and Mellor, G. L., (1975); "A Simulation of the Wangara Atmospheric Boundary Layer Data", J. Atmos. Sci. 32, 2309-2329.

Zakharov and Shabat (1974); "A Scheme for Integrating the Nonlinear Equations...", Funct. Anal. and Appl. 8, 226-235.

VanZandt, T. E., Green, W. L., Clark, W. L., and Grant, J. R., (1979); "Buoyancy Waves in the Troposphere: Doppler Radar Observations and a Theoretical Model", Geophys. Res. Lett. 6, 429-433.

Zeman, O., and Lumley, J. L., (1976); "Modeling Buoyancy Driven Mixed Layers", J. Atmos. Sci. 33, 1974-1988.

DATE FILMED

8